ABSTRACT

CUNNINGHAM, JEFFREY GLENN. Atmospheric Characteristics of Cool Season Intermittent Precipitation Near Portland, Oregon. (Under the direction of Dr. Sandra E. Yuter.)

Pacific Northwest cool season precipitation is often described as mostly stratiform (i.e. steady and continuous). While most regional precipitation is stratiform in terms of area and duration, embedded convective cells within stratiform precipitation occur frequently enough to warrant study. Embedded cells locally increase rain rate, total precipitation, and streamflow discharge and hence raise the risk of flooding, landslides, and debris flows. Analysis of vertically pointing radar data near Portland, Oregon for three cool seasons (2005 to 2008) indicates that fallstreaks in the snow layer, locally enhanced precipitation regions a few kilometers in size indicated in radar reflectivity data above the 0° C altitude, are nearly ubiquitous on days with significant rainfall accumulation and large areas of precipitation. The observed fallstreaks in snow enhance rainfall immediately below the snow fallstreak. Compared to stratiform periods, embedded convective periods include higher Doppler vertical velocity values and higher variability in velocities especially in the snow layer. The combination of these findings points to generating cells within the snow layer and the seeder-feeder mechanism as important sources of surface precipitation variability for periods of embedded convective cells within stratiform precipitation. The primary goal of this study was to determine the sources of instability typically associated with convective cells embedded within stratiform precipitation for Pacific Northwest cool season storms. Storm periods occurring over six cool seasons (2002 to 2008, totaling 1923 hours) of operational radar data (KRTX) and 166 upper air soundings (KSLE) are analyzed. A new method was employed to objectively determine the degree of precipitation intermittency in sequences of radar scans. The resulting continuum of intermittency values was grouped into four categories: mostly convective precipitation, mostly stratiform precipitation, embedded convective cells within stratiform precipitation, and other.

Atmospheric soundings during periods with embedded convective cells within stratiform precipitation are more likely to have convective available potential energy (CAPE) than soundings during periods of mostly stratiform precipitation. Specifically, most unstable

parcel CAPE (MUCAPE) > 0 J kg^{-1} occurs 2.8 more frequently during embedded periods than for mostly stratiform periods. Over 90% of embedded periods have MUCAPE > 0 J kg^{-1} or at least two 500 meter layers of potential instability. In contrast to the near surface based instability most commonly associated with the mostly convective precipitation, embedded convection is elevated. The median most unstable parcel height of origin for embedded convective periods is 2.5 km compared to 0.5 km for mostly convective periods.

Although this present research did not deal directly with orographic precipitation enhancement, it does address synoptic and mesoscale precipitation processes that frequently occur near terrain in the Pacific Northwest. The exclusion of the seeder-feeder mechanism as a mode of cellularity for orographic precipitation in recent work is inconsistent with the observations presented here and inconsistent with much of the pre-2000 literature, which show the seeder-feeder mechanism directly modulating surface rain rate with or without terrain present. Numerical models, whether operational or idealized, need to represent the seeder-feeder process in order to accurately simulate precipitation variability at small spatial scales (less than < 5-10 km) and temporal scales (< 3 hours) within the warm sector of Pacific Northwest extratropical cyclones.

Atmospheric Characteristics of Cool Season Intermittent Precipitation Near Portland, Oregon

by
Jeffrey Glenn Cunningham

A dissertation submitted to the Graduate Faculty of
North Carolina State University
in partial fulfillment of the
requirements for the degree of
Doctor of Philosophy

Marine, Earth, and Atmospheric Sciences

Raleigh, North Carolina
2012

APPROVED BY:

Sandra E. Yuter Committee Chair	Matthew D. Parker
Karl W. Wegmann	Sankarasubramanian Arumugam

DEDICATION

To my family, for their sacrifices, while preparing this research.

ACKNOWLEDGMENTS

Everything is a team effort! This work was made possible with the generous support of the United States Air Force and the Air Force Institute of Technology's Civilian Institution Programs, but the views expressed in this document are those of the author and do not reflect the official policy or position of the United States Air Force, Department of Defense, or the U.S. Government. Dr. Sandra Yuter, my advisor and committee chair, was nearly always available for guidance and mentoring. For this, I am very thankful. I also wish to thank Drs. Matt Parker, Karl Wegmann, Sankar Arumugam, and David Kingsmill for taking their time to serve on my PhD committee or during the exam (Kingsmill) and for providing expert advice during the development of this research. Beth Tully provided figure illustration support.

I will always be grateful for the culture of teamwork and cooperation in the North Carolina State University's Cloud Precipitation Processes and Patterns Group. Dr. Matthew Miller provided editorial guidance on this dissertation and countless hours of Matlab support over the last three years. Andrew "MacGyver" Hall, Matlab programmer extraordinaire and friend, provided code discussion and feedback on many occasions. John L'Heureux and Matthew Woelfle spent endless hours ensuring that over 2 million files and over 7 TB of radar data were processed correctly. Tai Bryant provided MRR and surface data support. Casey Burleyson and Nate Hardin, my friends, officemates, and "sharpening stones" provided edifying feedback regarding my research, gardening, and life in-general. I appreciate Dr. Parker's Convective Storms research group for their insight into convective processes, for providing the CAPE code used to calculate several vertical profile variables, and for great Friday lunch conversations. Regular thoughtful discussions with Dr. Brian Colle and members of his SUNY research group (Sara Ganetis and David Stark) added depth and breadth to my understanding of Pacific Northwest precipitation processes.

I also wish to acknowledge my church congregation and friends who supported my family and me during times of illness, God for His many blessings in my life, and my wife and kids who sacrificed more than anyone else during the countless hours I spent researching and preparing this dissertation.

TABLE OF CONTENTS

LIST OF TABLES

LIST OF FIGURES

Chapter 1 - Introduction and Background

1.1 Introduction

1.1.1 Motivation

Between 1955 and 2011, 50 out of 71 federal major disaster declarations for Washington and Oregon were directly related to flooding, landslides, or debris flows (FEMA, 2012). These natural disasters occurred as a result of large rainfall accumulations during the cool season. Several synoptic and mesoscale conceptual models have been developed to help explain cool season precipitation in the Pacific Northwest since the 1960s. Most of the conceptual models illustrate important aspects of extratropical cyclone precipitation, such as frontal features (traditional and split-cold front), the warm conveyor belt, the atmospheric river, and frontal rainbands of various types (Harrold, 1973; Hobbs, 1978; Bao et al., 2006, Browning, 1990). Additional studies have focused on the role of terrain on precipitation location and intensity (Roe, 2005; Rotunno and Houze, 2007; Yuter et al., 2011). Although regional cool season precipitation is predominantly stratiform (i.e. steady and continuous), embedded convective within stratiform (i.e. variable precipitation intensity) occurs frequently enough to increase total precipitation and streamflow discharge (Hobbs, 1980; Houze, 1997; Westrick and Mass, 2001). What are the primary factors responsible for cool season embedded convective within stratiform precipitation in the Pacific Northwest?

To address this question, this dissertation is organized in the following manner. Chapter 1 highlights important literature concerning this research topic. Chapter 2 describes the research objective and hypothesis. Chapter 3 describes the data and methodology used in this research. Chapter 4 presents case study examples from the results. Chapter 5 presents the results from the six years of observations. Finally, Chapter 6 synthesizes the results with existing literature and lists recommendations for future work.

The following terms are used frequently throughout this document: 1) mostly stratiform precipitation, 2) embedded convective within stratiform precipitation, and 3) mostly convective precipitation. The terms are categorical descriptions of precipitation with varying degrees of precipitation intermittency (used in this document as an adjective to describe stopping and starting, and variable intensity). The terms are least intermittent to most intermittent, respectively. Intermittent precipitation (the noun) refers to embedded convective within stratiform precipitation and/or mostly convective precipitation. Detailed definitions are presented in Chapter 3.

1.1.2 Overview

In the literature, convective precipitation structure is often referred to as intermittent, turbulent, banded, or cellular and can occur at scales from a few to hundreds of kilometers (Rotunno and Houze, 2007). All of these adjectives describe various characteristics of convective precipitation, but intermittent stands out as a common quality easily identifiable on radar. Intermittent precipitation starts, stops, and changes intensity more frequently than non-intermittent precipitation. A comparison of six years (2002 to 2008) of operational radar-derived precipitation intermittency measures and sounding variables (moisture, hydrostatic instability, etc.) shows that embedded convective within stratiform precipitation is related to increased frequency of sounding profiles with most unstable parcel buoyancy compared to only stratiform precipitation. Most of the embedded convection is aloft (> 2.5 km), rather than low-level (0.5 km) as during mostly convective periods. Analysis of vertically pointing radar data near Portland, Oregon for three cool seasons (2005 to 2008) indicates that fallstreaks in snow, locally enhanced precipitation regions a few kilometers in size indicated in radar reflectivity data above the 0° C altitude, are nearly ubiquitous on days with significant rainfall accumulation and large areas of precipitation. The observed fallstreaks in snow enhance rainfall immediately below the snow fallstreak via the seeder-feeder process, (Marshall, 1953; Gunn et al., 1954; Browning et al., 1974; Rutledge and Hobbs, 1983) which in-turn increases precipitation intermittency (i.e. the convective nature of the precipitation).

Recent research studies associated with understanding orographic precipitation enhancement (Rotunno and Houze, 2007; Kirshbaum and Smith, 2008; Cannon et al., 2011) discuss the seeder-feeder mechanism as a possibly important mechanism in their respective background literature sections, but often develop idealized modeling scenarios without accounting for generating cells aloft. Most the recent research focuses on surface based hydrostatic instability or vertical wind shear instability (Kelvin-Helmholtz instability) as primary mechanisms for precipitation enhancement. This study finds that surface based buoyancy is most common at the surface cold front and within the cold sector of extratropical cyclones. In the warm conveyor belt region the elevated buoyancy associated with the seeder-feeder mechanism is the primary process for creating intermittent precipitation near the surface.

1.2 Background Literature Review

The primary factors responsible for cool season intermittent precipitation are meteorological processes at various spatial and time scales. The following subsections review the literature by moving from the large scale to the mesoscale. The first subsection describes the local geography and climatology, the second subsection describes synoptic and large scale influences, the third subsection is on mesoscale precipitation near cyclones, and finally the last subsection reviews the relationship between terrain and precipitation, as well as addressing the outstanding questions considered in this study.

1.2.1 Pacific Northwest Geography and Climatology

The Pacific Northwest is a vast region which encompasses many geographic zones and includes very complex mountainous terrain (Fig 1.1). To the west, the Pacific Ocean provides a source of moisture and mild near-surface atmospheric temperatures. The Willamette Valley, home to Portland, Oregon, is nestled between the Coast Range (up to approximately 1 km elevation) and the Cascade Range (2 to 3 km elevation). Portland, Oregon is the central location of the study area. To the east of Oregon and Washington, the Northern Rocky Mountain Range climbs vertically to an altitude of over 3 km and serves to slow or block cold North American continental air masses from affecting most of the Pacific Northwest.

Temperatures in the Pacific Northwest depend heavily on local geography, such as proximity to the Pacific Ocean and to mountains (Mass, 2008). In the cool season (November to March), the coast averages minimum and maximum temperatures from 0° C to 15 ° C, respectively. The minimum and maximum temperatures in the Willamette Valley are cooler by a few degrees on average. The mountains experience much cooler temperatures, dropping well below 0° C at night and remaining just above 0° C during the day. Annual precipitation in the Pacific Northwest varies widely from a 1 to 2 centimeters in inland deserts to 2-3 meters on mountain peaks (Fig 1.2). The Willamette Valley receives annually about 85-100 cm of precipitation. Most regional precipitation falls during the cool season as a result of strong southwesterly moisture flux driven by winter cyclones passing through the region. Wind direction and the height of the 0° C level are the primary controls on precipitation intensity and location (Yuter et al., 2011). Yuter et al. found the median winter storm 0° C level was about 1.5 km. Easterly gap flow from the Columbia River Gorge occurs frequently during the cool season, when the pressure gradient increases with approaching low pressure systems (Sharp and Mass, 2004). The gap flow is responsible for bringing colder temperatures to the Willamette Valley and is often accompanied with freezing rain and snow.

1.2.2 Synoptic-Scale Influences and Atmospheric Rivers

The Pacific Northwest region centered near 45° N, experiences strong midlatitude synoptic-scale storm systems throughout the cool season. Many, if not most, extratropical cyclones approaching the Pacific Northwest have the basic features described by the Norwegian cyclone model developed in the early 20th century (Fig 1.3), such as a surface warm and a surface cold front. Air mass fronts have a cross-frontal horizontal scale of 100 km or less, but can have along front lengths of a few thousand kilometers (Markowski and Richardson, 2010). The along front direction is considered synoptic scale, while the cross-front direction is on the mesoscale. The warm front typically extends to the east-southeast from a low pressure center. Behind (or south) of the warm front is the warm sector where most of the precipitation occurs. The cold front normally extends southward from the low pressure center. Behind or west of the cold front is the cold sector which consists of generally cooler, drier air. Extratropical cyclones are the primary synoptic scale features that bring moisture to the Pacific Northwest.

Wernli and Schwierz's (2006) analysis of global sea level pressure fields from the European Center for Medium-Range Weather Forecasts (ECMWF) Re-Analysis (ERA-40) for years 1958-2001 revealed a maximal seasonal mean (December, January, and February) cyclone frequency of 35% in the Northern Pacific (Fig. 1.4). Most of the cyclones that impact the United States West Coast (30° to 55° N) originate in the northeastern Pacific. Cyclone frequency is highest during cool season months November to March.

Atmospheric rivers (ARs) and the associated strong low-level moisture flux are probably the most significant large scale features of extratropical cyclones for cool season Pacific Northwest precipitation (Zhu and Newell, 1998; Lin et al. 2012). The AR is defined as a long narrow filament of a minimum with 2 cm of integrated water vapor and is typically defined using the data from the Special Sensor Microwave Imager (SSM/I) (Bao et al., 2006). Ralph et al. (2011) hypothesize that ARs producing flooding along the U.S. west coast often occur as a result of a superposition of tropical mechanisms (such as the Madden Julian Oscillation and Kelvin Waves) and extratropical wave packets in the mid-latitude westerlies. Regardless, the necessary planetary and synoptic scale circulations yield local convergence of moisture and transport moisture poleward within a narrow filament (≈400 km wide and >2000 km long) in the low-level jet ahead of cold fronts (Bao et al. 2006, Neiman et al., 2008; Ralph et al. 2011). Vertically, the AR is characterized by a peak moisture flux occurring at approximately 850 mb and tapering-off at about 500 mb (Ralph et al., 2011). The location of the high moisture flux is caused by a combination of the pre-frontal low-level jet (LLJ) and high values of low-level moisture (Ralph et al., 2005) (Fig. 1.5).   ARs have been directly linked to extreme flooding events near the West Coast of the United States. Specifically, Ralph et al. (2006) linked ARs to 7 severe flooding events in northern California's Russian river basin from October 1997 to February 2006. Similar observations have been made for other regions along the West Coast. For the water years[1] 1998-2005, 301 ARs transected the North American coast from Oregon to British Columbia (Neiman et al., 2008).

Ralph et al. (2005) produced average soundings of ARs approaching the West Coast from 10 storms during CALJET-1998 and PACJET 2001 (Fig. 1.6). These average profiles showed a nearly saturated atmosphere below ≈800 mb, southwest flow, and veering winds with height (indicating warm air advection). A strong LLJ of 23.4 ± 9.4 m s^{-1} was prominent at 1 km. The static stability of the ARs was characterized as neutral with respect to the moist Brunt Väisälä Frequency, N_m^2 as derived by Durran and Klemp (1982). Since the vertical profile is an average of several cases, it does not characterize spatial or temporal variability and may conceal important mesoscale instabilities and frontal forcing mechanisms that are often intertwined in the precipitating regions associated with frontal passage.

1.2.3 Observations of Mesoscale Precipitation Processes near Extratropical Cyclones

Previous studies on mesoscale precipitation near extratropical cyclones suggest that a mixture of hydrostatic and hydrodynamic instabilities affect the structure of mesoscale precipitation areas. Unfortunately, many of the previous studies do not systematically quantify or relate with long-term (i.e. multi-year) datasets precipitation intermittency to mesoscale instabilities. Instead, these studies rely on many detailed case studies to describe the relationship of mesoscale instabilities to precipitation structure. Some studies that do include many cases tend to average the data, leading to masking of important mesoscale features responsible for precipitation structure.

The classical Norwegian cyclone model does not address mesoscale precipitation within a cyclone. Since the 1960's, several field projects and studies have been conducted to examine mesoscale precipitation structure along the U.S. West Coast and near the United Kingdom (e.g. Nagle and Serebreny, 1962; Browning et al., 1974, Hobbs, 1975; Houze et al., 1976; Matejka et al., 1980, Yu and Smull, 2000; Medina et al., 2007, Colle et al. 2008).

[1] A water year begins October 1st through and September 30th the following year.

Over time, several conceptual models were developed to explain mesoscale precipitation structure associated extratropical cyclones passing over the West Coast.

Nagle and Serebreny (1962) developed one of the first conceptual models to describe mesoscale precipitation structures associated with maritime extratropical cyclones approaching the West Coast. Their conceptual model labels precipitation types based on the order in which they typically arrive at a given location. This conceptual model was further adapted by Medina et al. (2007) (Fig 1.7). The basic model describes the eastern most (early) precipitation as stratiform and continuous and steady in nature. Precipitation becomes convective and more intense in the middle and late sectors. Embedded convective within stratiform precipitation elements exist in the middle sector. Within the late sector, individual isolated convective cells are the dominant structure type.

Using aircraft and surface observations, Hobbs (1975) identified three sequential sets of conditions associated with cyclone passage over the Pacific Northwest. *Pre-frontal conditions* occurred first and included layered clouds from the surface to 9 km altitude, a variety of ice crystals (plates, sectors, and dendrites), low relative concentrations of ice particles and water droplets, liquid water contents of 0 to 0.5 gm^{-3}, light turbulence, very little riming, and a steady precipitation rate of 1.3 to 2.6 mm h^{-1}. *Transitional conditions* followed and had layered clouds up to 5.4 km altitude with embedded cumulus, similar crystal types as *pre-frontal* conditions, but with higher relative concentrations of ice particles and water droplets. Some regions with transitional conditions also had moderate to severe turbulence, riming, graupel, and heavy showers with rain rates up to 7.6 mm h^{-1}. Finally, *post-frontal conditions* had convective tops up to 4.6 km altitude, lower concentration of ice crystals, and higher concentrations of water droplets than pre-frontal. Post-frontal conditions also included moderate to severe turbulence, heavy riming, graupel and showers with a rain rate up to 5.2 mm h^{-1}. Qualitatively, Hobbs' (1975) aircraft observations are consistent with Nagle and Serebreny's (1962) horizontal conceptual model.

Hobbs (1978) further categorized mesoscale precipitation areas within the traditional cyclone model by synthesizing University of Washington's CYCLonic Extratropical Storms

(CYCLES) Project data[2] with observations from other studies from around the world. They classified 6 basic types of mesoscale rainbands according to their location relative to the cyclone (Fig 1.8). Type 1, *warm-frontal bands*, are approximately 50 km wide, located at the surface warm-front or ahead of the surface warm front and were oriented parallel to the surface warm front. Type 2, *warm-sector bands*, are approximately 50 km wide in the warm sector of the cyclone and are oriented parallel to the surface cold front. Type 3a, *wide-cold-frontal*, are approximately 50 km, located overtop the surface cold front or if there is an occlusion near the cold front aloft. Type 3b, *narrow cold-frontal bands*, are approximately 5 km wide and are just behind or along the surface cold front. Types 4, prefrontal cold-surge bands, are approximately 50 km wide and are often associated with a cold front aloft. Type 5, *postfrontal bands*, form behind and parallel to the cold front.

Parsons and Hobbs (1983) described likely causal mechanisms for several convective precipitation structures identified by Hobbs (1978). For the warm sector rain bands, they hypothesized potential instability and conditional symmetric instability as the primary causal factors, but dismissed internal gravity waves and vertical shear as likely candidates. Rutledge and Hobbs (1983) developed a parameterized numerical model to explain the seeder-feeder process in warm-frontal rainbands. The seeder-feeder conceptual model (Houze, 1993; Fig 1.9) shows a potentially unstable layer aloft with generating cells seeding ice crystals into a more stable moist layer near the surface (the feeder cloud). When the horizontally moving moist air layer near the surface encounters a hill or a mountain, it may lift vertically enough to produce cloud, but not precipitation. The seeder cloud from above provides the necessary crystals to trigger precipitation formation, where otherwise the seeder crystals might have evaporated if the orographic cap cloud was not present.

For the narrow-cold frontal rainbands, Parson and Hobbs (1983) attributed convection to a strong horizontal wind shift and possibly gravity current effects. Jorgensen et al. (2003) studied a narrow cold frontal rainband with echo tops near 4-5 km off the coast of California. Pseudo-dual-Doppler analyses showed low-level convergence ahead of the narrow cold frontal rainband. Jorgensen et al. suggest that a density current accounts for

[2] CYCLES occurred from 1973-1986.

some of the explained motion of surface cold fronts and the observed narrow cold-frontal rainband. Parson and Hobbs ascribed other possible theories for *wide cold frontal rainbands, post frontal rainbands and isolated convective cells,* such as internal gravity waves, boundary layer mechanisms and potential instability, respectively. They considered wide cold-frontal rainbands and warm frontal rainbands as enhancements of stratiform precipitation. Although the last two rainbands were described as stratiform, the primary process for generating precipitation was hypothesized as a seeder-feeder process (Herzegh and Hobbs, 1980).

The split-front model was proposed by Browning and Monk (1982) to explain commonly observed precipitation patterns in the warm conveyor belt region of extratropical cyclones near the United Kingdom (Fig. 1.10). This conceptual model features an elevated layer of potential instability, which results in mostly stratiform precipitation ahead of the surface cold front (shallow moist zone). The upper front is best characterized by a gradient in equivalent potential temperature[3] rather than potential temperature, since equivalent potential temperature also includes the effect of moisture. The split-front model stands in contrast to the "traditional" cold front conceptual model (Fig. 1.11), because the traditional model shows the slope of the cold front tilted backwards towards the cold sector (Bader et al., 1995), whereas in the split front the tilt is towards the warm sector. Figure 1.12 is an infrared satellite image showing the difference between a traditional cold front (Fig. 1.12a) and a split-front (Fig. 1.12b). The split front case shows an area of low clouds between the surface cold front and the cold front aloft. Woods et al. (2005) observed potential instability associated with a forward bent cold front for the 13 December 2001 storm from the Improvement of Microphysical Parameterization through Observational Verification Experiment (IMPROVE- 2) field project (Fig. 1.13). Evans et al. (2005) observed many generating cells in two elevated layers aloft associated with a forward titled cold front associated with the 1-2 February 2001 IMPROVE-1 storm. A cross-section of a cold frontal zone and associated atmospheric river presented by Ralph et al. (2011) for a storm event from 25 March 2005 also shows a region of elevated potential instability (Fig 1.14). With cross-sections through pre-cold frontal regions, these previous studies indicated the presence

[3] See Appendix C for a definition of equivalent potential temperature.

of potential instability (a latent hydrostatic instability), despite the characterization of this region by other studies as being mostly moist neutral (Ralph et al., 2005). This present work will address to a limited extent, the possible role of potential instability in generating intermittent precipitation.

1.2.4 Precipitation near Terrain

As extratropical cyclones pass over the complex terrain of the Pacific Northwest, they also produce orographic precipitation. In general, when an AR or strong moisture flux within a cyclone transects a mountain range, orographic precipitation enhancement occurs on the windward side of the mountain or ridge. Environmental factors such as the height of the 0° C level, static stability, whether or not flow blocking is occurring, wind direction, cross-barrier wind speed, localized convergence, and barrier jet formation also contribute to determining precipitation intensity and location (Colle, 2004; Reeves et al., 2008; Hughes et al., 2009; Lundquist et al., 2010; Nieman et al., 2010; Panzierra and Germann, 2010; Yuter et al., 2011;). Yuter et al. (2011) found that the height of the 0° C level and cross-barrier wind speed are more important than stability in controlling the spatial distribution of orographic precipitation in the Portland, Oregon region.

Browning et al. (1974) used the term mesoscale precipitation areas (MPAs) for regions with diameters of 10 to 100 km of relatively heavy rain, in the warm sector of a wintertime mid-latitude cyclone passing over the British Isles. These MPAs appeared to be associated with elevated layers of potential instability, which produced convective seeder cells aloft (Fig 1.15). The MPAs did not tend to organize into bands and were mostly initiated over open-ocean before landfall. When the MPAs passed over the mountains some dissipated on the downwind side, while others tracked across the entire radar network. Some MPAs appeared to be initiated by the terrain. Using surface rain gauges and scanning radar, Browning et al. (1974) observed cellular orographic precipitation enhancement as the cells aloft transected the orography (in addition to the background precipitation produced from flow ascent).

Work in the Pacific Northwest and the European Alps also suggests that cellularity is an important mechanism for orographic precipitation enhancement (Rotunno and Houze, 2007). The thought is that increased turbulent motion within cellular clouds leads to more efficient conversion of condensate to precipitation. In summarizing results from the Mesoscale Alpine Programme (MAP) and their own work, Rotunno and Houze suggest two modes of cellularity for orographic precipitation enhancement. First mode conditions are unblocked and unstable and the second mode is blocked and stable (Fig 1.16). In the former mode, precipitation enhancement occurs most intensely over the windward slope and terrain peaks and in the latter mode enhancement occurs along a shear layer located over a blocked air layer. Houze and Medina (2005) suggest that during blocked scenarios a layer of vertical wind shear instability (Kelvin-Helmholtz instability) causes the turbulent cellular motions (> 2 m s^{-1}) and thus enhances the precipitation.

Using idealized modeling, Kirshbaum and Durran (2004) found that terrain-locked banded cellular precipitation caused by orographic lifting over small-scale terrain features could have a large impact on local accumulated precipitation totals. They also found that while potential instability is a good predictor for cellular convection, the moist Brunt Väisälä frequency, as defined by Durran and Klemp (1982) and Emanuel (1994), is a more accurate predictor for cellularity, because of the inclusion of the gradient of total water mixing ratio in the equation for N_m^2. Cellularity increased with residence time of a parcel in a cap cloud and with increased mountain width, but decreased with an increase in environmental wind shear in 2D simulations. In another idealized modeling study using only liquid microphysics (Kessler, 1969), Fuhrer and Schar (2005) argued that a “marginally unstable” (potentially unstable) air mass transecting a mountain ridge leads to development of stratiform precipitation with embedded convection. They describe the development of embedded convection within a stratiform region as highly dependent on small amplitude upstream perturbations, which enhance the efficiency of the convective circulations. In model sensitivity experiments of mixed phase clouds Colle et al. (2008) found that the Coast Range is important for triggering convective cells and associated local precipitation enhancement, but decreased precipitation in the Cascade Range. Using mixed phase microphysics in a modeling sensitivity study, Kirshbaum and Smith (2008) and Cannon et al. (2011) found that not all convection brings about more efficient conversion of condensation to precipitation. They cite reasons such as the competing effects of downdrafts and updrafts, a decrease in condensation rates with higher air flow temperatures, and redistribution of moisture through convection. One weakness of the above idealized orographic precipitation modeling studies appears to be the exclusion of seeder-feeder related processes (both the elevated hydrostatic instability and microphysical response). For instance, the profiles used in Fuhrer and Schar, (2005), Kirshbaum and Smith (2008) and Cannon et al. (2011) use vertical profiles with only near-surface potential instability (decreasing equivalent potential temperature with increasing height) (Fig. 1.17). Previous observational work has shown that elevated convective cells (associated with elevated potential instability aloft) associated with/without feeder clouds and with/without terrain are important for precipitation near extratropical cyclones (Browning et al., 1974; Cotton et al., 2011). Cannon et al. (2011) recognized this limitation by stating, "…some clouds that were unable to internally generate much precipitation in our simulations may become much more efficient when seeded from above."

As shown with the previous studies discussed here, a mixture of hydrostatic and hydrodynamic instabilities can affect the structure of mesoscale precipitation areas near Portland, Oregon. Cool season precipitation near Portland is influenced by both extratropical cyclone processes and terrain. Unfortunately, many of the previous studies do not systematically quantify or relate, with multi-year datasets, precipitation intermittency to the location and magnitude of mesoscale instabilities (hydrostatic or hydrodynamic). Field experiment case studies advantageously provide a variety of important details about mesoscale precipitation areas, but often lack statistical context regarding how frequently the different types of event may occur. Past studies with larger datasets have tended to average results, potentially masking important hydrostatic instabilities (Ralph et al., 2005). The current conceptual models for precipitation near terrain do not explicitly address how common each mode occurs and do not include elevated convective cells or the seeder-feeder mechanism (Rotunno and Houze, 2007). Idealized modeling studies of precipitation near terrain have tested the sensitivity of embedded convection precipitation processes without fully accounting for elevated convective cells or the seeder feeder process (Kirshbaum and Durran, 2004; Fuhrer and Schar, 2005; Kirshbaum and Smith, 2008; and Cannon et al., 2011). This present study is designed to elucidate the impact of hydrostatic instability on cool season intermittent precipitation (specifically, embedded convective within stratiform precipitation) near Portland Oregon.

1.3 Chapter Figures

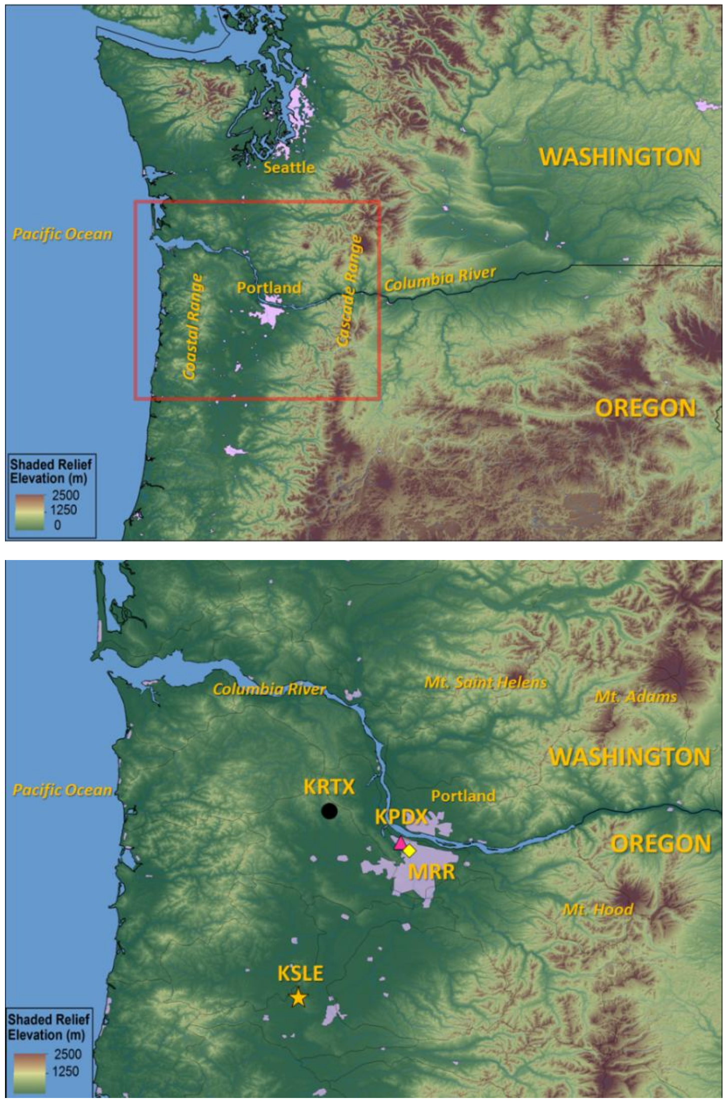

FIG. 1.1. Terrain maps of the study domain and location of instruments. a) large view of the study region shows the major political and geographic features. b) zoomed-in view of the Portland, Oregon region with locations of important instruments indicated by various shapes. The black circle is the NWS WSR-88D operational scanning radar, the pink triangle is the Portland International Airport METAR, the yellow diamond is the MRR vertically pointing radar, and the yellow star is the operational Salem, Oregon sounding. Maps are provided courtesy of Nate Hardin.

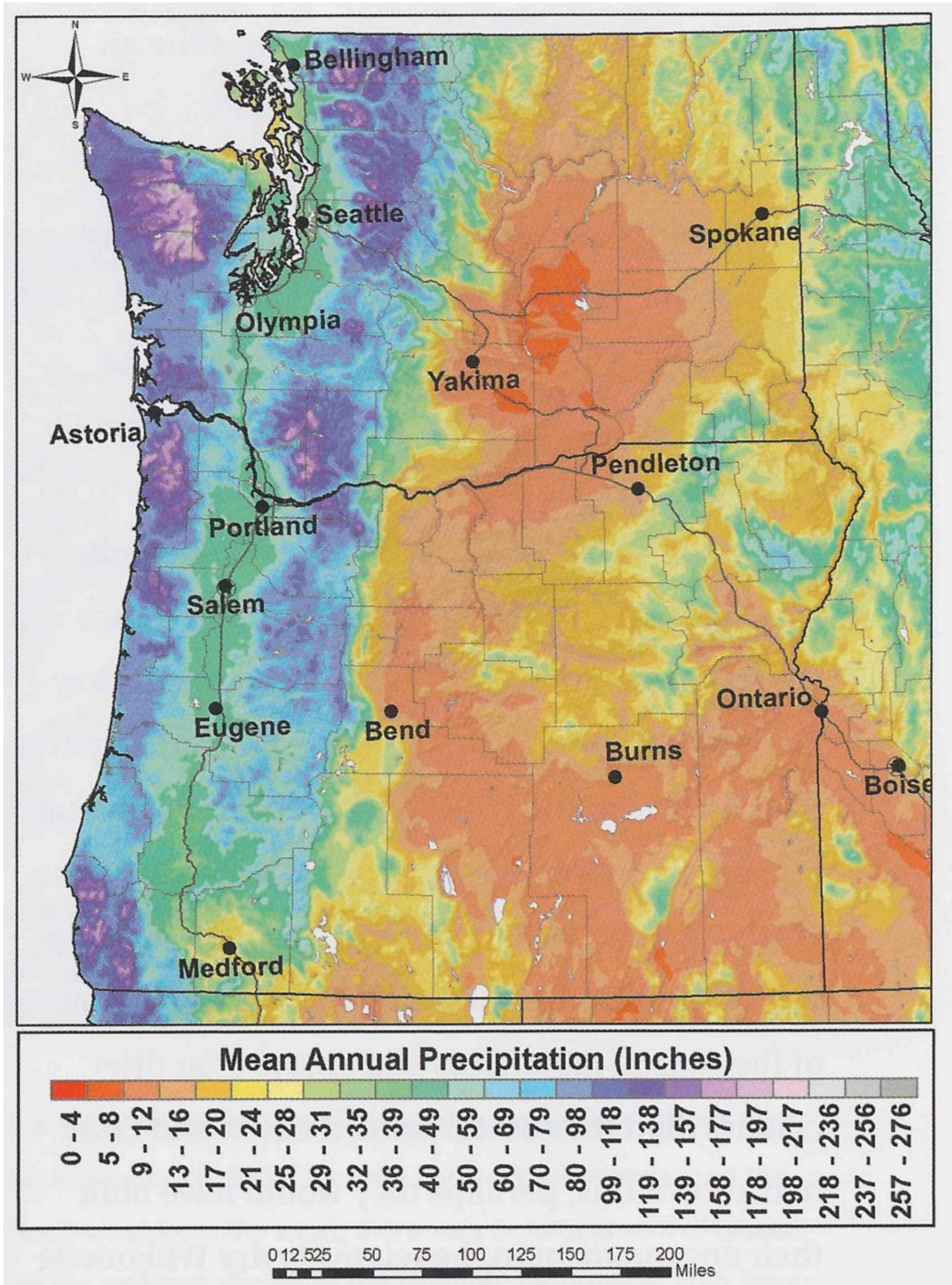

FIG. 1.2. Pacific Northwest mean annual precipitation (Mass, 2008).

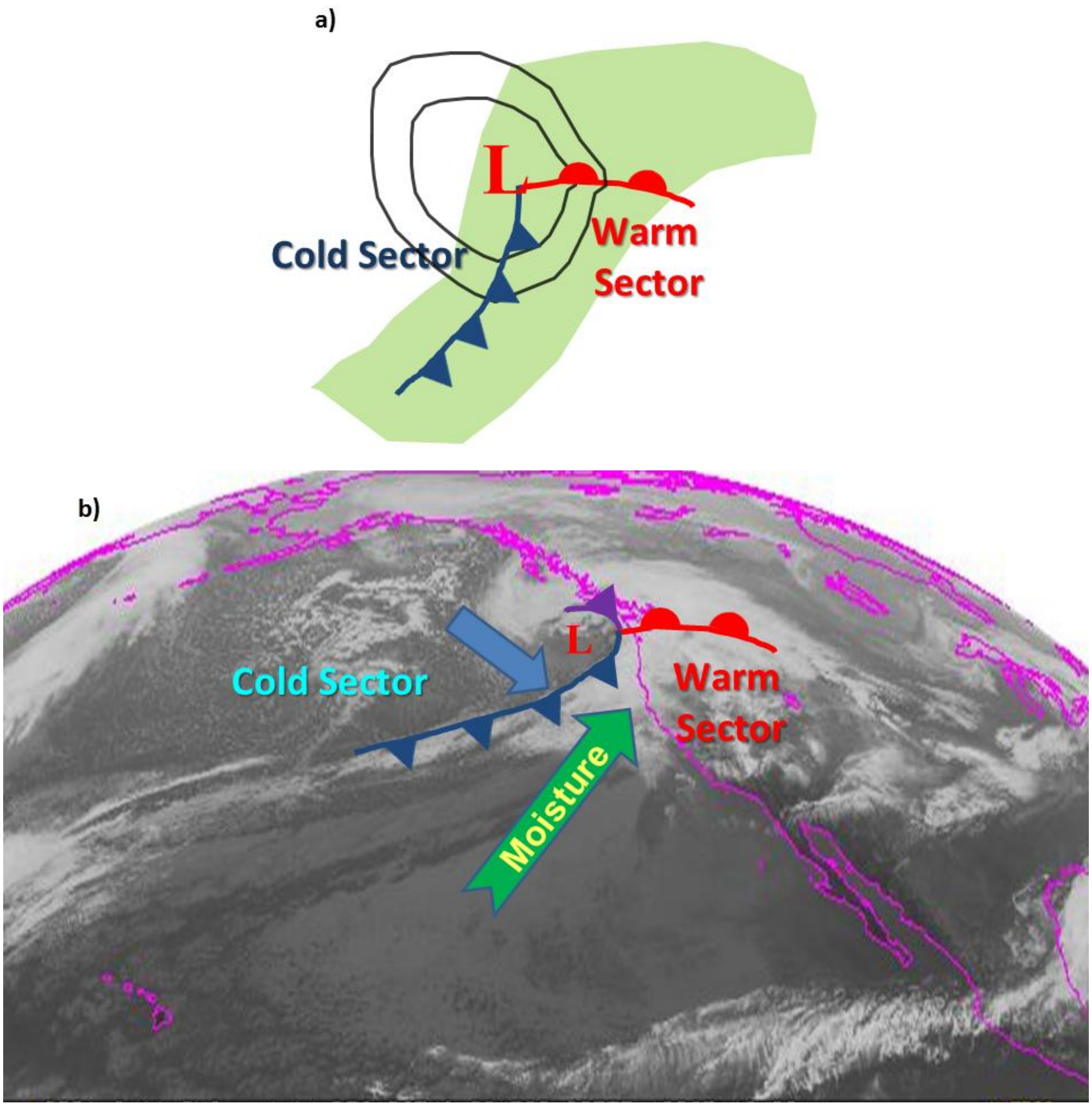

FIG. 1.3. Norwegian cyclone model examples. Panel a) Norwegian cyclone conceptual model, where the L is the surface low pressure center, the red line with circle hatches is the surface warm front, the blue line with triangle hatches is the surface cold front, the green shaded region is precipitation, and gray lines are surface isobars. Panel b) GOES IR image with Norwegian cyclone conceptual model features overlaid

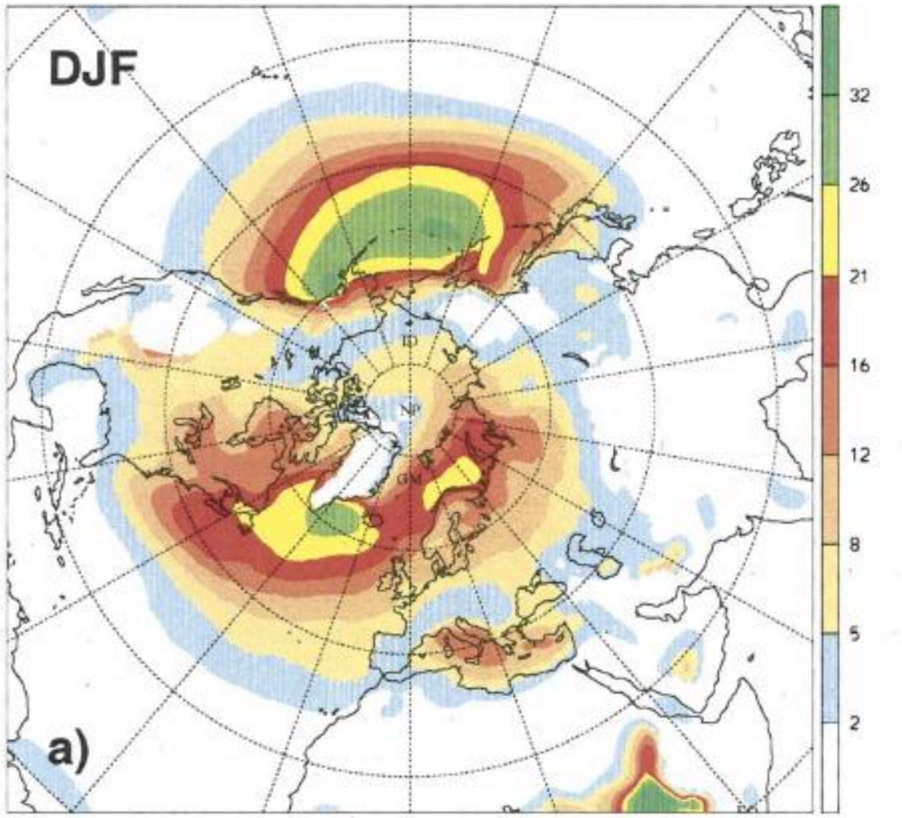

FIG. 1.4. Seasonal mean cyclone frequency (%) in the Northern Hemisphere for the ERA-40 period 1958-2001 for December, January, February. The field is not plotted in regions where the topography exceeds 1500 m (Wernli and Schwierz, 2006, their figure 4).

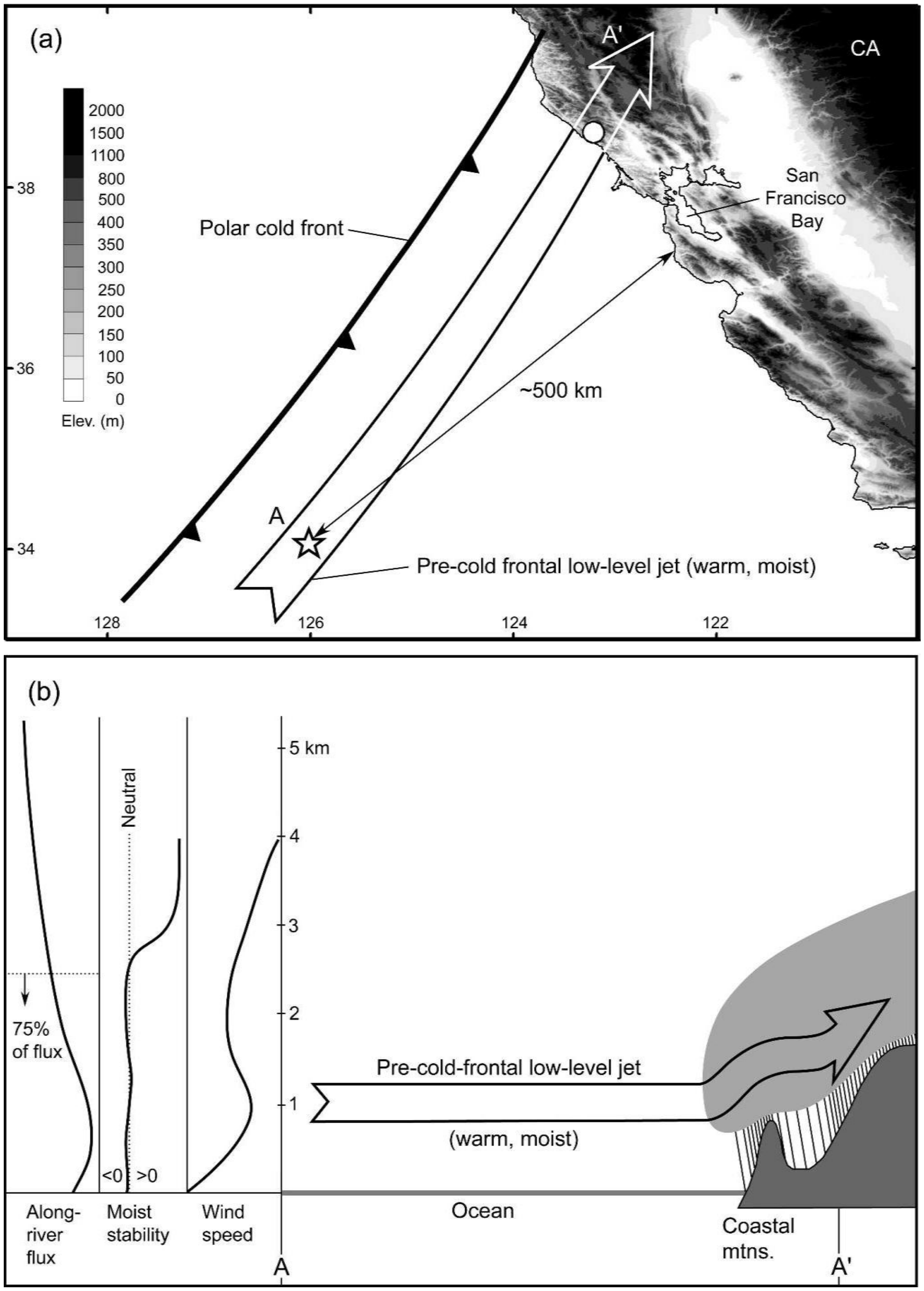

FIG. 1.5. Conceptual representation of land-falling extratropical cyclone conditions. a) Horizontal cross-section view, b) Vertical cross-section view (from Fig. 13 of Ralph et al., 2005).

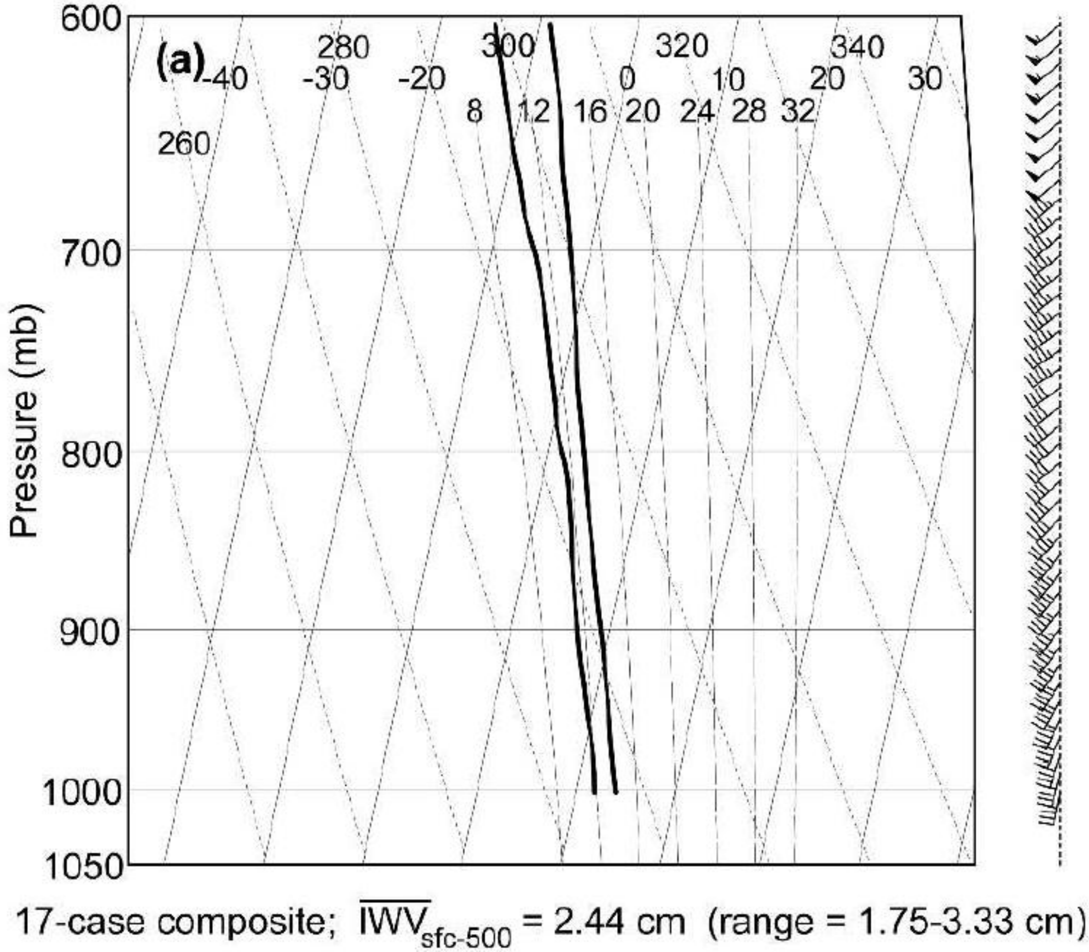

FIG. 1.6. Skew T-logp portrayal of the composite mean sounding (100-m vertical resolution) based on the 17 pre-cold-frontal dropsondes from CALJET-1998 and PACJET-2001 (from Fig 4.a. of Ralph et al., 2005).

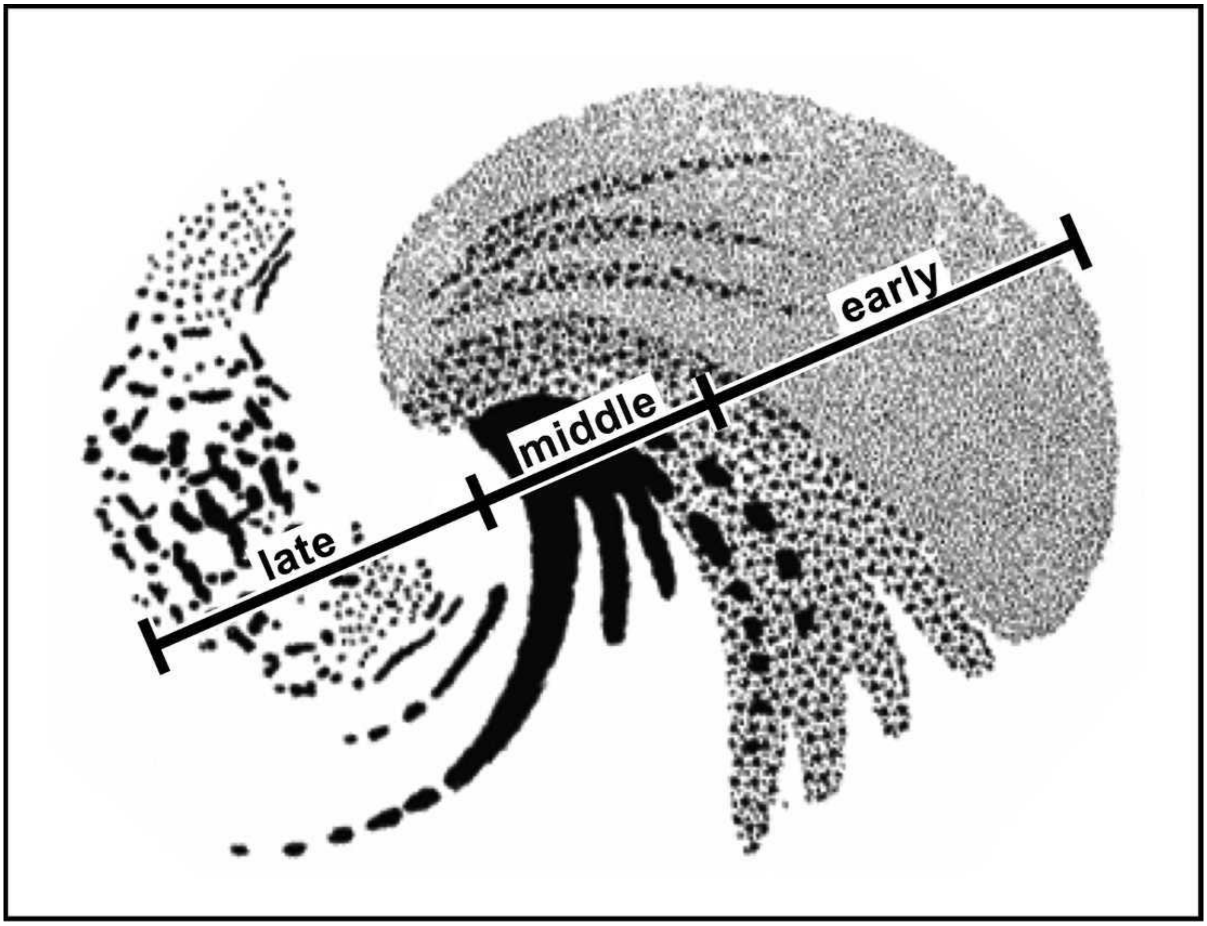

FIG. 1.7. Idealized precipitation pattern of an eastern Pacific extratropical cyclone. The precipitation intensity is indicated by the degree of the shading. The line segments indicate the early, middle, and late sectors of the storm as the terms are used in this study. Adapted from Nagle and Serebreny (1962) by Medina et al. (2007).

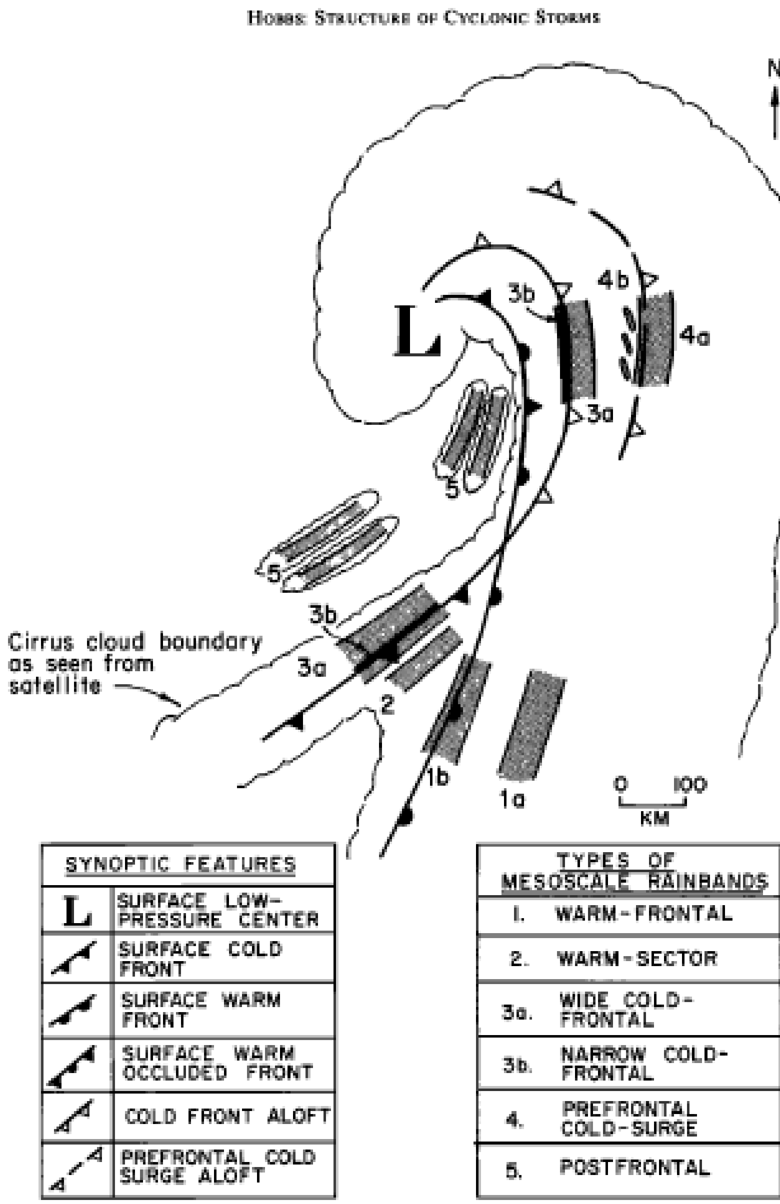

FIG. 1.8. Schematic of the types of rain bands located near extratropical cyclones. (Hobbs, 1978)

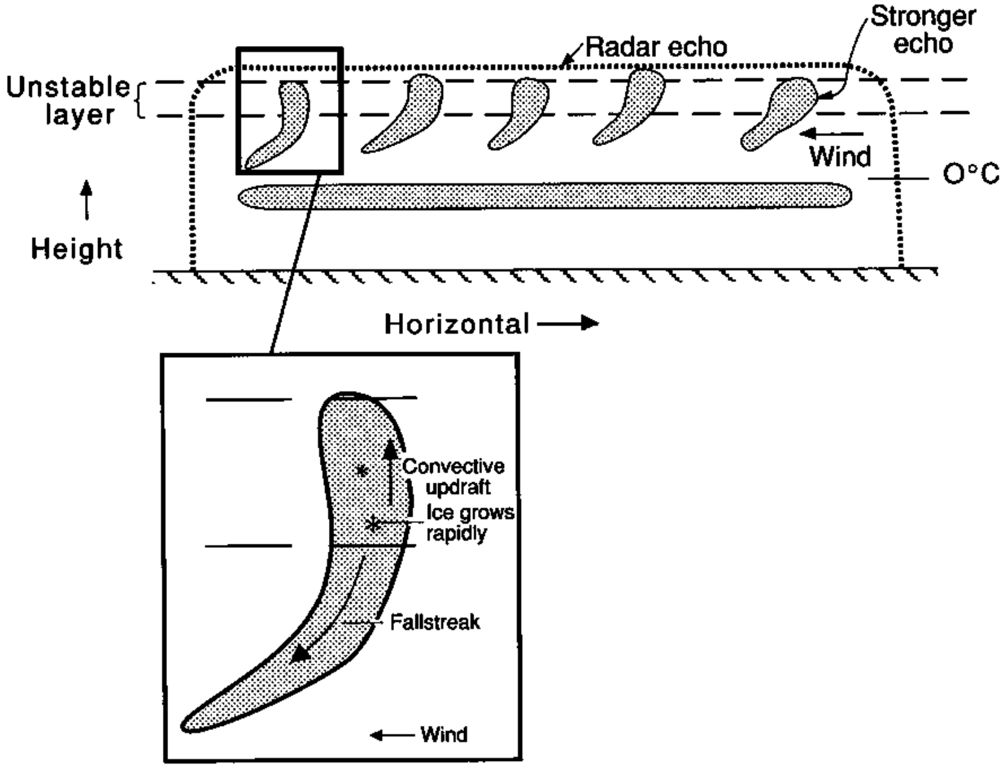

FIG. 1.9. Seeder-feeder mechanism. Generating cells are illustrated with idealized radar echo (Houze 1993).

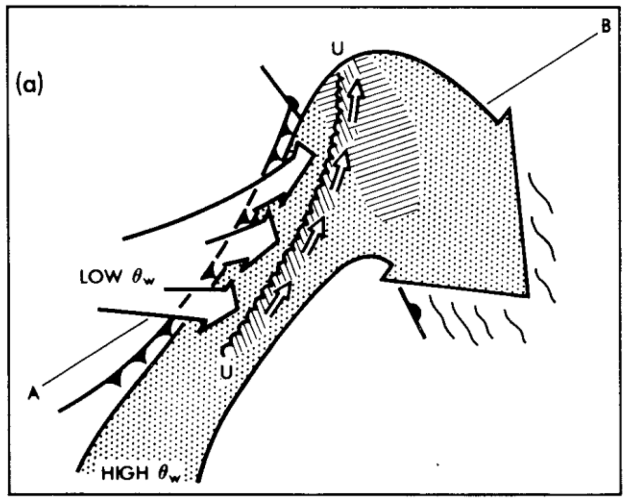

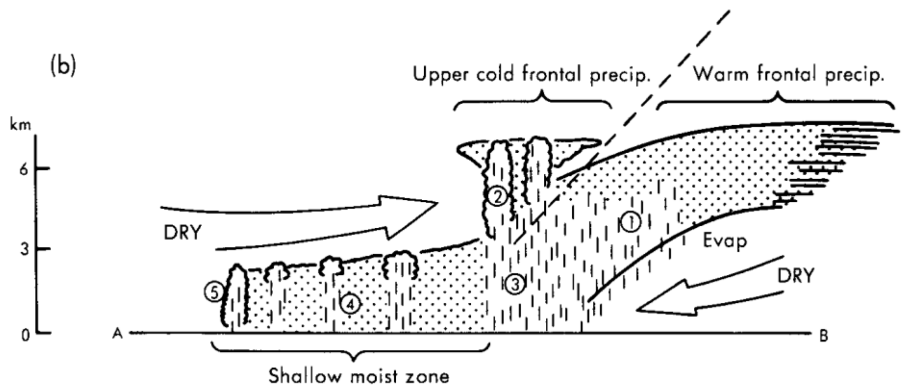

FIG. 1.10. Forward tipped cold front a) Plan view of warm conveyor belt with forward-sloping ascent. The large hatched arrow represents the warm conveyor belt, and the white small arrows represent dry cooler air aloft moving over the moist warm conveyor belt introducing upper-level instability. In the split cold front, the warm conveyor-belt is tipped back over the surface cold front. b) Vertical section along AB - 1) warm frontal precipitation, 2) convective precipitation-generating cells with the upper cold front, 3) precipitation from the upper cold frontal convection descending through an area of warm advection, 4) shallow moist zone between the upper and surface cold fronts characterized by warm advection, 5) shallow precipitation at the surface cold front itself (From Fig. 5 Browning and Monk, 1982; Browning, 1986).

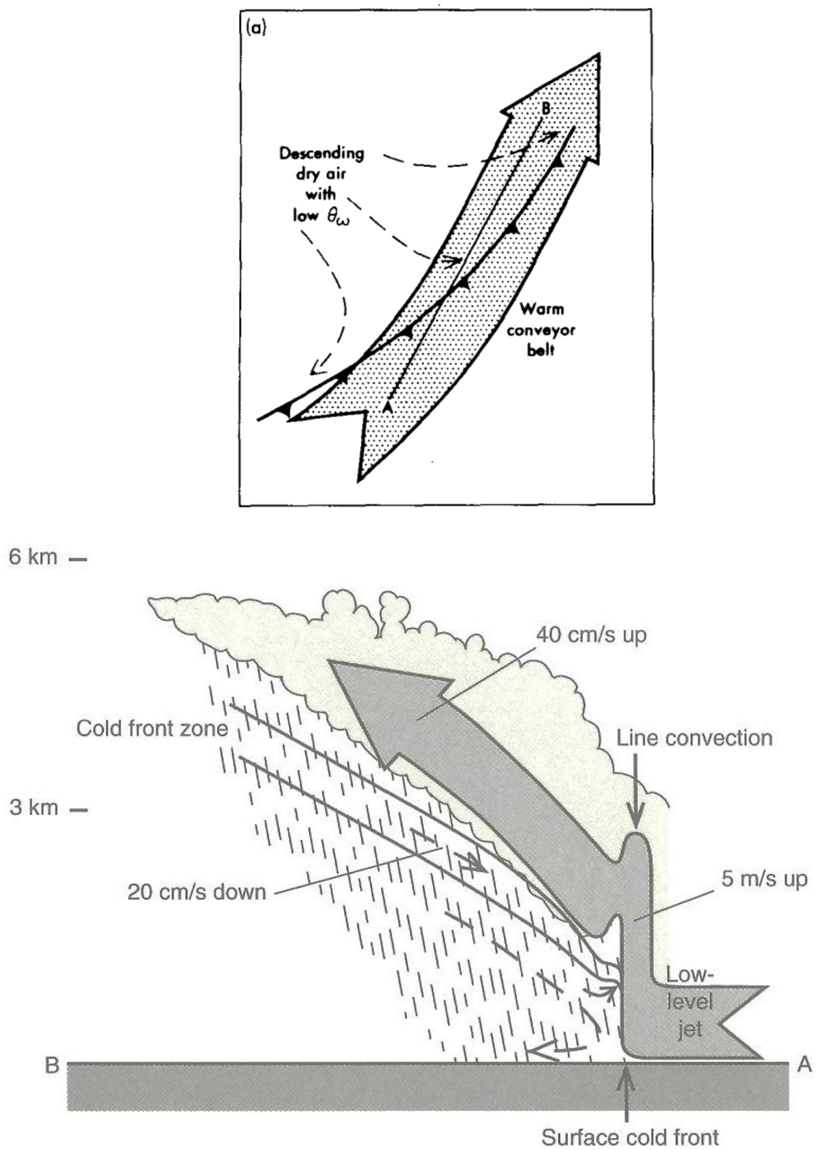

FIG. 1.11. Traditional cold front a) Plan view of warm conveyor belt with rearward sloping ascent. The large hatched arrow represents the warm conveyor belt, and the dashed small arrows represent dry cooler air aloft moving over the moist warm conveyor belt (Browning, 1986) and b) vertical cross-section of a traditional cold front showing airflows relative to the system (adapted by Bader et al. 1995 from Browning, 1986)

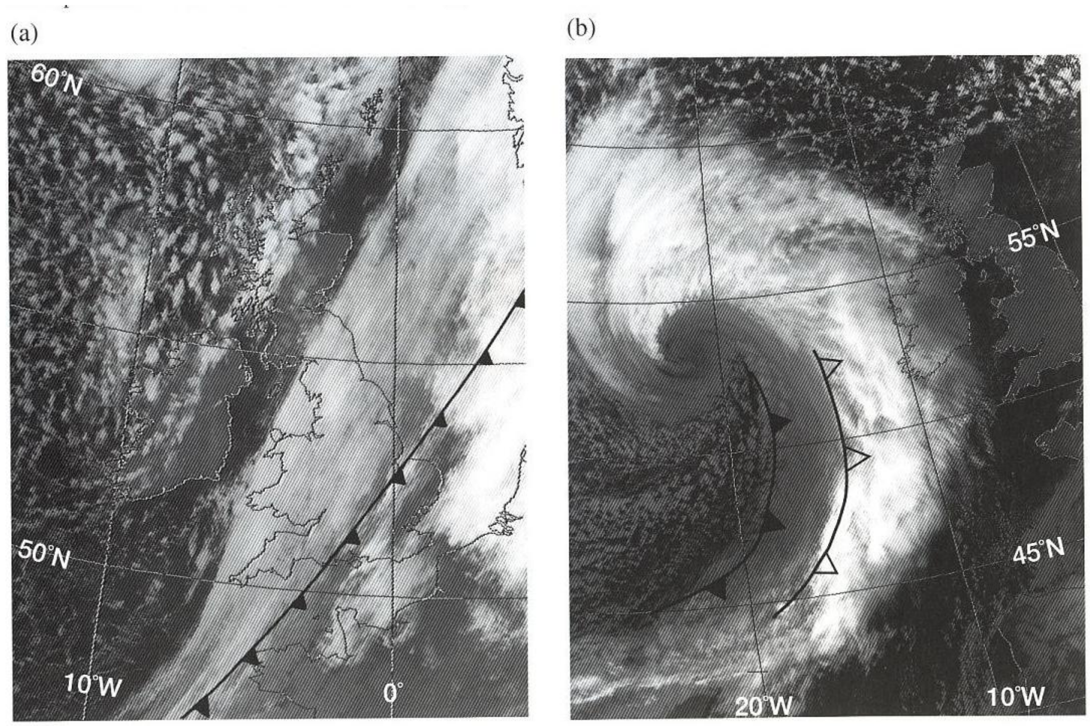

FIG. 1.12 – Infrared satellite images of a traditional cold front and a split-cold front. Panel a) a classical cold front: NOAA-11 image at 0302 UTC 14 January 1989, b) a split cold front: NOAA-10 image at 0847 UTC on 21 February 1989 (from Bader et al., 1995).

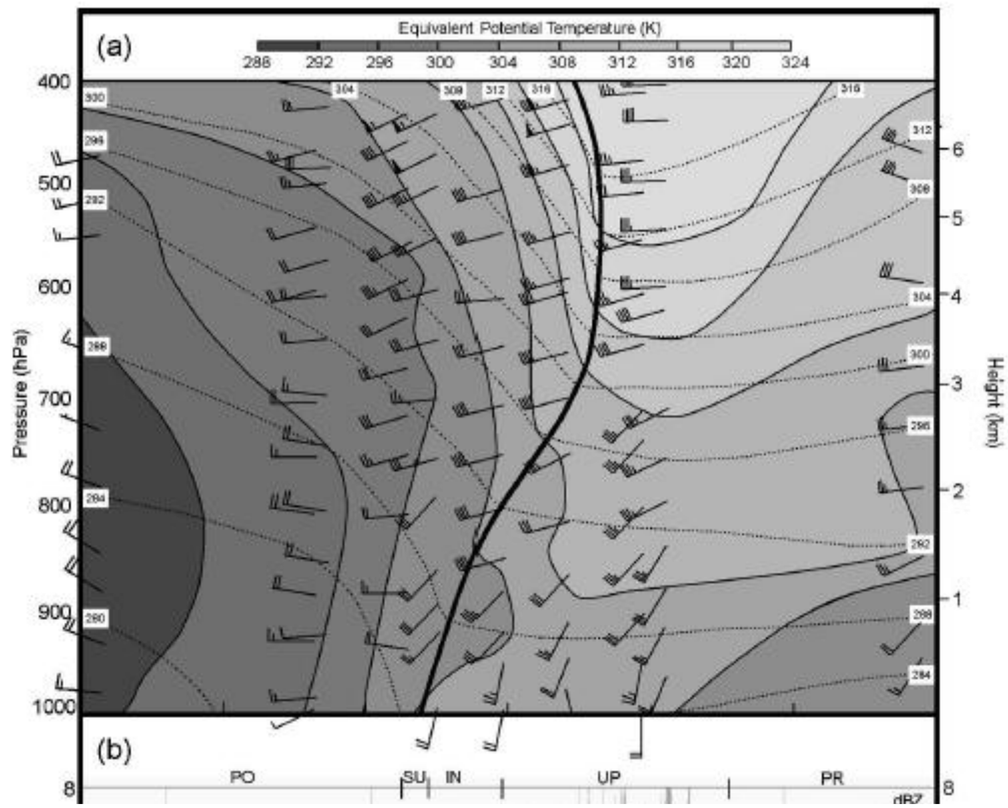

FIG. 1.13 – Examples of observed potential instability associated with a forward bent cold front for the 13 December 2001 IMPROVE- 2 storm. Thick solid vertical line is the analyzed cold front location (Woods et al., 2005).

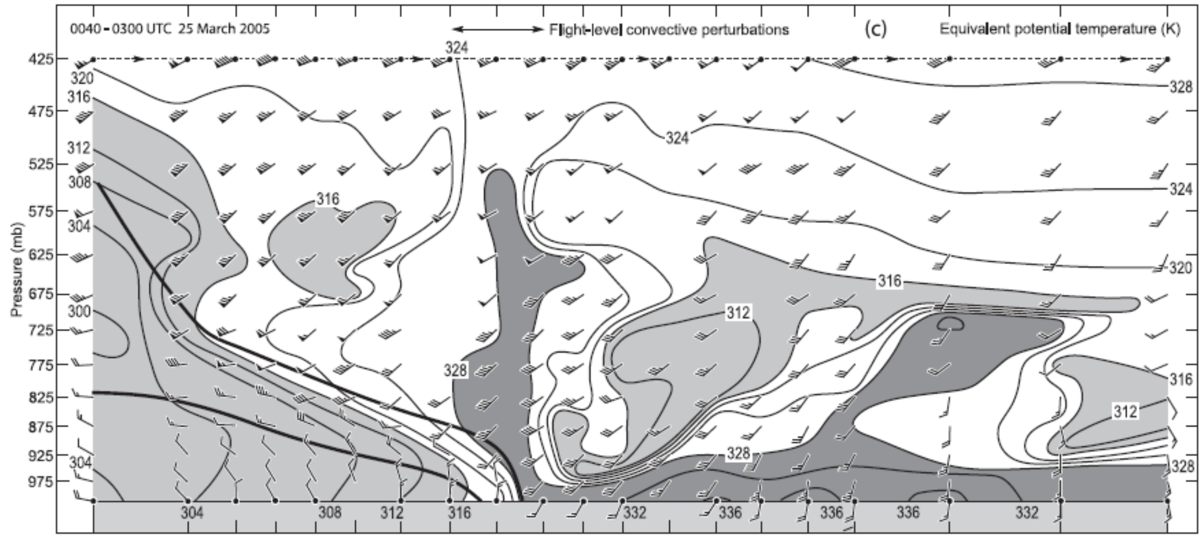

FIG. 1.14 – Example of observed potential instability ahead of upper-level trough/surface cold front. Figure 8 from Ralph et al. (2011) showing the cross-section of a cold frontal region and atmospheric river over the open Pacific Ocean north of Hawaii. Frontal boundaries are indicated by black boldface lines.

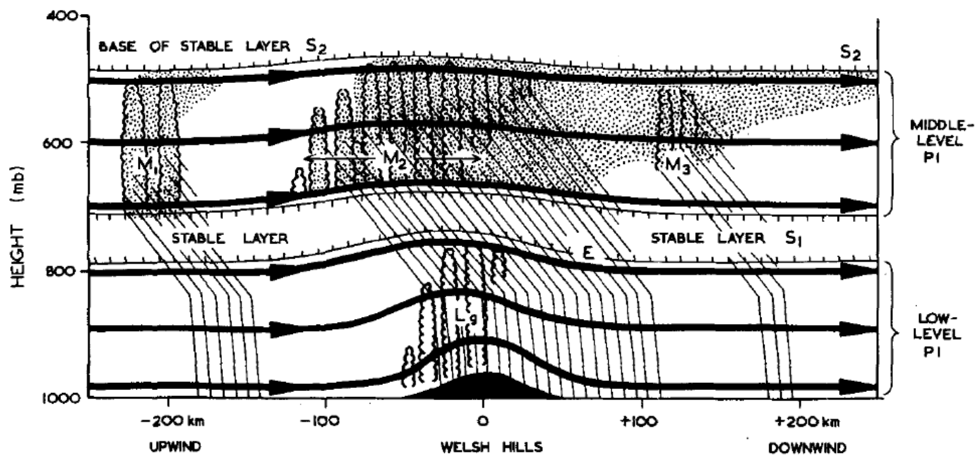

Figure 12. Model showing dependence of warm sector rainfall on potential instability and orography. See Key for explanation of symbols.

Mean streamlines within the strong west-south-west flow crossing the Welsh hills, drawn to be consistent with the observed pattern of precipitation development; although the precise form of the streamlines is arbitrary, notice that the middle-level air begins to ascend far upwind of the hills.

S_1 Layer with rather high static stability separating the potentially unstable air at low levels from potentially unstable air at middle levels.

S_2 Base of the region of high static stability that extends throughout the upper troposphere.

Small scale convection occurring where the low-level or middle-level potential instability (PI) is realized by general ascent.

Ice crystal (anvil) 'cloud' resulting from the middle-level convection and perhaps also, above 500 mb, from stable ascent over the hills.

Precipitation trajectories relative to the ground, strongly inclined because of the high winds; the change in slope occurs at the melting level at about 840 mb.

M_1 Middle-level convection within isolated MPAs due to areas of mesoscale ascent that occur in the warm sector even over the sea.

$\longleftarrow M_2 \longrightarrow$ Abundant middle-level convection triggered by orographic uplift over the hills, occurring as fresh outbreaks within and between existing MPAs.

M_3 Decaying middle-level convection mainly associated with MPAs previously in existence far upwind of the hills (i.e. M_1).

L_g Rapid low-level growth of precipitation falling from aloft, producing a large increment in rainfall rate tied closely to the hills.

E Evaporation in the lee of the hills, decreasing the amount of precipitation from middle-levels that reaches the ground over central England; however, because of the enhanced generation of precipitation over the hills (M_2) widespread rain continues to fall up to 100 km downwind of the hills.

FIG. 1.15. This figure from Browning et al. (1974) illustrates a conceptual model of potential instability aloft with seeder cells generating ice crystals over a stable moist layer. Precipitation is preferentially enhanced over the hills, but not absent over the water.

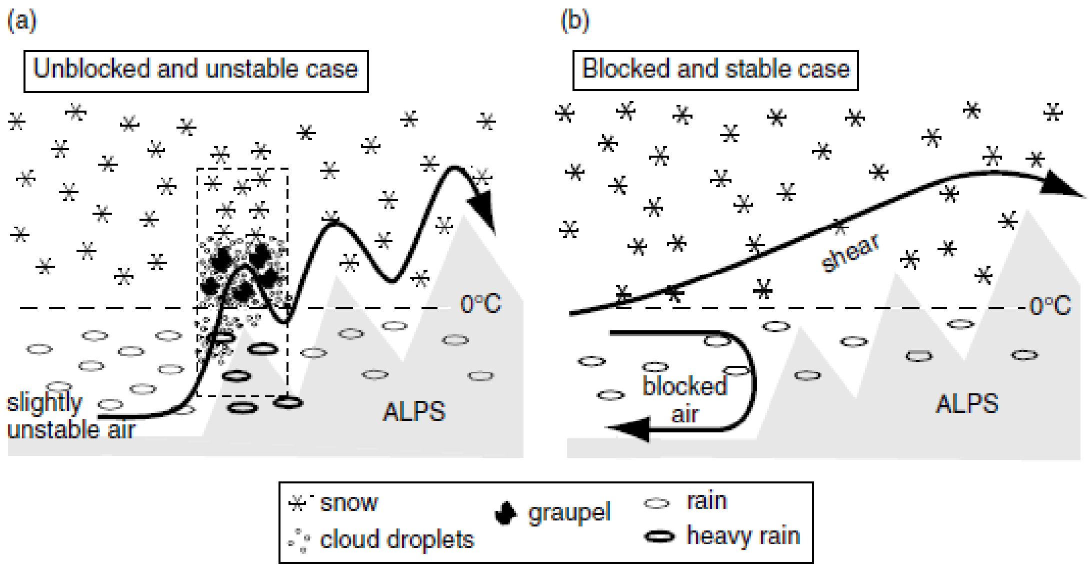

FIG. 1.16. Two modes of cellularity as observed during Mesoscale Alpine Programme and Houze and Medina (2005) (from Rotunno and Houze, 2007).

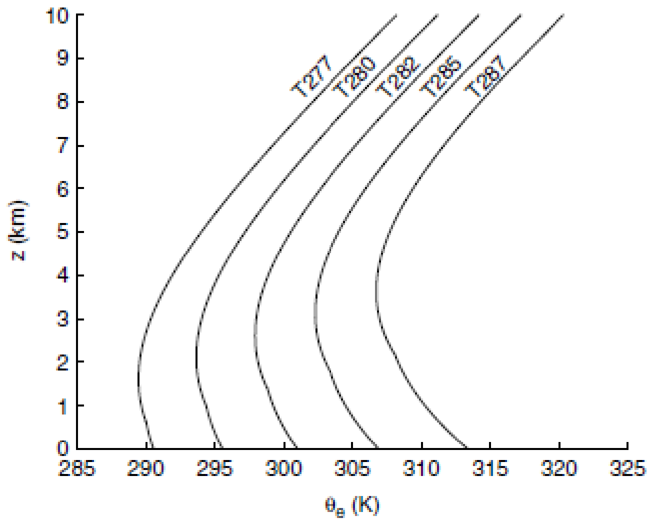

FIG. 1.17. Equivalent potential temperature profiles as a function of surface temperature used for model sensitivity tests to determine the impact of embedded convection on precipitation created by moist flow over terrain (from Cannon et al., 2011).

Chapter 2 – Research Objective and Hypothesis

There is lack of consensus in the literature regarding the primary mesoscale mechanisms responsible for intermittent, convective cells embedded within broader stratiform precipitation in the Pacific Northwest. As discussed in the literature review, studies attribute cellularity in the Pacific Northwest to hydrostatic instability or to hydrodynamic instability (such as vertical wind shear instability or conditional symmetric instability). However, they fail to quantify, with long-term datasets, the location and magnitude of either type of mesoscale instability. Does increased cellularity come from increased near surface buoyancy (hydrostatic instability) or vertical wind shear instability (hydrodynamic instability), as implied by Rotunno and Houze (2007)? Or does increased precipitation intermittency and variability come from elevated hydrostatic instability, in conjunction with the seeder-feeder mechanism (Browning et al., 1974; Rutledge and Hobbs, 1983, Locatelli et al., 2005)?

The lack of consensus in recent literature points to a need for more observational work to identify general mechanisms responsible for intermittent, cellular precipitation. In response to these questions, I developed an automated and objective method for identifying intermittent, cellular precipitation structures in large multi-year radar datasets. The information about precipitation structure is then combined with additional atmospheric characteristics to identify associated hydrostatic instability mechanisms. New and old algorithms are employed in a novel two-step process to detect intermittent, cellular precipitation near Portland, Oregon. Step 1 applies the theoretical framework outlined in Houze (1997) and the practical algorithm described in Steiner et al. (1995) and Yuter et al. (2005) to operational radar data. The second step characterizes precipitation intermittency in the time dimension. Four different modes of precipitation intermittency over 3-hour periods are identified: 1) mostly stratiform, 2) embedded convective within stratiform precipitation, and 3) mostly convective, which vary from least intermittent to most intermittent. A fourth "other" mode is used for uncategorized periods.

Previous research and theory demonstrate that three ingredients must be present for convective-type precipitation to occur: moisture, lift, and hydrostatic instability (Schultz and Schumacher, 1999). Logically, cases should be examined for hydrostatic instability first, before conditional symmetric instability (Schultz and Schumacher, 1999; McCann, 1995). Furthermore, assessment of conditional symmetric instability requires observational data with high 3D resolution. Assessment of hydrostatic instability is possible with even a coarse sounding network. For these reasons, this study will be restricted to assessing hydrostatic instability and wind shear instability of precipitation with varying degrees of intermittency. Averaging soundings and radar data tends to lose important information regarding the variability of the data. Effort is taken to avoid losing important information during statistical analysis.

My general hypothesis is that as cool season precipitation near Portland, Oregon becomes more intermittent, the precipitation periods will have increased frequency of vertical profiles with positive buoyancy. Specifically, the frequency of precipitation periods with positive buoyancy (as measured by most unstable parcel convective available potential energy[4]*) should be higher (> 2x) for embedded convective within stratiform precipitation periods than for mostly stratiform precipitation periods*. When buoyancy is not present, other factors, such as potential instability, vertical wind shear instability, conditional symmetric instability, frontal forcing, etc. are possible causes of cellular embedded precipitation. Due to reasons described earlier, only hydrostatic instability and the vertical wind shear instability are addressed in this study. The altitude of the instability also has to be assessed, since this has implications for the relative importance of different microphysical processes (such as the seeder-feeder mechanism).

[4] Convective available potential energy is defined in Chapter 3.

Chapter 3 – Data and Methodology

Previous large scale field experiments (CYCLES, IMPROVE, etc.) designed to study precipitation in this region employed specialized research instrumentation to conduct intensive observing periods, which in many cases included high resolution airborne radar, and ground-based scanning and vertically pointed radar. In general, operational datasets have coarser spatial and temporal resolution, but have much longer observational periods. In this study, operational datasets are used in conjunction with vertically pointing radar.

3.1 Instruments and Data

The primary observational dataset for this study are observations from the Portland, Oregon, National Weather Service (NWS) Level II Next Generation Weather Radar (NEXRAD) Weather Surveillance Radar-1988 Doppler (WSR-88D) from 2002 to 2008. These observations present a large, nearly continuous dataset (volume scan interval of approximately 6 min) for the period of interest. Traditional upper-air soundings from the NWS upper-air balloon located in Salem, Oregon (KSLE) and NWS METAR surface observations at Portland International Airport (KPDX) are available from 2002 to 2008. A METEK Microwave Rain Radar (MRR) provides vertically pointing radar data in Portland, OR from 2005 to 2008. Streamflow discharge was measured from the United States Geologic Survey's (USGS) Fanno Creek (56th Avenue) gage located near Portland, Oregon and is discussed in Appendix A. Instrument locations are identified in Figure 1.1 and metadata are located in a Table 3.1. Portland, Oregon is a good study domain because of the co-location of several operational and research instruments, which aids validation of results.

3.1.1 Portland, Oregon NWS WSR-88D (KRTX)

The KRTX WSR-88D is situated in the Willamette Valley (Fig 1.1). For most precipitation situations, this radar is operated with NWS volume coverage pattern 21, which scans 360 degrees at 9 elevation angles (0.5, 1.5, 2.4, 3.4, 4.3, 6.0, 9.9, 14.6, and 19.5 degrees) every 6 minutes (Fig. 3.1). The NWS WSR-88D has an approximately 1.0 degree beamwidth at the half-power point. KRTX WSR-88D data are archived in Level 2 format at the National Climatic Data Center located in Asheville, NC and are available over the Internet.   Most KRTX data for this study were from the constant 0.5 degree elevation. The effective horizontal resolution with this beam width allows for a horizontal grid spacing of 2 km out to a range of approximately 120 km, when the level 2 polar data are interpolated to a horizontal grid. Partial beam filling with ground targets is likely to occur in standard atmospheric refraction conditions for the 0.5 degree elevation slice in several mountainous locations (Doviak and Zrnik, 1993). Special care was taken to filter out these locations in the radar data processing (Fig 3.2).

KRTX File Quality Control and Interpolation Processing

Level 2 NEXRAD files were processed into universal format (UF) polar coordinate files using a process developed by David Kingsmill (personal communication). Quality control was performed on the UF files by removing clutter and anomalous propagation via a processes developed by Sandra Yuter (personal communication). Quality controlled UF files were then interpolated into NETCDF Cartesian coordinate files (2 km horizontal grid-spacing) within the domain identified in Figure 3.3 with Reorder software (NCAR, 2012).

3.1.2 Vertically Pointing Radar

The MRR is vertically pointing K-band (24.1 GHz) radar (Loffler-Mang et al. 1999; Peters et al. 2002) located 38 km to the southeast of KRTX (Fig 1.1). This instrument has a beamwidth of 1.5° and was setup with a vertical range up to 4.5 km altitude and a gate spacing of 150 meters. Radar reflectivity and Doppler vertical velocity (V_D) are recorded every 1 minute. With the K-band radar, reflectivity values are subject to signal attenuation during heavy precipitation. Therefore, specific values of reflectivity in the vertical are unreliable above heavy precipitation regions. Relative values of reflectivity are still useful for identifying fallstreaks in snow. Attention is required to ensure that false fallstreaks created by attenuation from high reflectivity in the rain layer of precipitation are identified as artifacts.

The Doppler Vertical Velocity (V_D) for the MRR is defined in the radial direction as

$$V_D = V_P + V_A,$$

where, V_P is the hydrometeor fall velocity and V_A is the speed of the air. V_P is dependent on hydrometeor type. Positive values of V_D are moving towards the radar (i.e. down or towards the ground) and negative values are moving away from the radar (i.e. up or towards space). Doppler vertical velocity data are reliable through the entire column because they are not affected by signal attenuation.

3.1.3 NWS Upper-Air Sounding (KSLE)

The Salem, Oregon NWS upper-air sounding is the nearest operational sounding available for the study domain (89 km south of KRTX). Data from the sounding are used to describe the vertical profile of wind, wind shear, temperature, moisture, and buoyancy instability. The KSLE sounding is only available every 12 hours and the location is on the southern end of the domain. KSLE is available for the entire 6 year study period.

3.1.4 NWS METAR Surface Observation (KPDX)

The KPDX METAR surface observation station is located at the Portland International Airport and is 32 km to the southeast of KRTX. KPDX provides standard hourly and special observations for the airfield. Daily precipitation data were examined to identify days with significant precipitation using the criteria applied in Yuter et al. (2011). A significant precipitation day is defined as a day with 5 mm of accumulated precipitation or a surrounding day with 2.5 mm of accumulated precipitation. Only KRTX data on significant precipitation days were examined for intermittent precipitation.

3.1.5 National Lightning Detection Network (NLDN)

National Lightning Detection Network (NLDN) data, a product of Väisälä, were provided courtesy the United States Air Force 14th Weather Squadron in Asheville, NC. Near Portland, Oregon, NLDN has a cloud-to-ground lightning strike accuracy of less than 500 meters and a detection efficiency of greater than 90% (Väisälä, 2012).

3.2 Two-Step Intermittency Detection Process with Operational Scanning Radar Data

Identification of intermittent precipitation with operational scanning radar occurs in a two-step process. First, a convective-stratiform algorithm is applied to the low level 2D gridded horizontal reflectivity data to decompose the data into precipitation structure type. Second, the convective-stratiform algorithm output is analyzed in the time dimension to detect precipitation intermittency. The convective-stratiform algorithm applied in the first step has a long history of use and is founded on a theoretical framework for using precipitation radar to distinguish convective (intermittent) type precipitation from stratiform type precipitation (Houze, 1997). The framework infers different dynamical and microphysical processes for each type of precipitation, based on horizontal radar reflectivity gradients. Houze (1997) defines convection as a noun, and convective and stratiform as adjectives. Convection occurs with vertical air motions of 1-10 m s^{-1}. Convective-type precipitation on a radar echo is associated with young active convection and forms as a result of collision and coalescence (liquid phase) and riming (ice phase clouds). Riming occurs when precipitation sized ice crystals, move through supercooled water droplets. The supercooled cloud droplets collide with and freeze on the ice crystals (Cotton et al. 2011). Stratiform describes the type of precipitation associated with weak vertical air motions (1-2 ms^{-1} - i.e. upward vertical motions that are small relative to the fall speed of ice crystals and snow). In these vertical velocity conditions hydrometeors primarily grow as a result of vapor deposition in the ice phase. Stratiform precipitation occurs at the mesoscale in areas of old convection or at the synoptic scale in areas of gentle uplift, such as warm fronts. In radar reflectivity data, convective precipitation tends to appear as areas of locally enhanced reflectivity with sharp horizontal reflectivity gradients (Fig 3.6). Convective precipitation is associated with vertical columns of reflectivity. Stratiform precipitation tends to appear in radar reflectivity data as regions of weak horizontal gradients with varying vertical thickness. A bright band may also be apparent in a vertical cross-section of reflectivity data for stratiform precipitation when melting associated with the 0° C level is located within a narrow layer resolvable by the observing radar. The bright band is a layer of enhanced reflectivity values associated with melting hydrometeors.

Hobbs et al. (1980) illustrates an excellent example of the impact of convective versus stratiform precipitation on rain gage derived rain rate with a case from 17 November 1976. At several different rain gages, rain rates sharply increased with the passage of each mesoscale rainband, sub-band, and precipitation cores (their Figs. 5 & 6). The rainbands, sub-bands, and precipitation cores would likely have been identified as convective-type precipitation using the Houze (1997) framework. Appendix A highlights an example of how convective and stratiform precipitation can impact streamflow in a small urban watershed near Portland, Oregon.

3.2.1 Step 1 - Convective-Stratiform Identification (CONVSF) Algorithm

The convective/stratiform algorithm (CONVSF), originally defined by Churchill and Houze (1984) and adapted by Steiner et al. (1995), Houze (1997), and Yuter et al. (2005), was tuned to work with data from KRTX by subjectively examining echo structure within vertical cross-sections from a number of cases. Churchill and Houze (1984) developed the algorithm for radar data from the tropics in an effort to objectively quantify the unique contributions of stratiform and convective precipitation to rainfall totals. The algorithm is a practical application of the theoretical concepts described in Houze (1997) for identifying convective radar echoes with two dimensional radar data. The algorithm categorizes every pixel in a two-dimensional gridded data field as convective, stratiform, or weak echo, beginning with convective pixels first. Figure 3.6a-h illustrates how the algorithm would decompose a two dimensional gridded array of reflectivity for precipitation events with different structures.

The CONVSF algorithm was designed to work in the tropics, so two adjustments to the criteria were required for it to work in the Pacific Northwest. The first adjustment is to turn-off the intensity requirement for the identification of convective cores. As described in the background section and highlighted in past studies, the regional cool season intermittent precipitation is shallow (relative to deep moist tropical convection) and embedded within broad stratiform precipitation with high reflectivity values. Hence, it became necessary to utilize the detection of peakedness (sharp gradients) within the reflectivity field for the identification of convective cores. The second adjustment was to increase the sensitivity of the peakedness criteria by adjusting parameter *a* in equation B1 of Yuter and Houze (1997) from a setting of 8 to a setting of 4. Decreasing this parameter increases the algorithm's sensitivity to horizontal reflectivity gradient changes. The setting was chosen by examining a large number of cases with an ensemble of parameter values. By using a fixed sensitivity parameter, relative changes in algorithm output can be used to understand underlying precipitation structure changes.

3.2.2 Step 2 - Intermittent Precipitation Detection Algorithms

Building on the convective-stratiform algorithm as a foundation, a new methodology was developed to objectively quantify changing spatial and temporal characteristics of intermittent precipitation associated with extratropical cyclones. First, the convective-stratiform algorithm is applied to a cool season's worth of two dimensional reorder NetCDF reflectivity files (significant precipitation days only). Then, all cool season precipitation events are sub-divided into 3-hour periods. Calculations for the frequency of precipitation, frequency of convection, and convective-stratiform intermittency are performed for each grid point for each 3-hour period. Performing the calculations over 3-hour periods ensures a sufficiently large number of radar volumes to perform calculations (about 30 volumes during a 3-hour period), but is not too long of a period to average (i.e. "mask" or "washout") meaningful spatial and temporal characteristics of the precipitation.

Figure 3.4 shows the evolution of a hypothetical convective cell moving from the bottom left to the upper right. As the cell moves over the red highlighted box the precipitation type changes from weak echo, to stratiform, to convective, back to stratiform, and finally back to weak echo again. By storing the precipitation type for each grid point for a 3-hour period, one can define several variables related to precipitation occurrence and intermittency. Table 3.2 is a rubric for interpreting the calculations below. Each variable is calculated at each grid point in the radar data domain.

Frequency of Precipitation

Frequency of precipitation is a common calculation used to identify geographic locations of preferred or enhanced precipitation and is often used in orographic precipitation studies. Yuter et al. (2011) defines the frequency of precipitation for each grid point as the number of pixels with $Z \geq 13$ dBZ divided by the total number of pixel opportunities for the time period (i.e. the total number of radar volumes in 3 hours).

$$\text{Frequency of Precipitation} = 100 \times \frac{\#\ of\ Precipitating\ Pixels}{\#\ of\ Opportunities}$$

A precipitating pixel is defined as any pixel categorized as convective or stratiform. In this study, the calculations for frequency of precipitation are calculated for 3-hour periods not 12-hour periods used in Yuter et al. A frequency of precipitation equal to 100% means that precipitation is always occurring at a grid point, whereas a frequency of precipitation equal to zero means that precipitation never occurs at a grid point.

Frequency of Convective Precipitation

The frequency of convective precipitation is defined as:

$$\text{Frequency of Convective Precipitation} = 100 \times \frac{\#\ of Convective\ Pixels}{\#\ of\ Precipitating\ Pixels}$$

.

Although the frequency of convective precipitation is an Eulerian calculation, it implicitly represents the two dimensional peakedness criterion of the data as identified by the CONVSF algorithm. Frequency of convective precipitation equal to 100% means that the grid point is always identified as convective. A frequency of convective precipitation equal to zero means that a grid point is never convective and is always stratiform. A frequency of convective precipitation equal to 50% means that the grid point is stratiform precipitation half of the time and convective precipitation the other half of the time it is precipitating.

Convective-Stratiform Intermittency

Convective-stratiform intermittency addresses the relative amount of time the precipitation remains as one mode (either convective or stratiform) before changing to the other. Convective-stratiform intermittency is defined as:

$$\text{Convective - Stratiform Intermittency} = 100\% \times \frac{\#\ of\ Transitions}{\#\ of\ Precip.Opportunities}$$

Low values of convective-stratiform intermittency imply the period experiences convective or stratiform continually for most of the raining period. High values indicate that each mode existed for a relatively short period before changing.

Making Sense of Frequency of Precipitation, Frequency of Convective Precipitation, and Convective-Stratiform Intermittency

Interpreting each of these measures individually yields important information about precipitation at each radar grid point, but interpreting the measures together for all grid points yields additional information about the nature of the precipitation intermittency in the domain for a 3-hour period of time. Figure 3.5, illustrates conceptually the convective/stratiform intermittency and frequency of convective precipitation phase space. For purposes of establishing a categorical description of the region's precipitation structure, the phase space is divided up into several regions. The first region is the mostly stratiform mode, which is described as frequency of convective precipitation less than 33%. The second mode is the embedded convective within stratiform, which is defined as frequency of convective precipitation less than 66%, but more than 33% and convective-stratiform intermittency greater than 33%. Mostly convective precipitation is the third mode, which is defined as the frequency of convective precipitation greater than 66%. Finally, the fourth mode is the "other" mode that is convective or stratiform for about half of the time, but has a low convective-stratiform intermittency (< 33%). Fig 3.6i-l illustrates how the phase-space looks as data density diagram with real reflectivity data from a 3-hour period. A single reflectivity image from the 3-hour period is displayed in Fig 3.6a-d, with corresponding CONVSF algorithm output. The region on the categorical graph (Fig. 3.5) with the highest frequency of occurrence is classified as the 3-hour period's dominant precipitation mode. Although the clear lines of distinction are helpful for interpretation, it is also important to remember that the convective/stratiform intermittency and frequency of convective precipitation phase space is actually a continuum.

Prior to establishing the dominant precipitation mode for a 3-hour period, four quality assurance steps are applied to the data. The first two quality assurance steps remove bright band contaminated data. The first step discards all 3-hour periods within 6 hours of a sounding with a 0° C level below 1.4 km. The second quality assurance step filters out data in the radar domain beyond a radius of 70 km from KRTX, the approximate range of a bright band impact on the 0.5° elevation slice under standard refractive conditions. The third step applies the partial beam filling filter (Fig. 3.2) to remove locations with possible partial beam filling (i.e. non-meteorological echo). After the first three quality assurance steps are complete, the final step ensures enough data points are available for calculations by checking for at least 250 pixels with persistent precipitation (1000 km^2; must have a frequency of precipitation $\geq$ 30%). Finally, the dominant precipitation mode is found for each remaining 3-hour period. The two-step intermittent precipitation identification process is a robust and objective method for identifying intermittent precipitation structures in large scanning radar datasets.

3.3 Mesoscale Instability

Although synoptic scale factors are a major influence on the Pacific Northwest atmospheric environment, mesoscale instabilities and forcing mechanisms cause locally vigorous vertical motions which lead to convective precipitation. Convection (the noun) refers to vertically oriented turbulent overturning air motions due to an imbalance of forces in the vertical (Markowski and Richardson, 2010). Typically, convection occurs as a result of the release of hydrostatic instability. Hydrodynamic instabilities, such as vertical wind shear instability or conditional symmetric instability can also result in vertical accelerations.

However, this present work only focuses on comparisons of hydrostatic instability and vertical wind shear instability.

Convection, occurring as a result of a vertical acceleration due to hydrostatic instability, happens when a parcel of air becomes positively buoyant. This occurs when the temperature of the parcel is warmer than the environment. The equation of motion for this relationship is written as:

$$\frac{d^2\Delta z}{dt^2} = B = g\left(\frac{T - \bar{T}}{\bar{T}}\right)$$

where Δz is the displacement in the vertical direction, B is buoyancy, T is the parcel temperature, and $\bar{T}$ is the environmental temperature (environment is denoted by the overbar for other variables too), and g is the gravity constant (Markowski and Richardson, 2010). Under parcel theory, which assumes irreversible thermodynamics, the amount of available energy for updrafts in convection is defined as convective available potential energy (CAPE). CAPE is simply the integrated quantity of buoyancy, B, from the level of free convection (LFC) to the equilibrium level (EL): $CAPE = \int_{LFC}^{EL} B dz$. CAPE is often used to predict the theoretical maximum updraft speed, which is defined as $w_{max} = \sqrt{2CAPE}$. To calculate CAPE, Doswell and Rasmussen (1994) suggest finding the most unstable parcel within the lowest 300 mb ($\approx$ 3 km) (abbreviated as MUCAPE throughout this document) which may or may not be the surface parcel. The difference between the environmental temperature and the theoretical parcel temperature[5] is directly proportional to the amount of buoyancy a parcel experiences at each level. Negative values indicate that the parcel is warmer than the environment, which shows positive buoyancy. Positive values indicate negative buoyancy, while zero indicates zero buoyancy.

The environmental lapse rate determines whether or not a layer of atmosphere is considered hydrostatically unstable. Additionally, under parcel theory the environmental lapse rate influences the amount of buoyancy available to a parcel at each vertical level (the

[5] Calculations were based on the difference between the virtual equivalent potential temperature for the environment and the parcel ($\bar{\theta}_{eV} - \theta_{eV}$).

environmental temperature in the equation of motion is a function of the environmental lapse rate). In a dry atmosphere, a layer of air is considered absolutely unstable when the *potential temperature*[6] *($\bar{\theta}$)* decreases with height (z) or the environmental lapse rate is greater than the dry adiabatic lapse rate (Γ_d), such that

$$\frac{\partial \bar{\theta}}{\partial z} < 0 \text{ or } -\frac{\partial T}{\partial z} > \Gamma_d$$

A layer of atmosphere is labeled conditionally unstable when the *saturation equivalent potential temperature*[7] ($\overline{\theta_{es}}$) decreases with height or the environmental lapse rate is greater than the moist adiabatic lapse rate (Γ_m) but is less than the dry adiabatic lapse rate, such that:

$$\frac{\partial \bar{\theta}_{es}}{\partial z} < 0 \qquad \text{or} \qquad \Gamma_m < -\frac{\partial T}{\partial z} < \Gamma_d \,.$$

When the environmental lapse rate equals the dry adiabatic lapse rate or the moist adiabatic lapse rate, the stability of the layer is considered dry neutral or moist neutral, respectively. If a layer of atmosphere is saturated and the *equivalent potential temperature*[7], ($\overline{\theta_e}$) decreases with height ($\frac{d\bar{\theta}_e}{dz} < 0$), the layer of air is considered moist absolutely unstable (MAUL). If the layer of air is unsaturated and $\frac{d\bar{\theta}_e}{dz} < 0$, the layer is considered potentially unstable. A layer of air that is potential unstable can become moist absolutely unstable when saturation occurs through layer lifting or evaporation of water into the layer. Lifting an unsaturated potentially unstable layer causes the bottom of the potentially unstable layer to saturate before the top of the unstable layer. Due to moist adiabatic warming, the bottom of the layer warms faster than the unsaturated upper portion of the layer causing a hydrostatic imbalance. In the Pacific Northwest, conditions are usually saturated or nearly saturated near the surface during extratropical cyclone passage.

Unfortunately, parcel theory does not include factors such as the effects of pressure perturbations, the freezing of water droplets (release of latent heat of fusion), condensation,

---

[6] See Appendix C for definitions of potential temperature, saturation equivalent potential temperature, and equivalent potential temperature.

and hydrometeor loading on buoyancy and updraft speed. Pressure perturbations, condensation, and hydrometeor loading have a negative effect on buoyancy and updraft speed, while the release of the latent heat of fusion adds to buoyancy. Williams and Renno (1993) suggest that release of latent heat during the phase change to ice more than offsets water loading in the tropics. McCaul et al. (2005) also suggest that latent heat of fusion may be important for deep convection. It is not yet clear if the release of latent heat of fusion is an important factor in Pacific Northwest region, which experiences more shallow convection. CAPE is generally small during extratropical cyclone passage, but not insignificant. The inclusion of latent heat of fusion may be significant, since much of the convective precipitation occurs above the 0° C level.

A moist Richardson number (Ri), based on a simplified version of the moist Brunt-Väisälä frequency (N_m), is used to assess soundings for vertical wind shear instability (Kelvin-Helmholtz instability) where $Ri \equiv \frac{N_m^2}{\left(\frac{\partial \bar{u}}{\partial z}\right)^2}$ and $N_m = \left(\frac{g}{\overline{\theta_e}} \frac{\Gamma_m}{\Gamma_d} \frac{\partial \overline{\theta_e}}{\partial z}\right)^{1/2}$ (adapted from Markowski and Richardson, 2010). Kelvin-Helmholtz stability is assured for Ri > 0.25, but 0 < Ri < 0.25 is required, but not sufficient for instability. Houze and Medina (2005) observed vertical wind shear instability increasing precipitation cellularity near terrain. This present work examines the relationship of vertical wind shear instability to cellularity/intermittency over the Willamette Valley.

3.4 Resampling Technique

To compare sample measurements (such as wind speed, stability, etc.) from mostly stratiform, embedded, and mostly convective 3-hour periods, a two-sample permutation test is performed (section 5.3.3 of Wilks, 2006). The null hypothesis is that the two empirical samples are drawn from the same distribution. The test statistic is informative about the distribution of values, such as the difference between median or mean values of the two distributions (or other percentile differences, as shown later in the results). To conduct this test, the test statistic is calculated for the two empirical sample distributions (for example, samples from mostly convective and mostly stratiform 3-hour periods). Then the original two samples of measurements are pooled together. A null distribution of the test statistic is generated by calculating the test statistic on two pseudo-distributions (equal in size to the original two empirical distributions) n times. The two pseudo-distributions are generated by randomly drawing from the pooled distribution over a large number of trials (such as 10,000). The p-value for this test is calculated by dividing the number of times the null distribution of the test statistic is larger than the original test statistic by total number of trials. With this p-value, the hypothesis can be rejected or not rejected depending on the confidence level required (alpha-level). For this research, an alpha-level of 95% is required for rejecting the null hypothesis. A rejection of the null hypothesis means the odds of getting a difference as large as what was observed through randomly sampling are acceptably small.

3.5 Chapter Tables

Table. 3.1. Instrument Metadata.

Instrument Name	Type of Instrument	Variable Used	Location	Period Available	Time Interval
KRTX NWS WSR-88D	Scanning S-Band Precipitation Radar	Reflectivity (dBZ)	45.71 N 122.96 W	2002-2008	6-10 min
KSLE NWS Sounding	Upper-Air Balloon	Temperature, Dewpoint Temperature, Wind Speed and Direction	44.92 N 123.02 W	2002-2008	12 hr (00Z and 12Z)
KPDX NWS METAR	Surface Meteorological Observation	24 Hour Precipitation Total	45.59 N 122.60 W	2002-2008	Varies (at least 1 hr)
MRR	Vertically Pointing K-band Radar	Reflectivity (dBZ) Doppler Vertical Velocity (ms^{-1})	45.56 N 122.53 W	2005-2008	1 min when available
Fanno Creek Streamflow Gage	Stream Gage	Streamflow discharge (m^3s^{-1})	45.49 N 122.73 W	2002-2008	15 min
NLDN	Cloud-to-Ground Lightning Detection	Cloud-to-Ground Strike	300 km radius around KRTX	2002-2008	Each Strike

Table. 3.2. Rubric to interpret 3-hour period radar intermittency characteristics.

Local Grid Point Measure	**0 %**	**50 %**	**100 %**
Frequency of Precipitation	No Precipitation	Precipitating for half of the period	Always Precipitating
Frequency of Convective Precipitation*	Stratiform precipitation only	If precipitating, half of the time stratiform, half of the time convective	Convective precipitation only
Convective-Stratiform Intermittency*	No transitions between precipitation type (always convective or always stratiform)	Transitions occur half of the time precipitation occurs	Many transitions between precipitation type (nearly constant changes in categories)

* Conditional on precipitation occurring.

3.6 Chapter Figures

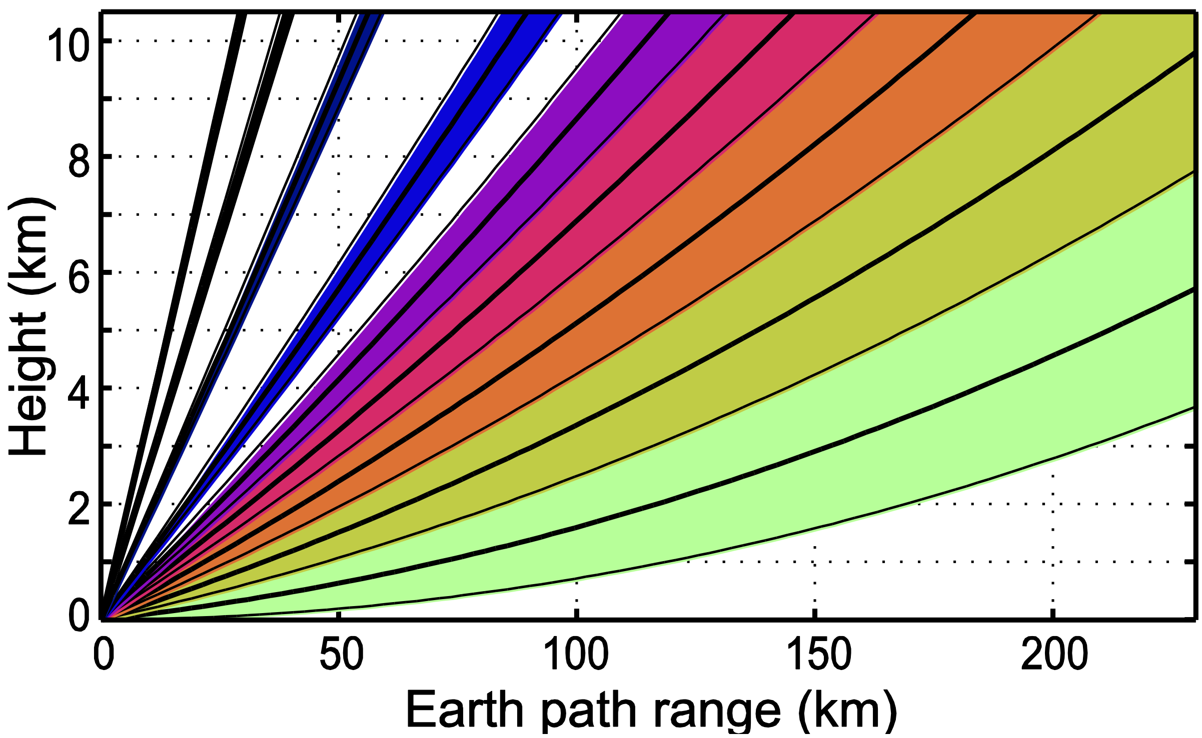

FIG. 3.1. NWS Volume Coverage Pattern 21, which scans 360 degrees at 9 elevation angles (0.5, 1.5, 2.4, 3.4, 4.3, 6.0, 9.9, 14.6, and 19.5 degrees) every 6 minutes. The NWS WSR-88D has an approximately 1.0 degree beamwidth at the half-power point.

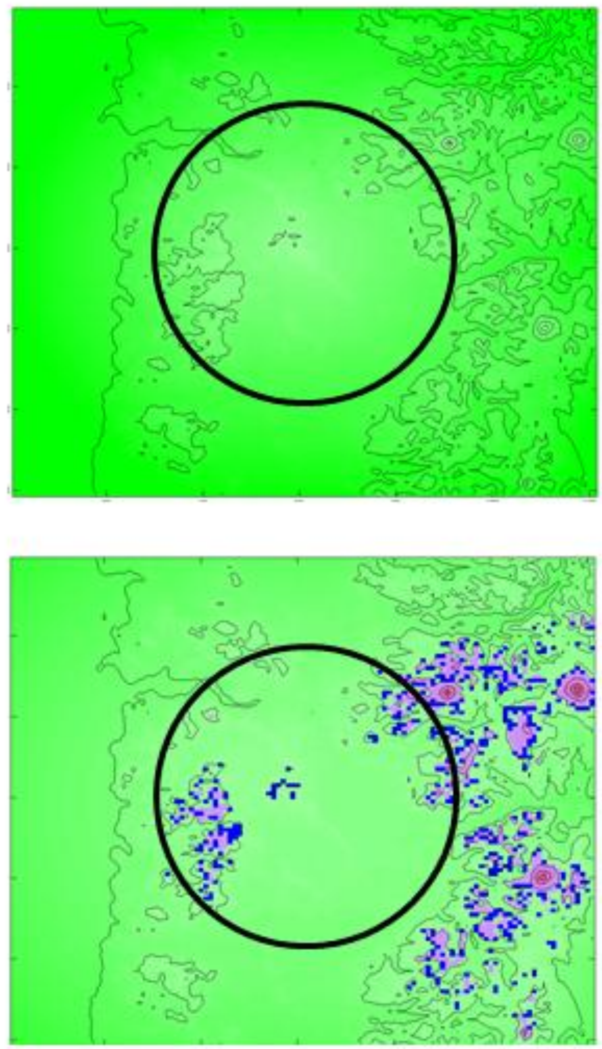

FIG. 3.2. Locations of partial beam filling for the 0.5 degree elevation slice for refraction in a standard atmosphere. Top figure) beam center of slice, bottom figure) lower edge of beam. Red colors indicate where a portion of the beam is below the Earth's surface, whereas green colors indicate that the beam is above the Earth's surface. Calculations are based on ray path equations in Doviak and Zrnik (1993). The black solid circle is the 70 km range ring.

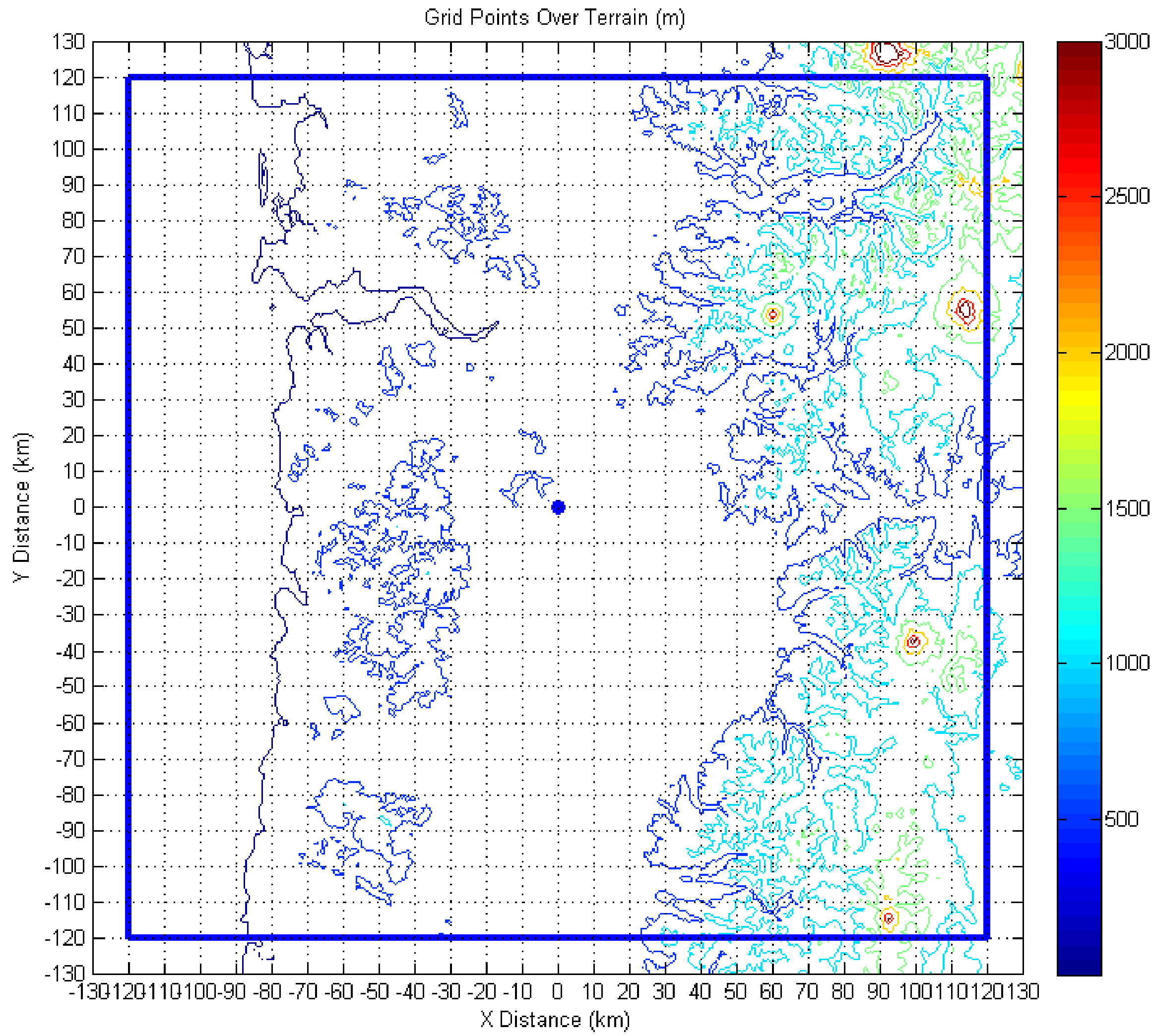

FIG. 3.3. Geographic Location of grid points for KRTX NETCDF files processed using NCAR Reorder. Terrain elevation is indicated with colored contours in meters. The dark blue lines represent the bounds of the file domain.

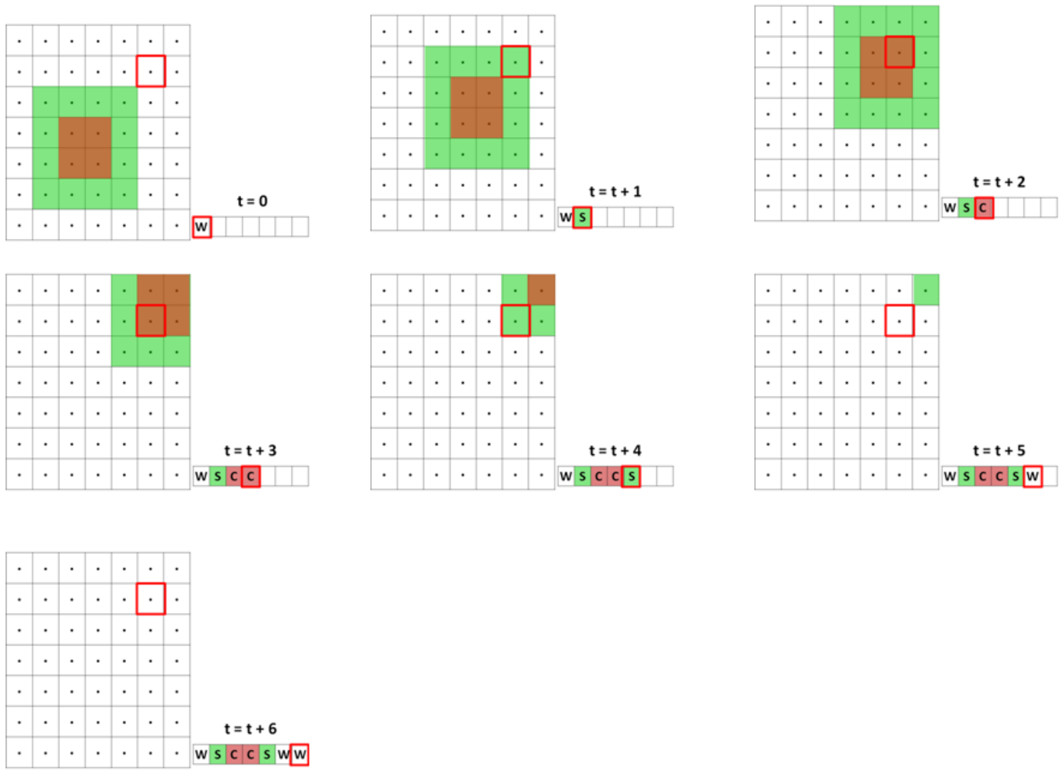

FIG. 3.4. Conceptual representation of how the CONVSF algorithm output might change in time for pixels. The red color indicates the pixel was identified as convective precipitation, the green color indicates that the pixel was identified as stratiform precipitation. The white color indicates that the pixel was identified as weak echo or no echo. The red box is a fixed location. The grid in the bottom right of each smaller figure shows how changes in CONVSF output change in time.

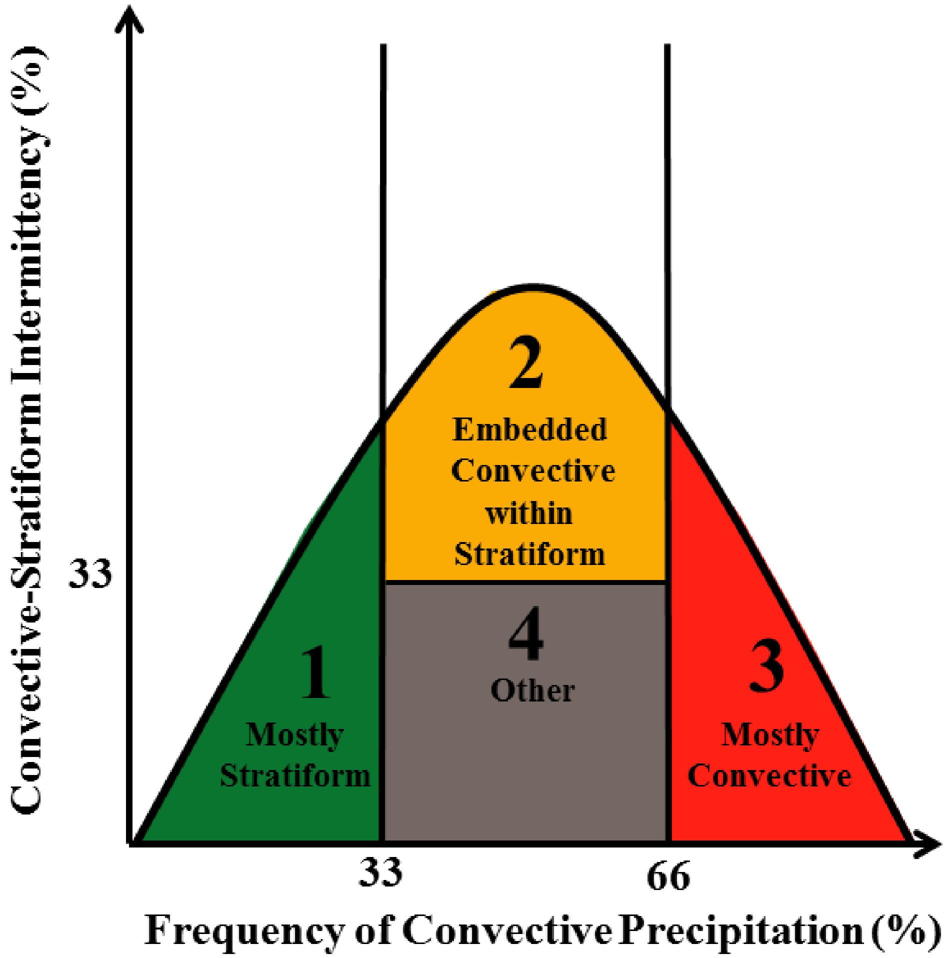

FIG. 3.5. The mapping of convective-stratiform intermittency and frequency of convective precipitation.

FIG. 3.6. Examples of KRTX radar reflectivity with corresponding convective-stratiform algorithm output. Panels a)-d) are KRTX radar reflectivity. Panels e)-h) are convective-stratiform algorithm output. Pixels are designated convective (red), stratiform (green), and weak echo or no echo (white). Panels i)-l) are data density diagrams of the of frequency convective precipitation versus convective-stratiform intermittency. Panel times: a), e), and i) correspond to a mostly stratiform period centered on 12 UTC 27 December 2005, b) , f), and j) correspond to an embedded convective within stratiform period centered on 06 UTC December 2005, c), g), and k) correspond to an "other" period centered on 21 UTC 31 December 2005, d) h), and l) correspond to a mostly convective period centered on 03 UTC 01 January 2006.

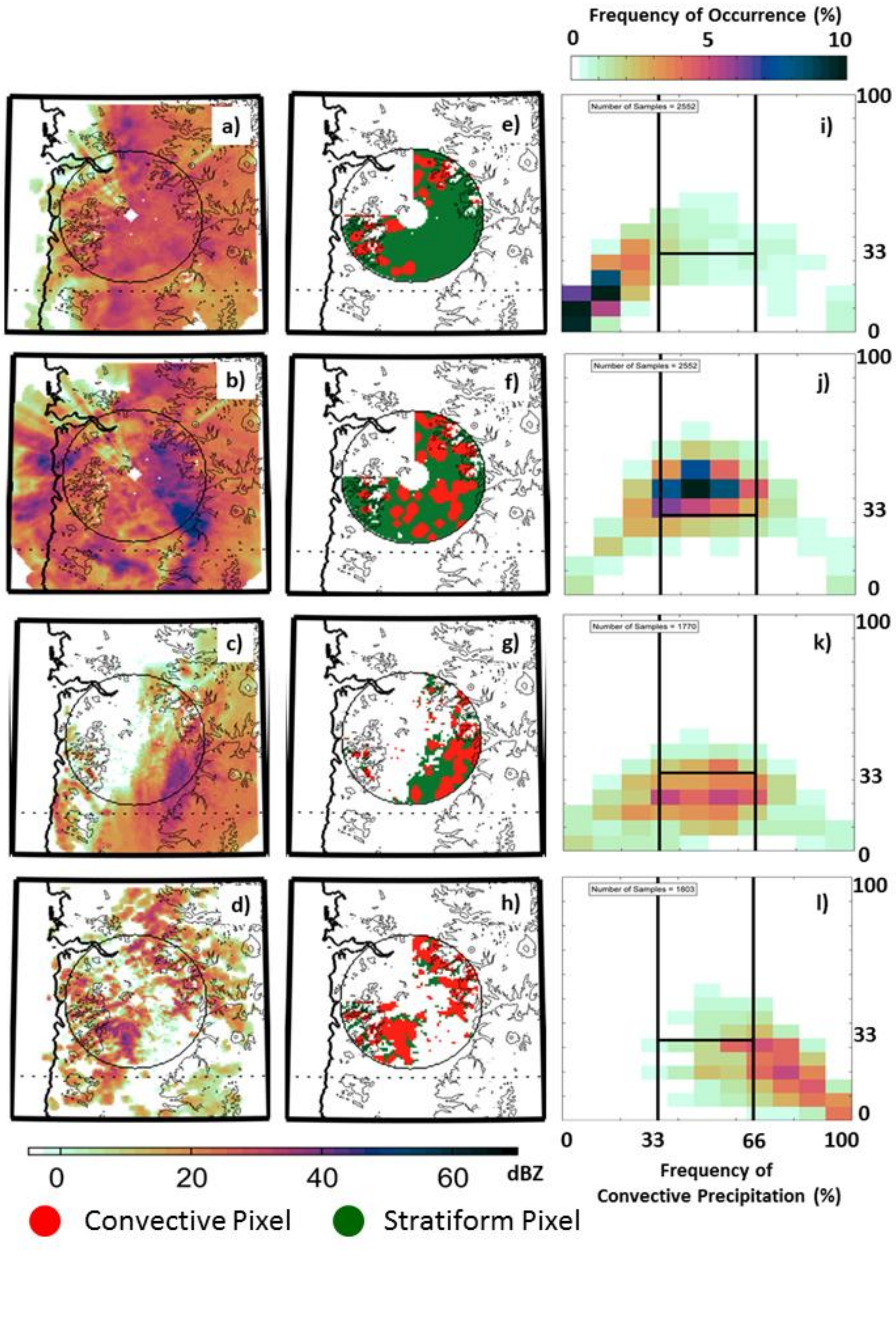

Frequency of Occurrence (%)
0
5
10
a)
b)
c)
d)
e)
f)
g)
h)
i)
j)
k)
l)
Number of Samples = 2552
Number of Samples = 2552
Number of Samples = 1770
Number of Samples = 1803
100
33
0
Convective-Stratiform Intermittency (%)
0
33
66
100
Frequency of Convective Precipitation (%)
0
20
40
60
dBZ
Convective Pixel
Stratiform Pixel

Chapter 4 – Application of Methodology to Case Studies

Three extratropical storm events near Portland, Oregon are highlighted in detail to illustrate the typical evolution of precipitation structures within passing winter cyclones. As will become obvious with the following cases, the synoptic pattern is strongly connected to the precipitation structure. Associated with synoptic changes are changes in hydrostatic instability. Previous work developed several conceptual models to explain characteristics of extratropical cyclones and the precipitation associated with them. Here, attention is paid specifically to those features easily identified with GOES IR, horizontal scanning radar algorithms, and vertically pointing radar. The scanning radar domain is much larger than that of the 1D vertically pointing radar and the vertically pointing radar time resolution is much higher than the scanning radar, so exact matching of features is not possible. However, together the instruments complement one another.

The typical extratropical cyclone transitions presented for 14 to 15 December 2006 and 02 to 04 December 2007 are contrasted with a more stable stratiform extratropical cyclone passage on 26 to 29 March 2005. Figure 4.1 illustrates the location of the surface cold front and the surface low pressure center for each storm with representative surface analyses. Each storm event differs in the details, but all storm events have identified surface cold fronts approaching the Pacific Northwest. Figure 4.2 indicates that each storm event has an upper-level trough axis approaching the study region. Figure 4.3a-d are representative soundings from each storm event. Figure 4.3a has an elevated conditionally unstable layer between approximately 530 mb and 600 mb, while figures 4.3b-c are conditionally stable throughout most of the vertical column. Figure 4.3d represents the mostly convective time period of the storm event on 14-15 December 2006, when the low levels of the troposphere are conditionally unstable. The following are more detailed descriptions of storm evolution with respect to precipitation intermittency and hydrostatic instability.

4.1 - 14 to 15 December 2006

The storm event 14 to 15 December 2006 occurred over a period of about 2 days. At 1145 UTC 14 December 2006, GOES IR indicated upper-level clouds over the KRTX domain (Fig. 4.4.a). These clouds (the "baroclinic leaf") were associated with the warm conveyor belt (Browning, 1990), located near the warm sector of the extratropical cyclone (Fig. 1.3). The warm conveyor belt is also the location of where the atmospheric river occurs (Zhu and Newell, 1998; Fig. 1.10 and 1.11). By 2345 UTC, the western edge of the upper-level clouds moved to the Oregon Coast and low-level cellular looking clouds became apparent over the eastern Pacific Ocean (Fig 4.4.c). By 0545 UTC 15 December, the low cellular clouds moved inland over Oregon (Fig. 4.4.d), indicating that the upper-level trough axis moved ashore.

At the MRR, precipitation began falling around 06 UTC (Fig. 4.5a). Intermittent precipitation algorithms applied to KRTX data identified the initial precipitation as mostly stratiform (Fig 4.5.b). By 12 UTC, KRTX domain precipitation is identified mostly as embedded convective within stratiform. Precipitation temporarily changed back to stratiform from 1630 UTC to 1930 UTC and then remained embedded for 9 more hours. MRR reflectivity data indicates warm frontal passage occurring between 06 UTC to 18 UTC (as evidenced by the increasing rain layer depth in the MRR time series). The rain layer depth began to decrease as the 0° C level decreased. Precipitation became mostly convective by 03 UTC 15 December. According to the MRR, convective precipitation continued until 00 UTC 16 December. Due to potential bright band contamination, the intermittent precipitation algorithms did not characterize the time period after 0730 UTC 15 December; however, the isolated cellular echoes and clouds indicated by MRR reflectivity and GOES IR during this period suggest the period should be categorized as mostly convective precipitation.

The time-height profiles of stability measures reveal conditional instability (Fig 4.5d) and most unstable parcel buoyancy (Fig 4.5c) aloft (4.5 to 5.5 km) during the stratiform and embedded 3-hour periods ultimately transitioning to a surface-based conditional instability and buoyancy by the mostly convective precipitation 3-hour periods. The most unstable parcel (indicated by blue circles in figure 4.5c) originated at 3 km during the stratiform and embedded 3-hour periods of the storm, but decreased in height by the mostly convective periods. Both conditional instability and potential instability, as related by $\frac{d\bar{\theta}_{es}}{dz}$ and $\frac{d\bar{\theta}_{e}}{dz}$, respectively, are present at 4.5 to 5.5 km altitude from 12 UTC 14 December to 00 UTC 16 December (Fig. 4.5d-e). The vertical column of air has a relatively deep layer of most unstable parcel buoyancy at 00 UTC 16 December, which is near the end of the mostly convective precipitation period (indicated by the bright orange colors in Fig 4.5.c). This period relates to the cold sector of the surface cyclone or the western-side of the upper-level trough axis. Surface layer conditional and potential instability appear at 00 UTC 15 December and 00 UTC 16 December. In terms of Kelvin-Helmholtz instability (Fig. 4.5f), the Richardson number was ideal (i.e. $0 < \mathrm{Ri} < 0.25$) only sporadically and did not appear to be strongly related to evolution of precipitation structure.

Figure 4.6 illustrates three separate MRR reflectivity time series for 3-hour periods corresponding to a mostly stratiform (panel a - 06 UTC 14 December), embedded convective within stratiform (panel b - 18 UTC 14 December), and a mostly convective (panel c - 06 UTC 15 December). Fallstreaks form as a result of buoyant convective overturning, shear driven turbulence, or convective overturning in the melting layer (Marshall, 1953; Gunn et al., 1954; Yuter and Houze, 2003). Fallstreaks in the snow layer are present in all three of the MRR time series images, but are most obvious in the embedded 3-hour period. The fallstreaks within the snow layer of the mostly stratiform period (Fig. 4.3.a) are more diffuse than the other two 3-hour periods. During the stratiform and embedded cases, the fallstreaks appear to originate from altitudes above range of the MRR. Many of the fallstreaks in the rain layer for all three cases appear to be an extension of fallstreaks in snow. Some of the fallstreaks in the embedded and mostly convective period appear to originate just above the melting layer or in the rain layer.

4.2 - 02 to 04 December 2007

The 2-4 December 2007 storm event occurred over a period of about 3 days. Similar to 14-15 December 2006, GOES IR (Fig 4.7) indicates a typical cyclone passage over the Portland, Oregon region during this period. Warm frontal passage occurs between 12 UTC 02 December and 12 UTC 03 December (as indicated by MRR data showing deepening of the rain layer shown in Fig 4.8a). At 0645 UTC 03 December, the baroclinic leaf had already moved ashore (Fig 4.7a). By 1915 UTC (Fig. 4.7c), GOES IR indicates the upper-level trough axis had moved a couple of hundred kilometers to the east of its location at 1145 UTC. The upper-level clouds associated with the warm conveyor belt are aligned from the southwest to the northeast bringing a southwesterly moist flow from the Pacific Ocean into the Pacific Northwest region. The western edge of the upper-level clouds associated with the warm conveyor belt moved past the Portland, Oregon region by 0515 UTC 04 December (Fig 4.7e). After 0515 UTC, GOES IR indicates isolated low-level clouds similar to what was observed after cold frontal passage in the 14-15 December 2006 storm.

MRR data indicates convective or cellular type precipitation occurring on 02 December from 00 UTC to approximately 12 UTC (Fig 4.8a). This early period of precipitation is not categorized by the intermittency identification algorithms due to the low 0° C level and possible bright band contamination in KRTX reflectivity data. At 21 UTC 02 December, the algorithms detect embedded convection (Fig 4.8b). By 00 UTC 03 December precipitation becomes strongly stratiform for about 24 hours. At 00 UTC 04 December, the precipitation briefly becomes embedded transitioning into mostly convective by 03 UTC.

The vertical stability profiles (Fig. 4.8c-d), indicate elevated conditional instability and most unstable parcel buoyancy (approximately 3.5 to 4.5 km altitude) from about 00 UTC 02 December to 00 UTC 03 December. During this time there is also a region of strong potential instability at around 2 km altitude. All stability measures begin to indicate more frequent occurrence of most unstable parcel buoyancy and occurrence of conditional instability throughout the vertical column beginning at 00 UTC 04 December. By 12 UTC substantial conditional instability and most unstable parcel buoyancy is present from surface to about 4 km. The most unstable parcel originated from above 2 km for the embedded and mostly stratiform periods, but was near the surface for the mostly convective periods (Fig. 4.8c). Vertical wind shear instability occurs sporadically and is more frequently for the 02-04 December 2007 case than for the 14-16 December 2006 case.

Figure 4.9 illustrates three separate MRR reflectivity time series for 3-hour periods corresponding to a mostly stratiform (panel a - 00 UTC 03 December 2007), embedded convective within stratiform (panel b - 00 UTC 4 December), and a mostly convective (panel c - 09 UTC 04 December). Here, as in the 14-15 December 2006 storm, fallstreaks in snow are present in all three cases. The rain layer appears to be enhanced directly beneath the fallstreaks in snow. As in Fig. 4.6, the fallstreaks in the in snow layer of the stratiform 3-hour period (Fig. 4.9.a) are more diffuse than those in the convective or embedded periods. The source of the fallstreaks for the stratiform and embedded 3-hour periods appears to originating from above 2 km and in some periods above the MRR range of 4.5 km.

4.3 - 26 to 29 March 2005

A storm with very different hydrostatic stability profiles occurred on 26 to 29 March 2005. The intermittent precipitation identification algorithms categorize almost the entire storm (09 UTC 26 March to 21 UTC 28 March) as mostly stratiform (Fig. 4.10b). Hydrostatic stability measures show a more stable atmosphere both aloft and at the surface for the 12 UTC 26 March and 12 UTC 27 March soundings. What conditional instability aloft that does exist is relatively weak (00 UTC on 27 March). Most of the conditional instability is near the surface from 00 UTC 28 March to 00 UTC 29 March. Precipitation becomes mostly convective by 03 UTC 28 March (Fig. 4.10b). Again, for this case vertical wind shear instability tends to occur relatively sporadically throughout the storm event. Vertically pointing radar data were not available during this period, so observations of fallstreaks in snow were not possible.

4.4 Summary of Cases

14-15 December 2006 and 2-4 December 2007 storms record the evolution of precipitation structure and hydrostatic instability and Kelvin-Helmholtz instability of two separate extratropical cyclones. A common theme among the two separate cases, is the presence of conditional or potential instability aloft (2 to 6 km altitude) during the initial stages of the cyclone passage (near the warm front and warm sector) followed by the transition to surface based conditional instability at the time of near cold frontal passage. According to parcel theory, much of the conditional instability is realized when the theoretical most unstable parcel is lifted. Elevated buoyancy exists during the early periods of the storm events. By the mostly convective periods, the buoyancy is near the surface. Observations of potential instability aloft within extratropical cyclones are consistent with past observations and conceptual models from the past 30 years (Browning, et al., 1974; Browning, 1990; Woods et al. 2005, Ralph et al., 2011) (Fig. 1.13 and Fig. 1.14). Employing the ingredients based method for assessing an environment for convective potential (McNulty, 1978; Doswell, 1987; Schultz and Schumacher 1999) reveals that the storm environments in 14-15 December 2006 and 2-4 December 2007 are capable of producing overturning motions due to buoyant convection. Buoyant convection is present to a lesser extent 26-29 March 2005. Convection occurs primarily aloft for the stratiform and embedded periods, but is surface based in the mostly convective 3-hour periods. A relationship between vertical wind shear instability (according to the Richardson number) and precipitation intermittency is less clear.

Snow fallstreaks appear to be related to the instability aloft. The nearly ubiquitous nature of fallstreaks in snow shown in MRR reflectivity for stratiform, embedded convective within stratiform, and mostly convective periods is consistent with the location of the hydrostatic instability. The fallstreaks in snow enhance the precipitation in the rain layer immediately beneath the fallstreaks, thus increasing the intermittent nature of precipitation near the surface (i.e. the seeder/feeder mechanism). Increased precipitation intermittency in the surface rain layer seems to be different than the Houze (1993) seeder/feeder conceptual model that indicates precipitation should be more continuous in the feeder region of the cloud (Houze’s Figs. 6.6 and 6.7).

4.5 Chapter Figures

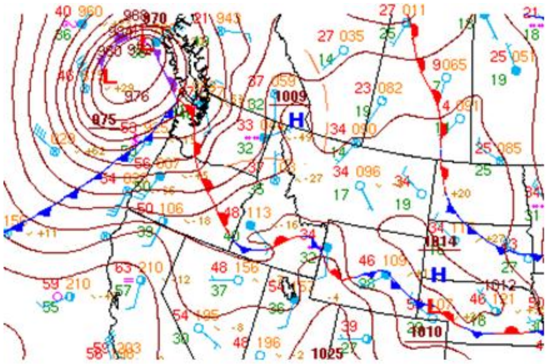

a) 00 UTC 15 December 2006

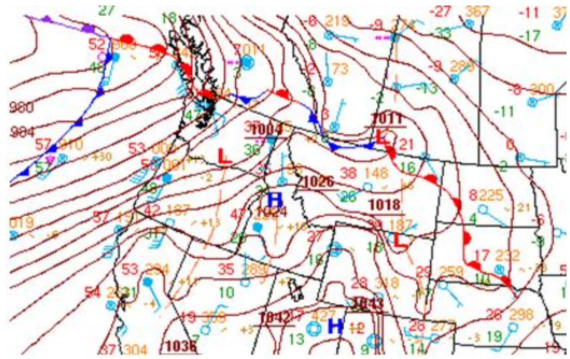

b) 12 UTC 03 December 2007

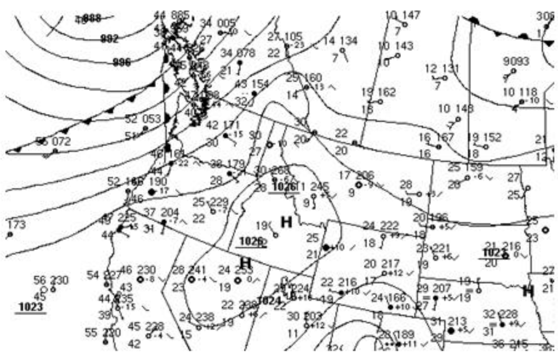

c) 12 UTC 26 March 2005

FIG. 4.1. Hydrometeorological Prediction Center surface analyses. Panel a) 00 UTC 15 December 2006, panel b) 12 UTC 03 December 2007, and panel c) 12 UTC 26 March 2005.

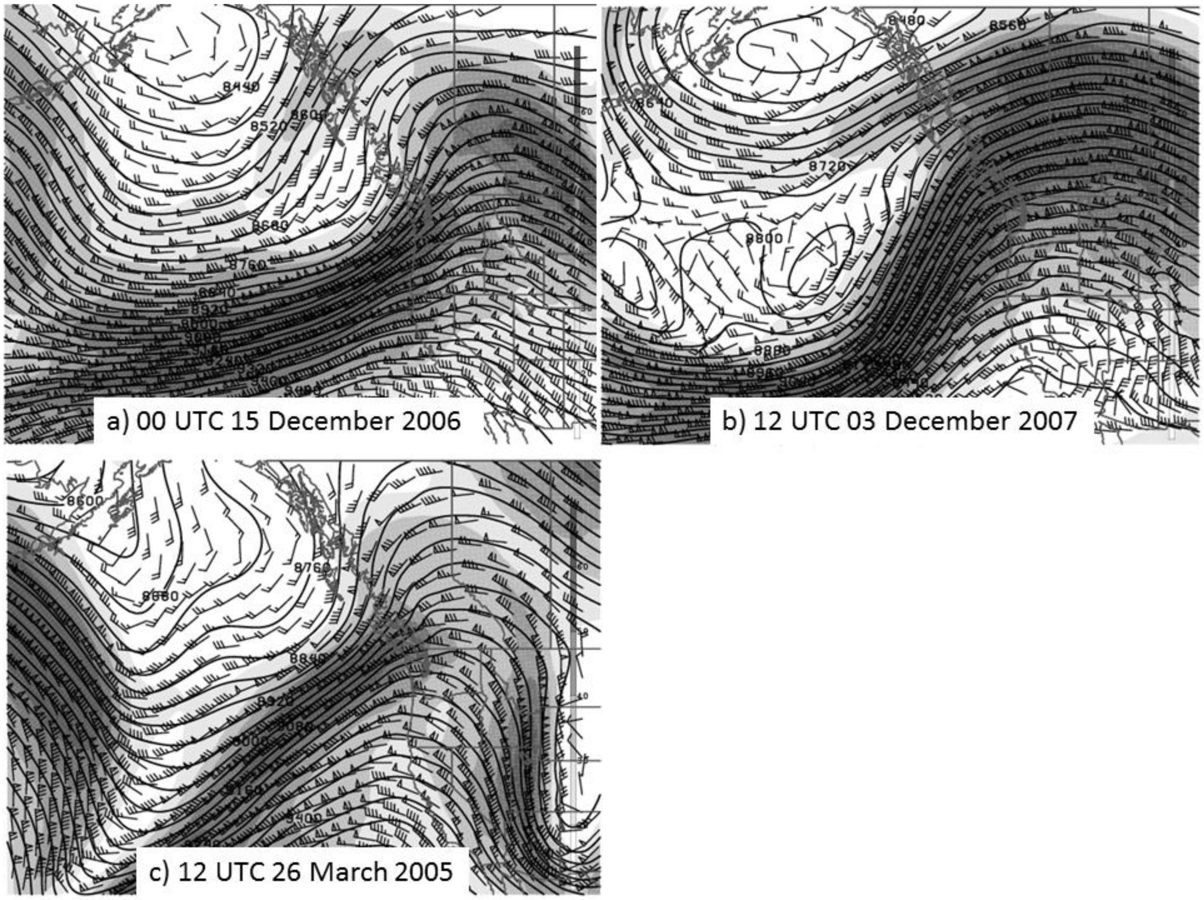

FIG. 4.2. North American Regional Reanalysis 300 mb plots. Panel a) 00 UTC 15 December 2006, panel b) 12 UTC 03 December 2007, and panel c) 12 UTC 26 March 2005. Black solid lines are constant geopotential height and shading is wind speed (lightest shading is 30 m s^{-1}, while the darkest shading indicates 60 m s^{-1}). (Images were provided by Sara Ganetis of Stony Brook University).

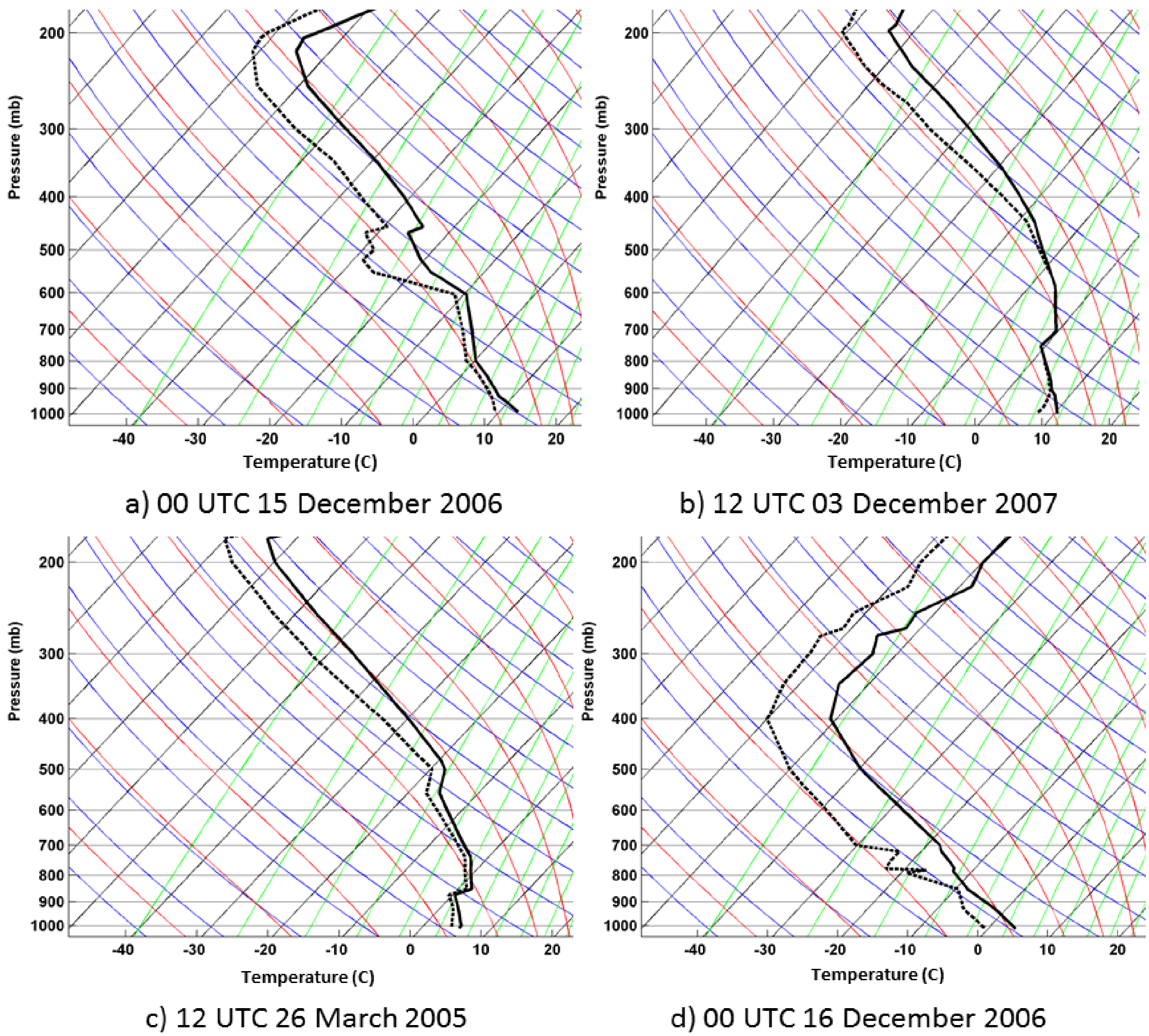

FIG. 4.3. Salem, Oregon (KSLE) SkewT-LogP diagrams. Panel a) 00 UTC 15 December 2006, panel b) 12 UTC 03 December 2007, panel c) 12 UTC 26 March 2005 and panel d) 00 UTC 16 December 2006. Non-labeled figure features: green solid lines are water vapor mixing ratio (g kg^{-1}), blue solid lines are dry adiabats (° C), and red solid lines are moist (saturation) adiabats (° C).

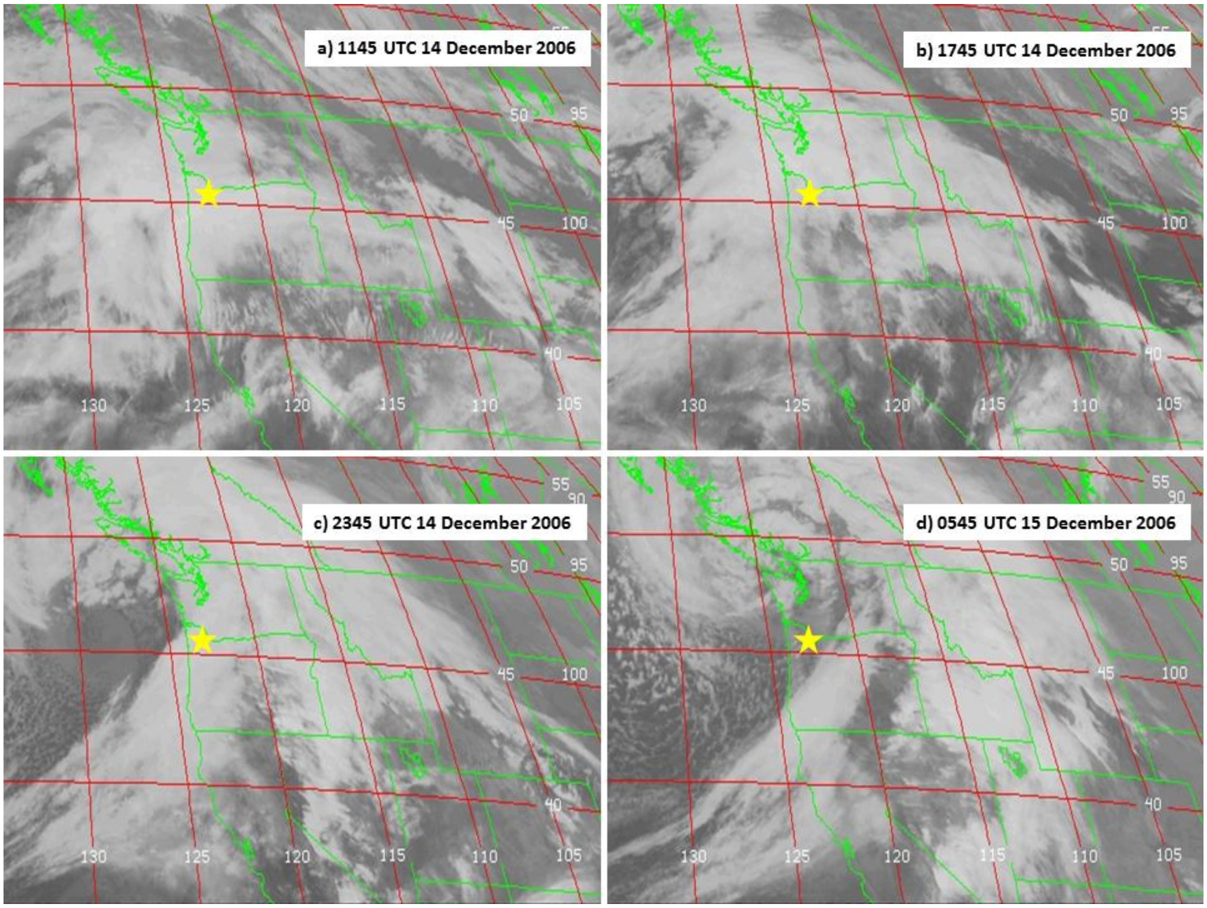

FIG. 4.4 – GOES IR for 14 to 15 December 2006 a) 1145 UTC 14 December 2006, b) 1745 UTC 14 December 2006, c) 2345 UTC 14 December 2006, d) 0545 UTC 15 December 2006. The star represents the center of the study domain (Portland, Oregon).

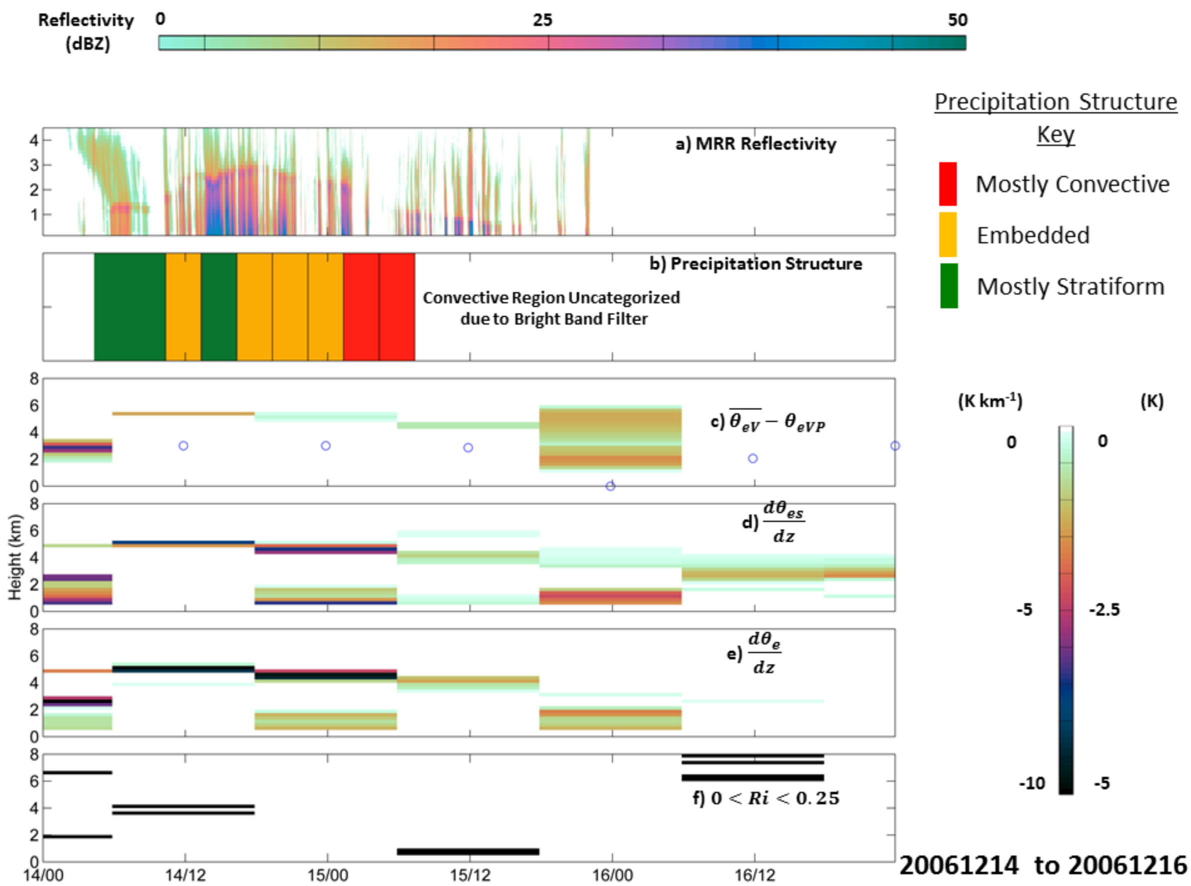

FIG. 4.5. Time series data for 14 to 15 December 2006. a) MRR Reflectivity, b) Precipitation Structure (green = mostly stratiform, gold = embedded, red = mostly convective), c) $\overline{\theta_{eV}} - \theta_{eVP}$ (a measure of buoyancy) in units K, decreasing values indicate more buoyancy, d) $\frac{d\bar{\theta}_{es}}{dz}$ (a measure of conditional instability) in units K km^{-1}, e) $\frac{d\bar{\theta}_{e}}{dz}$ (a measure of potential instability) in units K km^{-1}, and f) $0 < \mathrm{Ri} < 0.25$ (a measure of vertical wind shear instability (yes = black, white = no). Blue circles in panel c) are origination altitudes of the most unstable parcel (below 3 km) used for calculating $\overline{\theta_{eV}} - \theta_{eVP}$.

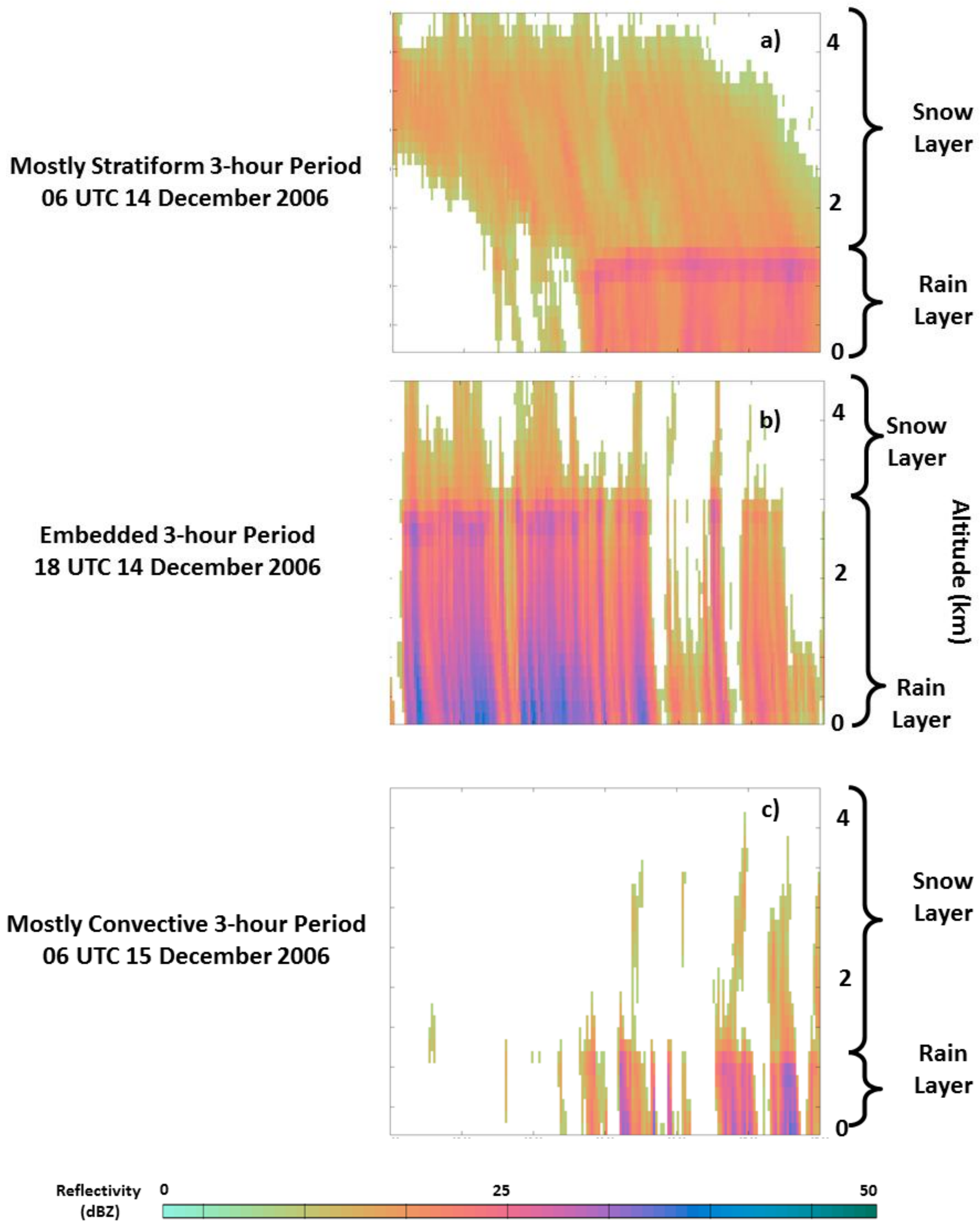

FIG. 4.6 – MRR 3-hour periods for 14 to 15 December 2006. a) mostly stratiform 3-hour period (06 UTC 14 December 2006), b) embedded 3-hour period (18 UTC 14 December 2006), c) mostly convective 3-hour period (06 UTC 15 December 2006)

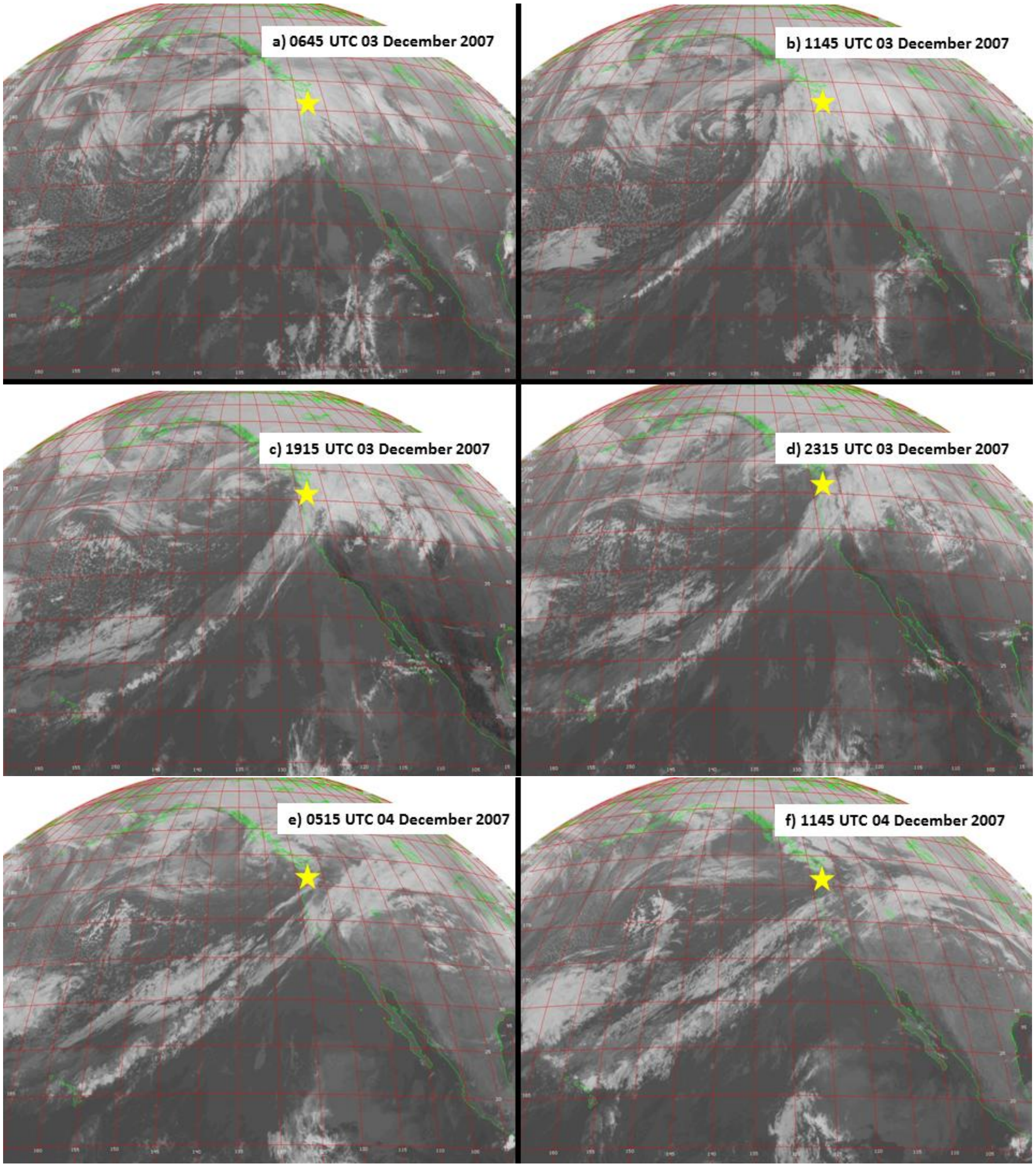

FIG. 4.7 – GOES IR for 02 to 04 December 2007. a) 0645 UTC 03 December 2007, b) 1145 UTC 03 December 2007, c) 1915 UTC 03 December 2007, d) 2315 UTC 03 December 2007, e) 0515 UTC 04 December 2007, f) 1145 UTC 04 December 2007. The star represents the center of the study domain (Portland, Oregon).

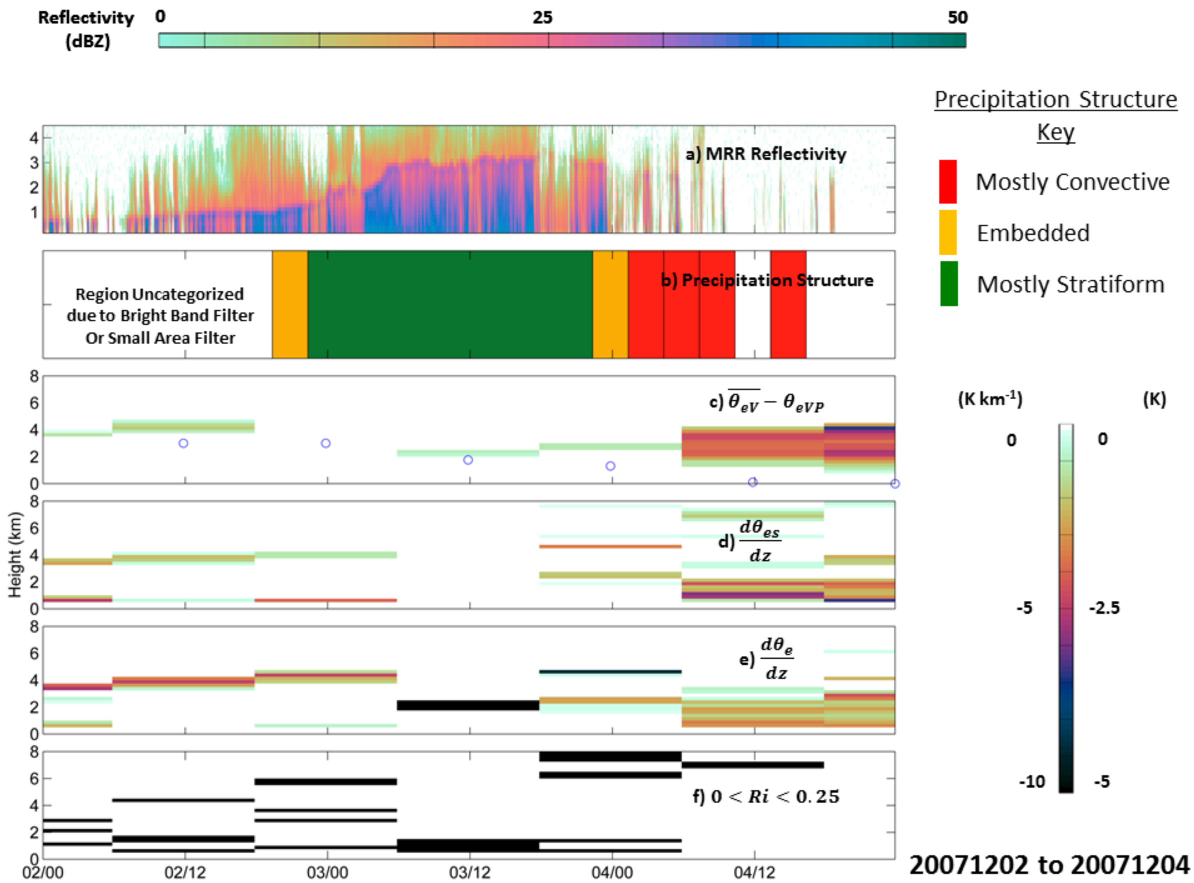

FIG. 4.8. Time series data for 02 to 04 December 2007. As in Fig 4.5.

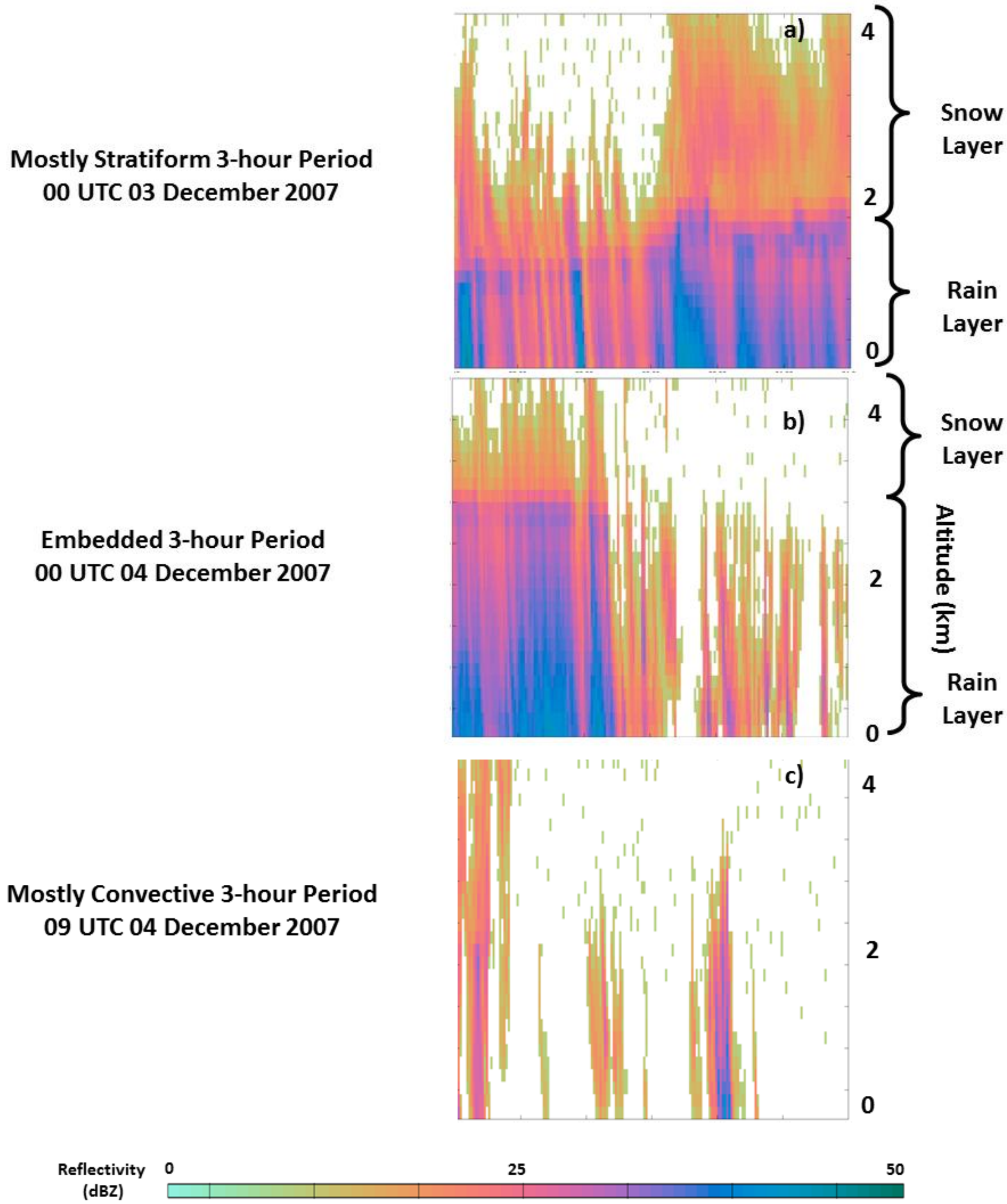

FIG. 4.9 – MRR 3-hour periods for 02 to 04 December 2007. a) Mostly stratiform 3-hour period (00 UTC 03 December 2007), embedded 3-hour period (00 UTC 04 December 2007), mostly convective 3-hour period (09 UTC 04 December 2007).

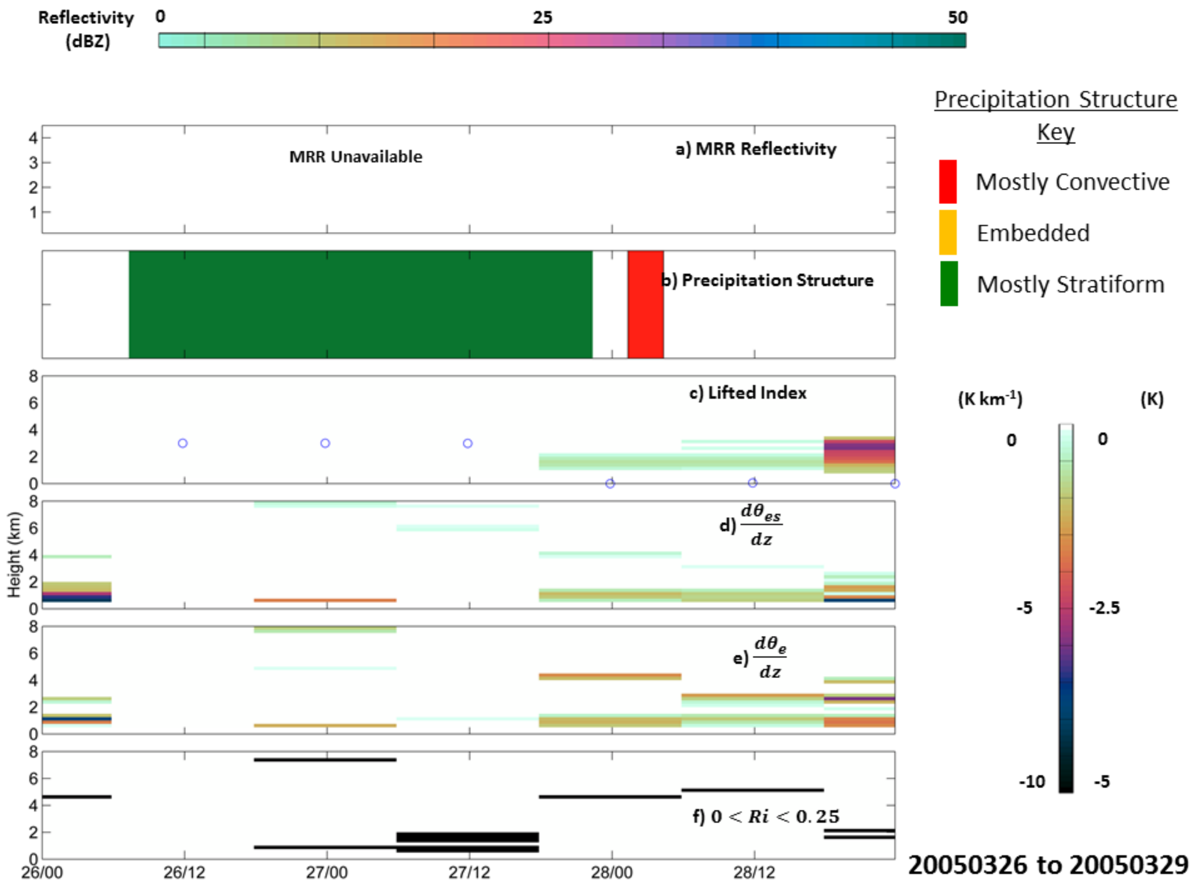

FIG. 4.10. Time series data for 26 March 2005 to 29 March 2005. As in Fig. 4.5.

Chapter 5 – Atmospheric characteristics of cool season intermittent precipitation near Portland, Oregon: 2002-2008

5.1 Annual Cool Season Characteristics

From 2002 to 2008, 641 3-hour periods[7] were categorized with the two-step intermittent precipitation identification process (Appendix E). Sixty percent of the 3-hour periods were categorized as mostly stratiform, 20% as embedded convective within stratiform precipitation, and 15% as mostly convective precipitation (Table 5.1 and Fig. 5.1). The unclassified "other" mode represented only 5% of the 3-hour periods. The number of 3-hour periods per cool season varied from a minimum of 56 periods in 2004-05 to a maximum of 142 periods in 2006-07. The total number of 3-hour periods closely correlates with the number of days with a NCDC flood report in either Washington or Oregon (Fig. 5.1) [NCDC 2012].

The mostly stratiform precipitation mode was the most common of the four precipitation modes during all six years (Figs. 5.1 and 5.2). For every year, except for 2007-08, mostly stratiform precipitation occurred in over 50% of the 3-hour periods categorized. The increase in 3-hour periods in the last 3 years was accompanied by an increase in the number and fraction of intermittent precipitation 3-hour periods. The highest number of intermittent precipitation 3-hour periods (62) occurred during 2006-07. For both Washington and Oregon, the number of individual federal disaster declarations related to flooding, mudslides, and landslides was highest in 2006-2007 (FEMA, 2012). High rain rate and long duration of rainfall are among known factors that contribute to increased landslide potential and river flooding (Baum and Godt, 2010; Yuter et al. 2011).

[7] Equivalent to approximately 80 days' worth of significant precipitation

5.2 Storm-Scale (Synoptic) Characteristics

5.2.1 GOES Satellite Analysis

GOES IR imagery from Chapter 4 illustrated the relationship of synoptic structure-to-mesoscale precipitation structure for a few storm events. This section distills information from GOES-IR imagery during storm events for 4 cold seasons (years 2002-03, 2003-04, 2004-05, and 2005-06). In order to conduct this analysis, GOES IR images of the Pacific Northwest region were manually examined to determine the location of the study domain relative to features of the extratropical cyclone that are discernible from IR imagery following Bader et al. (1995). The location of the 240 km by 240 km study domain was categorized as either 1) *ahead of cloud shield* (no upper-level cloud above the domain) 2) *beneath cloud shield* (upper-level cloud above the domain, corresponding to the warm conveyer belt region near the warm sector), 3) *near surface cold front* (in the warm sector within approximately 100 km to the east of the western edge of the mid-to-upper-level cloud), 4) *cold sector* (mostly low-level cellular clouds, free of upper-level clouds), or 5) *other*. No attempt was made to distinguish cold frontal type, so the cold front could be oriented with a "traditional" tipped back cold front or with a forward tipped split-front (Fig. 1.12). Also, no attempt was made to precisely locate the warm front.

Overall, the locations of mesoscale precipitation structures relative to synoptic features were found to be consistent with conceptual models from Nagle and Serebreny (1962), Hobbs (1978), and Medina et al. (2007) (Fig 1.7 and Fig 1.8). Mostly stratiform precipitation 3-hour periods occurred most frequently (50%) while beneath the cloud shield region (Fig. 5.3). Embedded convective within stratiform precipitation occurred most frequently (40%) near the surface cold front region (Fig. 5.3). Mostly convective precipitation 3-hour periods occurred most frequently (> 50 %) in the cold sector region (Fig. 5.3). Excluding the other category, the typical progression of features was in numerical order from 1) to 4). However, the order and duration of extratropical cyclone features did vary.

5.2.2 KSLE Sounding Variables

Vertical profiles of wind direction, wind speed, and relative humidity, as well as height of the 0° C level from the KSLE soundings confirm the GOES IR satellite analysis results. To avoid double counting, only 3-hour periods corresponding to sounding release time were paired with sounding data. Since soundings were only available every 12 hours, oversampling of one storm was unlikely. In all, 99 soundings were used to describe mostly stratiform 3-hour periods, 40 soundings for embedded convective within stratiform, and 27 soundings for mostly convective. For a complete listing of soundings used for this analysis, see bold highlighted 3-hour periods in Appendix E.

KSLE soundings indicate that mostly stratiform 3-hour periods had a median 0° C level of 2.1 km, excluding 3-hour periods with a 0° C level below 1.4 km[8]. Embedded 3-hour periods and mostly convective 3-hour periods had 0° C levels of 1.8 km and 1.6 km, respectively (Fig. 5.4). The difference in medians for the stratiform and embedded periods was not statistically significant (using the test described in 3.4), but the difference in medians between mostly convective and mostly stratiform was statistically significant. The observed decrease in freezing level height from stratiform-to-embedded-to-convective is consistent with cold frontal passage and typical cyclone evolution over a fixed point in the mid-latitudes.

At 1 km altitude, the typical wind direction for mostly stratiform 3-hour periods and embedded convective 3-hour periods was from 180 to 225 degrees (Fig. 5.5). By 4 km altitude, the typical wind for both modes was from 200 to 250 degrees. Both modes have similar wind profiles, consistent with the satellite analysis in Section 5.2.1, which showed embedded and stratiform precipitation occurring within the warm sector. The mostly convective mode is typically accompanied by more westerly wind (from 200 to 250 degrees at 1 km and 225 to 275 at 4 km altitude) throughout the column. This is also consistent with the satellite analysis in Section 5.2.1, which showed mostly convective occurring primarily in the cold sector of extratropical cyclones.

[8] 3-hour periods removed to avoid bright band contamination.

Although there is very little wind direction difference between stratiform and embedded modes, there is a statistically and meteorologically significant difference between wind speeds for each mode. Embedded 3-hour periods show a 3-5 m s^{-1} higher absolute wind speed than stratiform 3-hour periods (Fig. 5.6). Calculations of vertical wind shear do not show a statistically significant difference between the stratiform and embedded convection modes. It is unclear whether the increase in total wind speed is due to increased convective activity or if the increased wind speed is related to a change in the mesoscale or synoptic environment leading to increased convective activity. The higher wind speeds could simply be due to a tighter pressure gradient near surface or upper cold front. Higher wind speeds could also increase the amount of orographic lifting (i.e. higher cross-barrier winds could lift potentially unstable layers causing destabilization).

Moisture profiles for stratiform and embedded precipitation indicate near saturated conditions from the surface to 3 km (relative humidity from 80% to over 90%; Fig. 5.7). Lower tropospheric moisture is a required ingredient for moist convection. Above 3 km the relative humidity decreases more rapidly for embedded convective than for stratiform precipitation. Mostly convective 3-hour periods are closely saturated from surface to approximately 2 km. Between 2 km and 5 km altitude, relative humidity decreases rapidly. By 5 km altitude, the typical relative humidity for isolated convection is between 20% and 50%. Dry air over moist air likely implies potential instability is present with the embedded and mostly convective periods.

5.2.3 Storm Temporal Patterns

Analysis of the duration of and order in which the different precipitation categories occurred during storm events indicated four main patterns. A storm event is defined as a period of at least 9 hours (three 3-hour periods) within a 24 hour period that is categorized by the two-step intermittent precipitation detection process. By virtue of the filtering involved, these events only include periods with 0° C level > 1.4 km, significant precipitation days at KPDX, and periods with persistent precipitation (frequency of precipitation > 30%) for at least 1000 km^2 of the KRTX domain. The most *typical* pattern was a transition from stratiform to intermittent precipitation (mostly convective and/or embedded convective within stratiform). A *stratiform* pattern occurred when stratiform precipitation was present for at least 9 hours with no more than one intermittent 3-hour period during the storm. An *intermittent* only storm pattern was intermittent for at least 9 hours. A *remainder* pattern is used to label all other transitions.

Table 5.2 reports the identified patterns by event and Figure 5.8 summarizes pattern types by year. Most years, the fraction of typical transitions to total storm events is around 50%, but 2004-05 experienced the lowest ratio with only 1 out of 7 events (14%) with a typical pattern. Stratiform patterns are the next most common pattern of precipitation. The fraction of stratiform patterns is largest during the first three years (43 to 57%). Remainder patterns occur most frequently during 2006-07 (occurring in 1 out of 4 events).

5.3 Mesoscale Characteristics

5.3.1 Hydrostatic Instability and Kelvin-Helmholtz Instability

To test the hypothesis described in Chapter 2, several parameters for hydrostatic instability were examined with data from the KSLE sounding (2002 to 2008). Fig. 5.9 illustrates the fraction of precipitation periods identified with 1) positive MUCAPE, 2) no MUCAPE, but potentially unstable, and 3) no MUCAPE and potentially stable for each type of precipitation structure (mostly stratiform, embedded convective within stratiform, and mostly convective). Here, a sounding is considered to have potential instability layers if there are at least two 500 meter layers with $\frac{d\bar{\theta}_e}{dz} < 0$ somewhere in the vertical column. Lifting a potentially unstable layer releases latent convective instability. Layer lifting occurs in Pacific Northwest cool season storms with frontal forcing and/or air flow over terrain (and will likely occur for a high percentage of potentially unstable layers).

Recall from Chapter 2 the testable hypothesis*: the frequency of precipitation periods with positive buoyancy (as measured by most unstable parcel convective available potential energy*[9]*) should be higher (> 2x) for embedded convective within stratiform precipitation*

[9] Convective available potential energy is defined in Chapter 3.

periods than for mostly stratiform precipitation periods. Based on analysis of the KSLE sounding data, the hypothesis is confirmed. Periods with embedded convective cells within stratiform precipitation have a frequency of MUCAPE > 0 J kg^{-1} about 2.8 times that of stratiform precipitation by itself (Fig 5.9a-b and 5.10). Forty-eight percent of embedded period soundings have MUCAPE > 0 J kg^{-1}, while only 17% of mostly stratiform period soundings have MUCAPE > 0 J kg^{-1} (Fig. 5.9). Of the embedded periods with zero J kg^{-1} MUCAPE, most are potentially unstable (Fig. 5.9a). Combining embedded periods with either MUCAPE > 0 J kg^{-1} or potential instability yields up to 90% of embedded periods with active or latent (potential) hydrostatic instability. Eighty-nine percent of convective period soundings have positive MUCAPE and the remaining are potentially unstable (Figs. 5.9c and 5.10b). The sounding analysis indicates that there is an increased frequency of hydrostatic instability (in terms of MUCAPE or potential instability) with increasing cellularity or precipitation intermittency (as indicated by the radar identified categorical precipitation modes).

The magnitude of available potential energy is commensurate with the precipitation structure. Surface parcel based CAPE calculations (SBCAPE) are ill-suited to quantify the total available energy (Fig 5.10a) when surface inversions are present. Instead, calculations of the most unstable parcel CAPE (MUCAPE) are more appropriate (Fig 5.10b). Figure 5.10b shows statistically significant different MUCAPE distributions for stratiform, embedded convective and mostly convective precipitation modes. The cumulative distribution curves in Figure 5.9b show that nearly 83% of stratiform precipitation 3-hour periods have 0.0 J kg^{-1} of MUCAPE, while the remaining 17% of 3-hour periods have more than 0 but less than 100 J kg^{-1} of MUCAPE. In contrast, 89% of the mostly convective 3-hour periods have more than 0.0, but less than 460 J kg^{-1} of MUCAPE. Forty-eight percent of the embedded convection 3-hour periods have more than 0.0, but less than 350 J kg^{-1} of MUCAPE. Presented another way, parcel theory predicts that mostly convective periods have enough MUCAPE present to produce convective updrafts (w_{max} > 2 ms^{-1}) in 89% of the 3-hour periods (Fig. 5.10b). In contrast, only 10% of stratiform precipitation periods have sufficient MUCAPE to produce convective updrafts. Embedded periods have enough

MUCAPE to produce convective updrafts in 48% of periods. The 75th percentile w_{max} for embedded precipitation periods is 4.5 ms^{-1} compared to 17.5 ms^{-1} for mostly convective periods. The MUCAPE and updraft velocities predicted by parcel theory are not high compared to deep moist convection standards. However, these magnitudes of instability appear to be sufficient for seeder cells.

Hydrostatic instability during embedded periods is elevated compared to mostly convective periods (Fig. 5.10c). The 50th percentile of the distributions of height of origin for most unstable parcels is 2.5 km for embedded periods versus 0.5 km in mostly convective periods. The distributions of most unstable parcel height of origin for convective and embedded precipitation are statistically different. This finding is relevant to the seeder-feeder mechanism, which requires an elevated unstable layer. Figure panels 5.11a-c are frequency by altitude diagrams of $\bar{\theta}_{eV} - \theta_{eV}$, based on the most unstable parcel, for stratiform, embedded convection, and isolated convection modes respectively. The vertical resolution is 0.5 km. These CFADs show the locations of positive buoyancy among precipitation modes for the most unstable parcel. The CFAD for the stratiform precipitation mode shows $\bar{\theta}_{eV} - \theta_{eV}$ values near 0 K from surface through 3 km, but above 3 km values become very positive (Fig 5.11a). The CFAD for embedded convective precipitation also shows many 3-hour periods with near zero K $\bar{\theta}_{eV} - \theta_{eV}$ up through 3 km; however, about 10 to 15% of the 3-hour periods have negative $\bar{\theta}_{eV} - \theta_{eV}$ values up through 3 km. $\bar{\theta}_{eV} - \theta_{eV}$ values above 3 km are mostly positive, but 10-20% of values are negative indicating the presence of buoyancy. The CFAD for mostly convective 3-hour periods shows near zero values of $\bar{\theta}_{eV} - \theta_{eV}$ up through 0.5 km. Between 0.5 km and 5.5 km $\bar{\theta}_{eV} - \theta_{eV}$ values are mostly negative. Above 5.5 km most $\bar{\theta}_{eV} - \theta_{eV}$ values become positive. The mostly convective precipitation mode is clearly a convective mode, stratiform precipitation is clearly a stable mode, and embedded convection falls somewhere in-between the two contrasting modes.

Fig. 5.12a illustrates the frequency of potential instability ($\frac{d\bar{\theta}_e}{dz} < 0$) at KSLE for the vertical profiles of mostly stratiform, embedded convective within stratiform and mostly convective periods. Embedded periods have two maximums in frequency of occurrence (near the surface and at 4.5 km altitude). Mostly convective periods have a peak in frequency of potential instability at approximately 2.0 km altitude. Frontal forcing (the presence of which is confirmed by satellite analysis and synoptic variables) likely plays a role in realizing potential instability in many embedded periods. Figure 5.12b illustrates the frequency of vertical wind shear instability for the vertical profiles at KSLE of mostly stratiform, embedded convective within stratiform and mostly convective periods. In terms of frequency of vertical wind shear instability by altitude, there is very little difference between precipitation structures. About a third of soundings for all three precipitation modes (mostly stratiform, embedded, and mostly convective) have vertical wind shear instability near the surface. Very few soundings have vertical wind shear instability above 2 km.

5.3.2 Vertical Structure of Doppler Vertical Velocity

Subjective visual analysis of MRR vertically pointing radar reflectivity data for three cool seasons (2005-06, 2006-07, and 2007-08) found snow fallstreaks to be extremely common. Snow fallstreaks were visually identified in 89% of stratiform 3-hour periods, 95% of embedded 3-hour periods, and 69% of convective 3-hour periods. The height of the earliest detectable snow fallstreak varied, but most snow streaks began above 3 km. For a majority of 3-hour periods, the fallstreaks in snow led to the enhancement of precipitation in the rain layer. The enhancement occurred directly beneath the snow fallstreak and increased the precipitation variability within the rain layer. Fallstreaks in the snow region were of low magnitude and diffuse for about 40% of stratiform periods compared to 10% of the embedded periods. Both stronger and weaker reflectivity fallstreaks in snow modulated surface precipitation variability.

MRR Doppler vertical velocity data are useful for identifying the convective nature of precipitation passing over the instrument. The MRR measures only a single vertical column, so data from the MRR are not representative of what is occurring in the entire scanning radar domain. When interpreting MRR data in this context, higher Doppler vertical velocity values imply higher hydrometeor fall velocity and/or higher downdraft velocity. Higher hydrometeor fall velocities imply that larger hydrometeor sizes developed during a more convective hydrometeor development process. Additionally, higher downdraft velocity would also imply a more convective vertical circulation environment. Higher Doppler vertical velocities and higher variability in Doppler vertical velocity are observed, particularly within the snow layer and to some extent in the rain layer, for embedded periods compared to stratiform periods over the three year period (Fig. 5.13). The percentile differences between the distributions of Doppler vertical velocity for embedded 3-hour periods and mostly stratiform 3-hour periods are statistically significant (using test described in section 3.4) for most vertical levels. Higher values of and higher variability in Doppler vertical velocity are consistent with stronger generating cells yielding large particles. Interpretation of reflectivity is more complex due to possible signal attenuation; therefore the MRR reflectivity data are not presented as vertical profile distributions.

5.4 Lightning Characteristics of Precipitation Modes

Although the Pacific Northwest is not known for frequent lightning strikes, NLDN lightning strike data reveals interesting patterns which may help in understanding the region's intermittent precipitation. MacGorman and Rust's (1998) literature review of lightning studies suggests that lightning strikes are a result of a combination of many factors, but are highly related to the number of graupel-ice interactions that occur under conditions favorable for electrification. Conditions favorable for electrification depend on the residence time and concentrations of graupel, cloud ice, and super cooled cloud water particles within the mixed phase region of a cloud. These factors are influenced by the horizontal and vertical distribution of updraft speed particularly above the 0° C level. The absence of lightning strikes cannot prove the absence of convection, but the presence of frequent lightning strikes confirms the presence of updrafts and sufficient conditions for electrification in the mixed phase region of the cloud. Mean updrafts velocities of $w \gtrsim 6\text{-}7\ ms^{-1}$ are required to maintain the appropriate concentration and mixture of mixed phase particles (Michimoto, 1991; Zipser, 1994, Petersen et al., 1996; MacGorman and Rust, 1998). NLDN strike data combined with GOES IR data indicate that almost 90% of strikes occur at either the cold front or in the cold sector (Fig 5.14). These two regions are also conducive to generating intermittent cellular precipitation (embedded convective within stratiform and mostly convective precipitation). The locations of the lightning maxima with respect to synoptic location are also consistent with Hobbs' (1975) maxima locations of graupel, ice, and water concentrations.

The frequency of lightning strikes is highest just west of the Coast Range, which has frictional convergence between air over water versus land. There are also two terrain-induced convergence hot spots that support locally increased lightning (Fig. 5.15). The southern maximum occurs south of Mount St. Helens over the Columbia River Gorge and the northern maximum occurs near Seattle, WA a region known for localized convergence (Mass, 2008). The 0° C level is lowest near the synoptic cold front and within the cold sector. Based on KSLE sounding stability calculations, these two synoptic regions also contain the parcels with the highest theoretical parcel updraft speed.

5.5 Summary

Examination of data from six years (2002-2008) of operational scanning radar near Portland, Oregon (KRTX), operational sounding data from Salem, Oregon (KSLE), and three years (2005-2008) vertically pointing radar data from Portland, Oregon (MRR) reveals several key atmospheric characteristics regarding cool season precipitation structure in this region. As expected, stratiform precipitation preferentially occurred ahead of the cold front near the warm conveyor belt of the extratropical cyclone. Embedded convective within stratiform precipitation occurred within the warm sector near the surface cold front. Mostly convective precipitation occurred along the cold front and in the cold sector of the extratropical cyclone. The key results are summarized below. The results are synthesized with existing conceptual models in Chapter 6.

Key results:

1) Stratiform precipitation was the most common precipitation mode during the 2002-2008 cool seasons. The last three years experienced an increase in the number embedded and mostly convective 3-hour periods.

2) Most storms follow a typical transition pattern from stratiform precipitation to embedded convective within stratiform precipitation to mostly convective precipitation. The relative frequency of different temporal patterns had considerable inter-annual variability.
3) Periods with embedded convective cells within stratiform precipitation have a frequency of MUCAPE > 0 J kg^{-1} about 2.8 times that of stratiform precipitation by itself. (Fig. 5.9 and Fig 5.10). Of the embedded periods that have zero J kg^{-1} MUCAPE, most are potentially unstable. Combining embedded periods with either MUCAPE > 0 J kg^{-1} or potential instability layers yields up to 90% of embedded periods with active or latent (potential) instability.
4) Hydrostatic instability is more elevated for embedded convective periods compared to mostly convective periods. Most unstable parcels origination heights are more commonly elevated (> 2.5 km) for embedded periods compared to convective periods (0.5 km). There is a strong double maximum in potential instability near the surface and at 4.5 km with embedded periods compared primarily near surface based potential instability with mostly convective periods (Fig 5.12a).
5) Vertical wind shear instability does not appear to play a strong role in explaining differences between precipitation modes (Fig. 5.12b).
6) Pacific Northwest lightning strikes are strongly regulated by geography, occurring most frequently over ocean near the coast line. Where lightning occurs geographically, it tends to occur near the cold front and within the cold sector. Lightning strike data confirms the presence of strong updrafts and favorable lightning electrification conditions.
7) MRR reflectivity data shows nearly ubiquitous fallstreaks in snow originating above 3 km for stratiform and embedded 3-hour periods.
8) MRR Doppler vertical velocity within the snow layer are more variable and have higher maximum values in embedded compared to stratiform. This observation is consistent with stronger generating cells during embedded compared to stratiform

periods. Fallstreaks in snow enhance the rainfall directly below and thus have a direct impact on precipitation variability in the rain layer.

5.6 Chapter Tables

Table. 5.1. 2002-2008 Table of 3-hour periods categorized by two-step intermittent precipitation identification process.

	Cool Seasons						**All**
Precipitation Mode	*2002-03*	*2003-04*	*2004-05*	*2005-06*	*2006-07*	*2007-08*	
Stratiform	93	65	38	79	75	36	386
Embedded	23	14	7	22	35	25	126
Isolated Convection	11	11	7	20	27	22	98
Other	3	8	4	6	5	5	31
Total Events	130	98	56	127	142	88	641

Table. 5.2. Storm temporal patterns (2002-2008). The table lists the first day of the storm pattern. A storm is defined as a period of at least 9-hours within a 24 hour period. A stratiform pattern occurred when stratiform precipitation was present for at least 9 hours with no more than one intermittent 3-hour period during the storm. An intermittent only storm pattern was intermittent for at least 9 hours. A remainder pattern is used to label all other transitions.

Type of Storm Period	2002-03	2003-04	2004-05	2005-06	2006-07	2007-08	Total Storms
Stratiform	12/11, 12/13, 12/14, 01/12, 03/08, 03/13 03/21	01/07, 01/09, 01/23, 01/28, 02/16	11/16, 12/05, 12/26, 3/26	11/01, 11/13, 11/25, 12/28, 12/30, 01/13	02/16, 03/03, 03/24	None	25
Intermittent Only	11/09	02/28	12/08	11/04, 02/02	11/03, 11/05, 11/06, 12/11	11/10, 11/16, 12/06, 12/18, 01/10, 01/12	15
Typical Transition	12/16, 01/03, 01/04, 01/22, 01/26, 01/29, 03/07, 03/09	11/17, 12/24, 02/18	01/17	12/21, 12/26, 12/27, 12/30, 01/07, 01/10, 01/17, 01/30, 03/24	12/13, 12/14, 12/20, 02/09, 02/15, 03/25	11/17, 12/02, 01/03, 02/07, 03/13, 03/23	33
Remainder	None	None	03/19	01/06	11/19, 12/24, 01/02, 01/07	12/24	7
Total Storms	16	9	7	18	17	13	

5.7 Chapter Figures

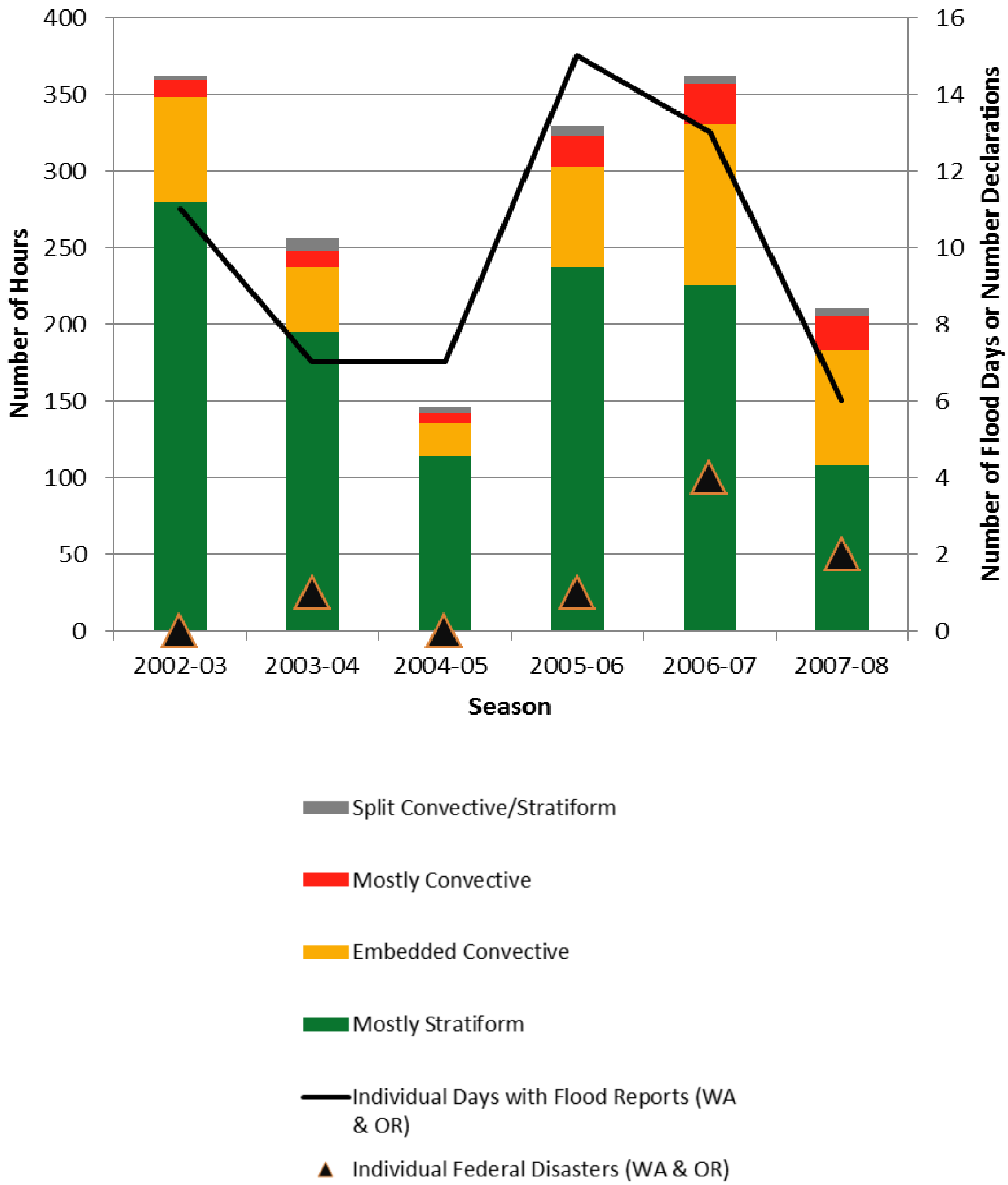

FIG. 5.1. Total number of hours for each precipitation mode by season (2002-2008). The number of flood days and federal disaster declarations are also overlaid.

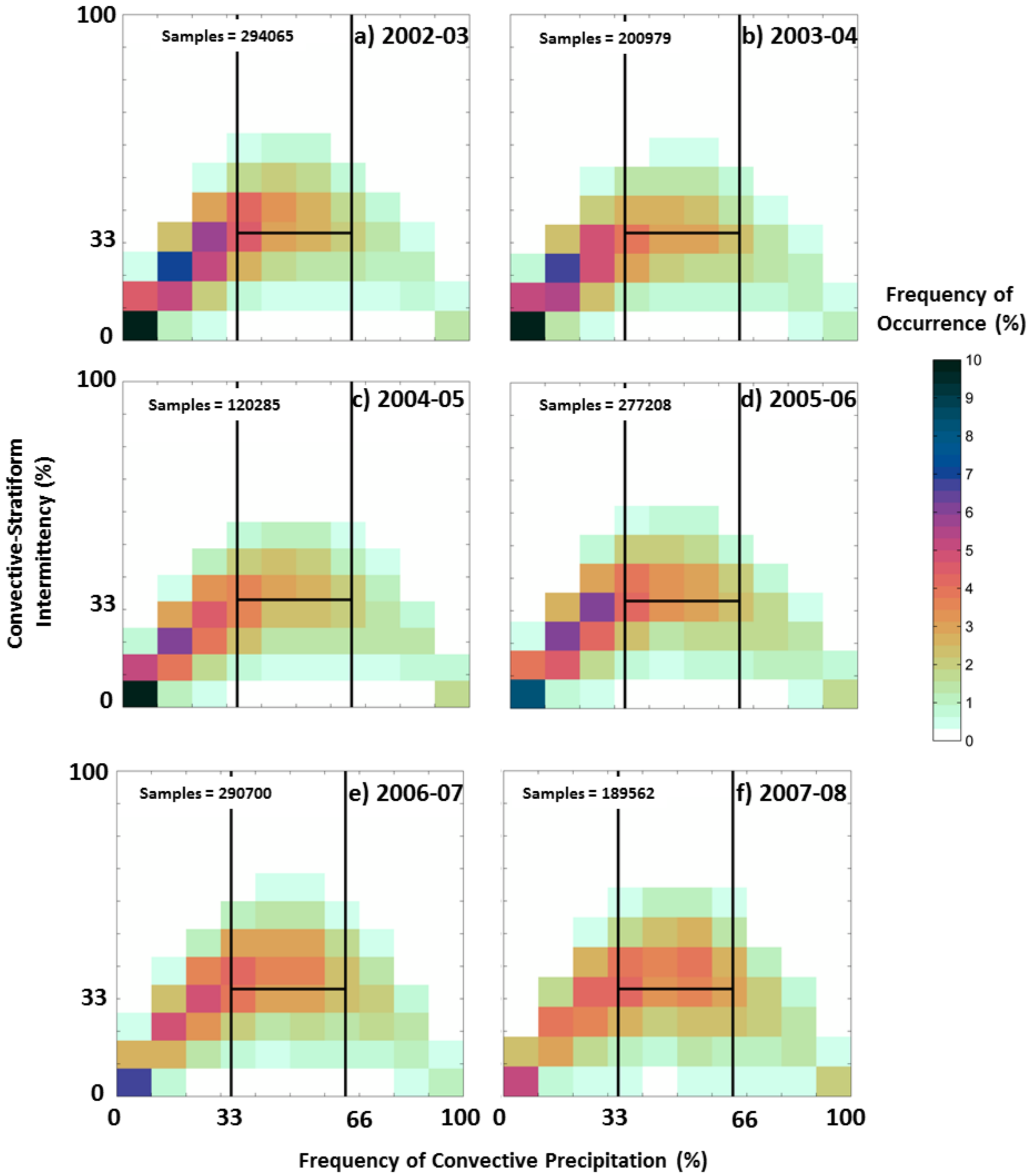

FIG. 5.2. Seasonal precipitation data density diagrams. Panel a) 2002-03, b) 2003-04, c) 2004-05, d) 2005-06, e) 2006-07, and f) 2007-08.

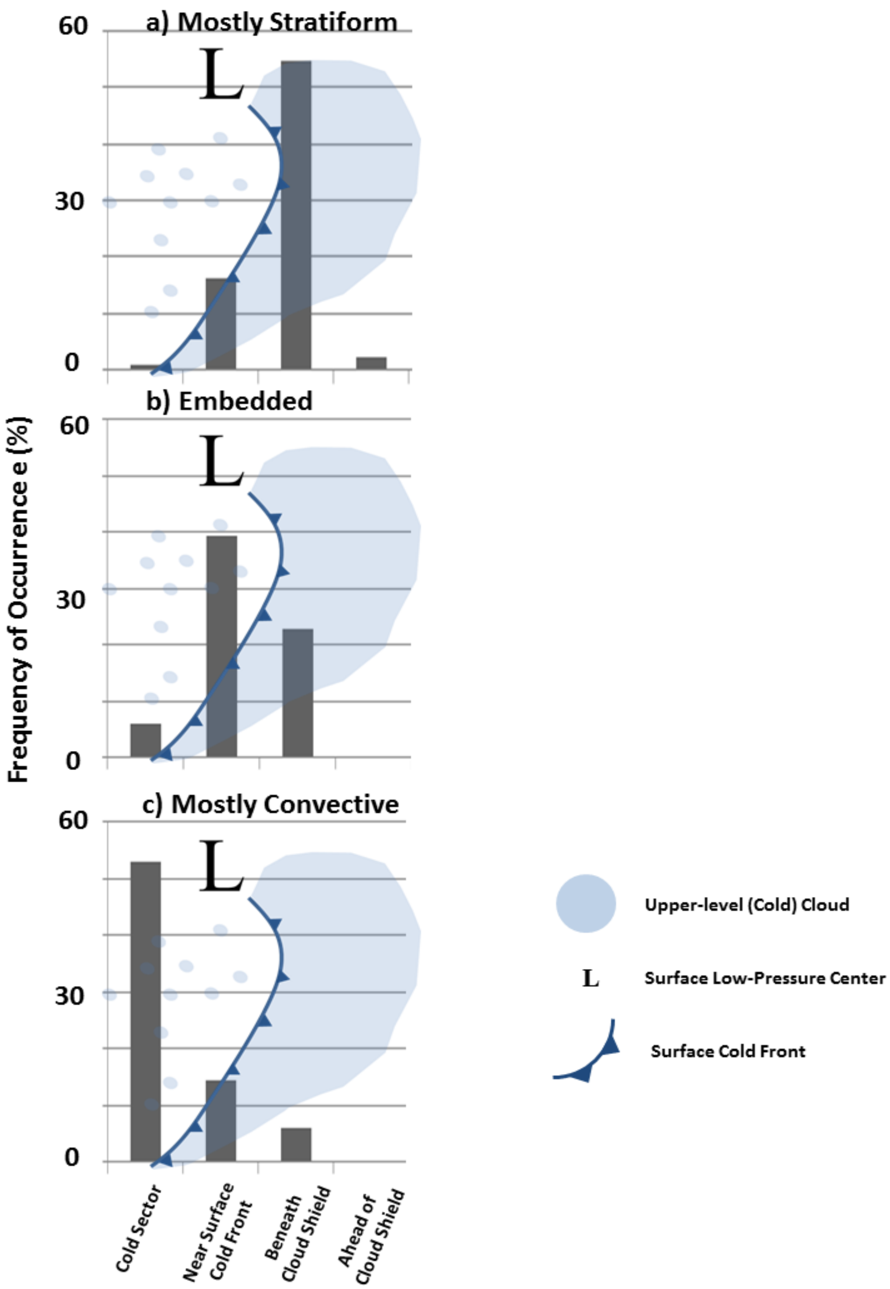

FIG. 5.3. Frequency of precipitation mode occurrence by synoptic location (2002 to 2006). Panel a), b), and c) are for mostly stratiform, embedded convective within stratiform, and mostly convective 3-hour periods, respectively. 3-hour periods not falling into the cold sector, near surface cold front, beneath could shield, and ahead of cloud shield criteria are not shown in the figure.

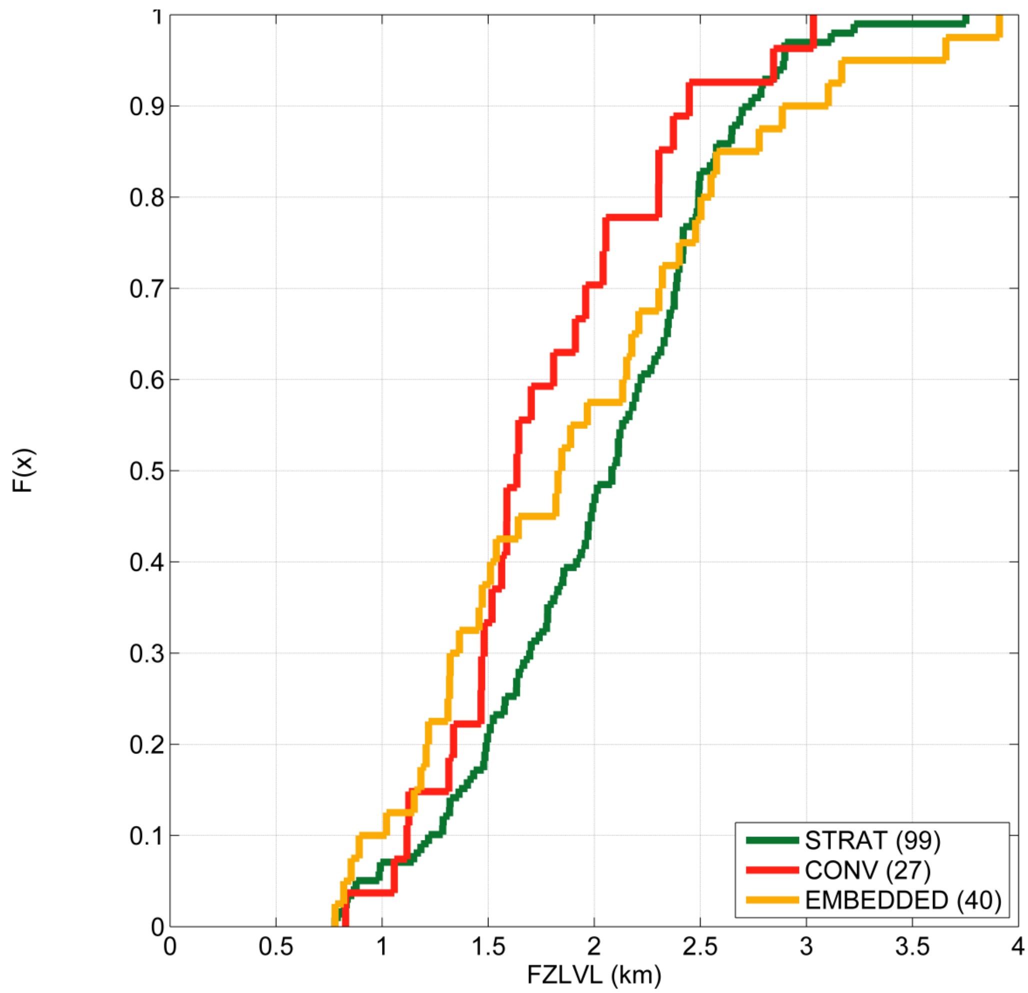

FIG. 5.4. Cumulative distribution functions for zero degree Celsius level from KSLE for 2002 to 2008 for periods where 0° C level > 1.4 km altitude. Red lines are mostly convective 3-hour periods, gold lines embedded convective within stratiform 3-hour periods, and green lines are mostly stratiform 3-hour periods.

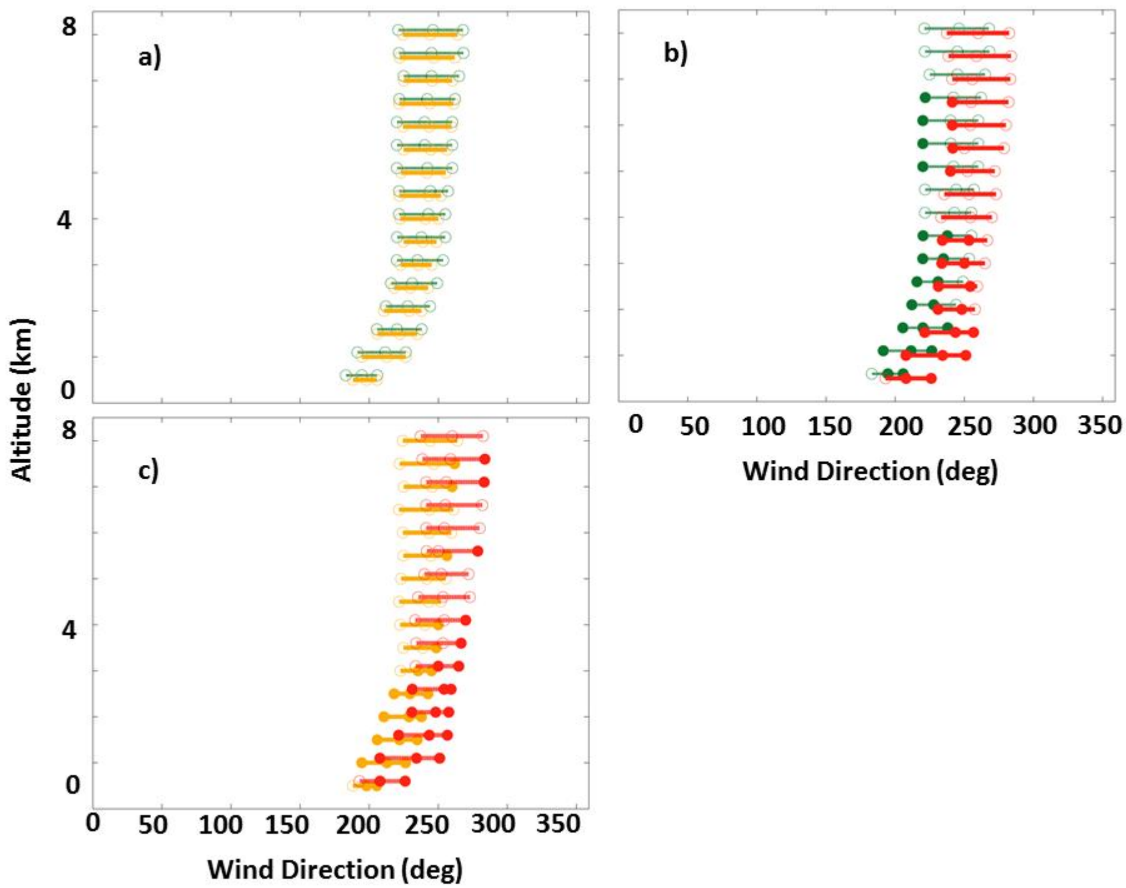

FIG. 5.5. Wind direction profiles as distributions for KSLE soundings with the 0° C level from 2002 to 2008. Circles are 25th, 50th, and 75th percentiles. Panel a) is a comparison between mostly stratiform 3-hour periods and embedded convective within stratiform 3-hour periods, panel b) is a comparison between mostly convective 3-hour periods and mostly stratiform 3-hour periods, and panel c) is a comparison between mostly convective 3-hour periods and embedded within stratiform 3-hour periods. Filled circles represent percentile differences which are statistically significant (alpha level 95%). Unfilled circles represent percentile differences that are not statistically significant. Red lines and circles are mostly convective 3-hour periods, gold lines and circles are embedded convective within stratiform 3-hour periods, and green lines and circles are mostly stratiform 3-hour periods.

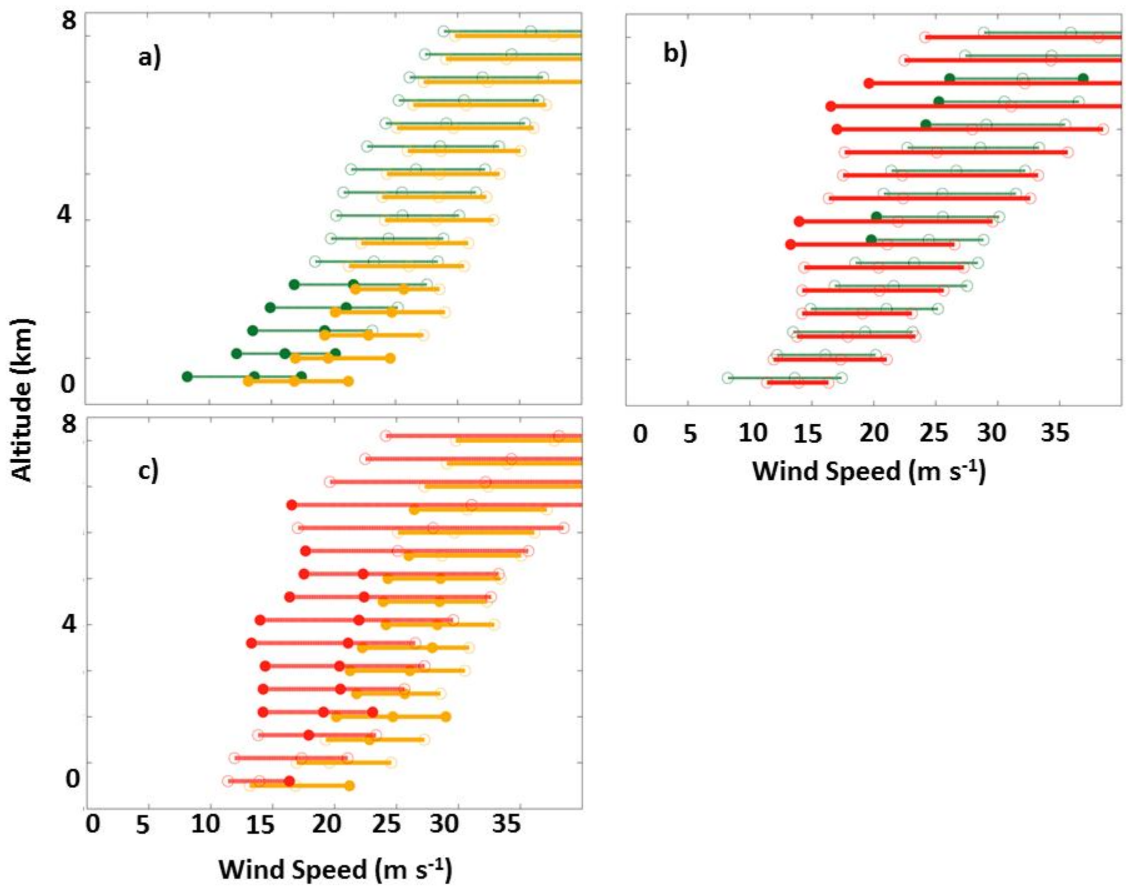

FIG. 5.6. As in 5.5 but for wind speed profiles.

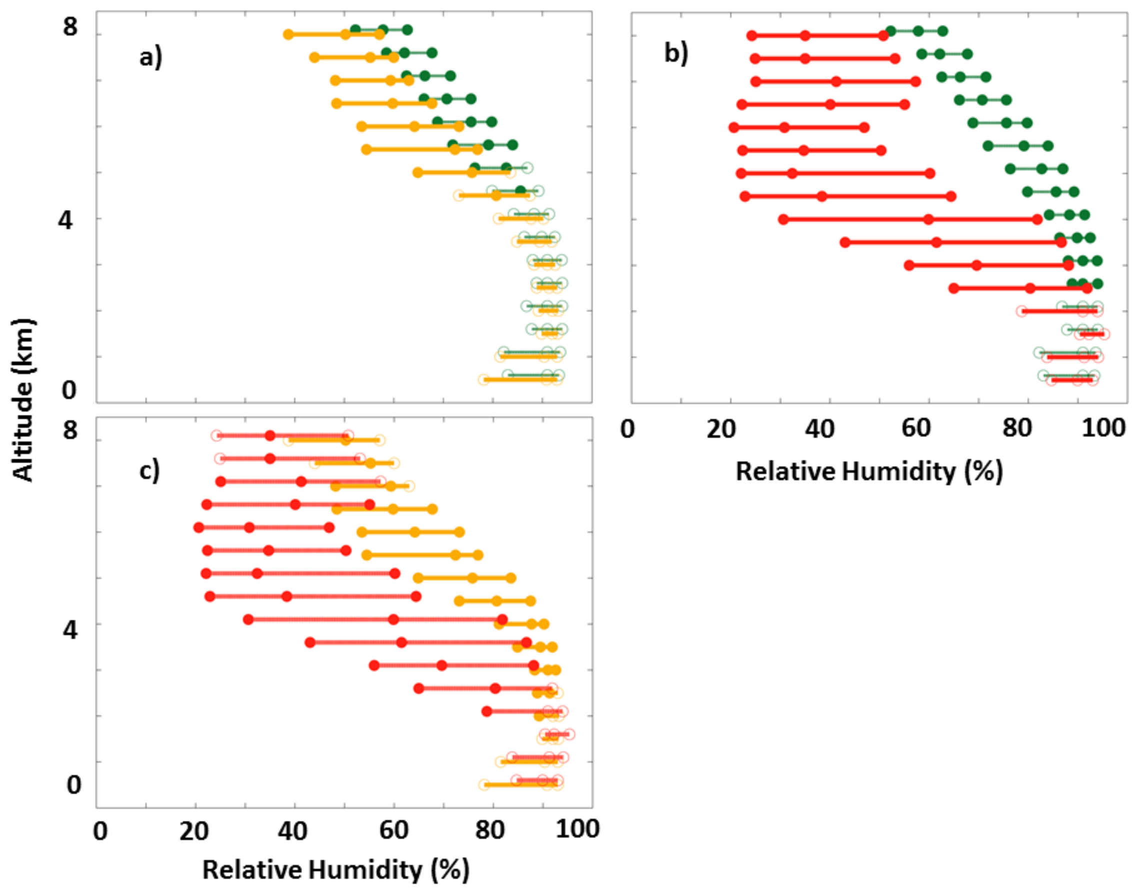

FIG. 5.7. As in 5.5 but for relative humidity profiles.

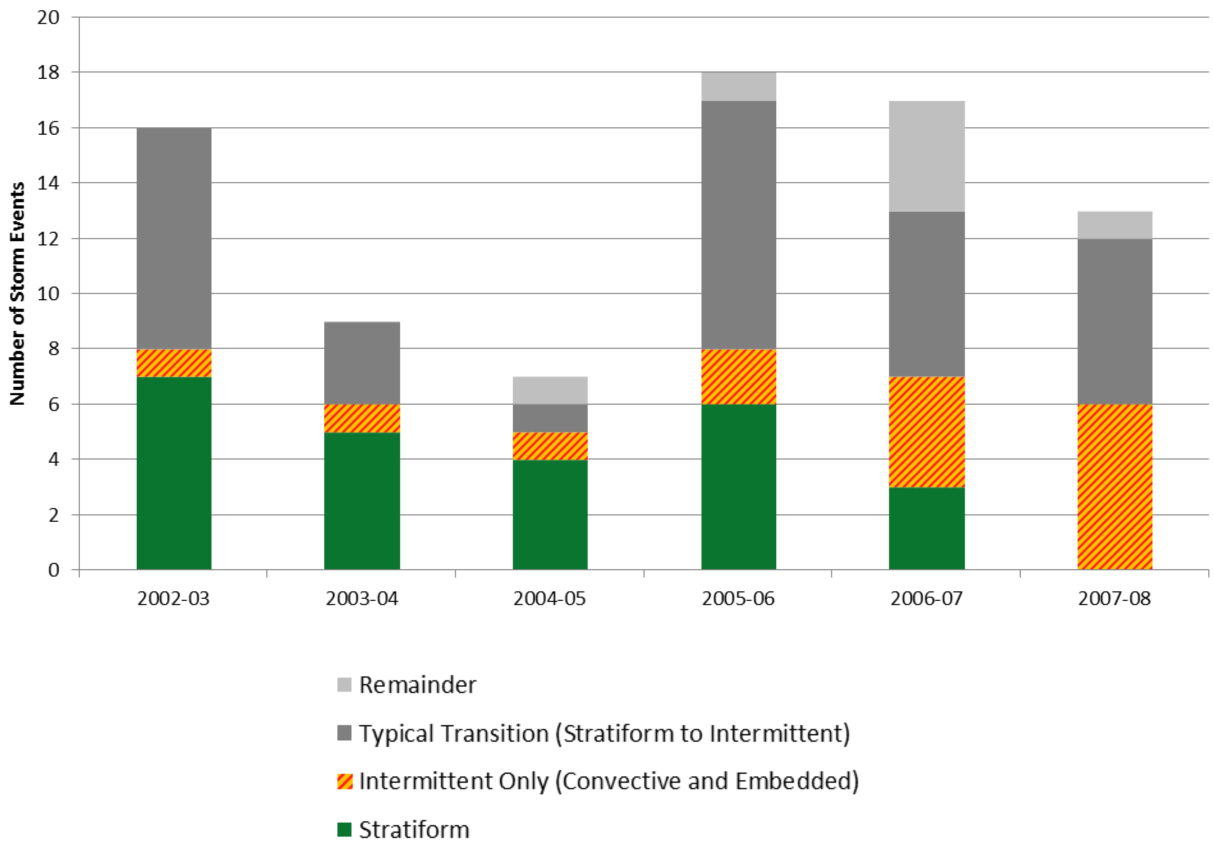

FIG. 5.8. Summary of cyclone-scale temporal pattern types by season (2002-2008).

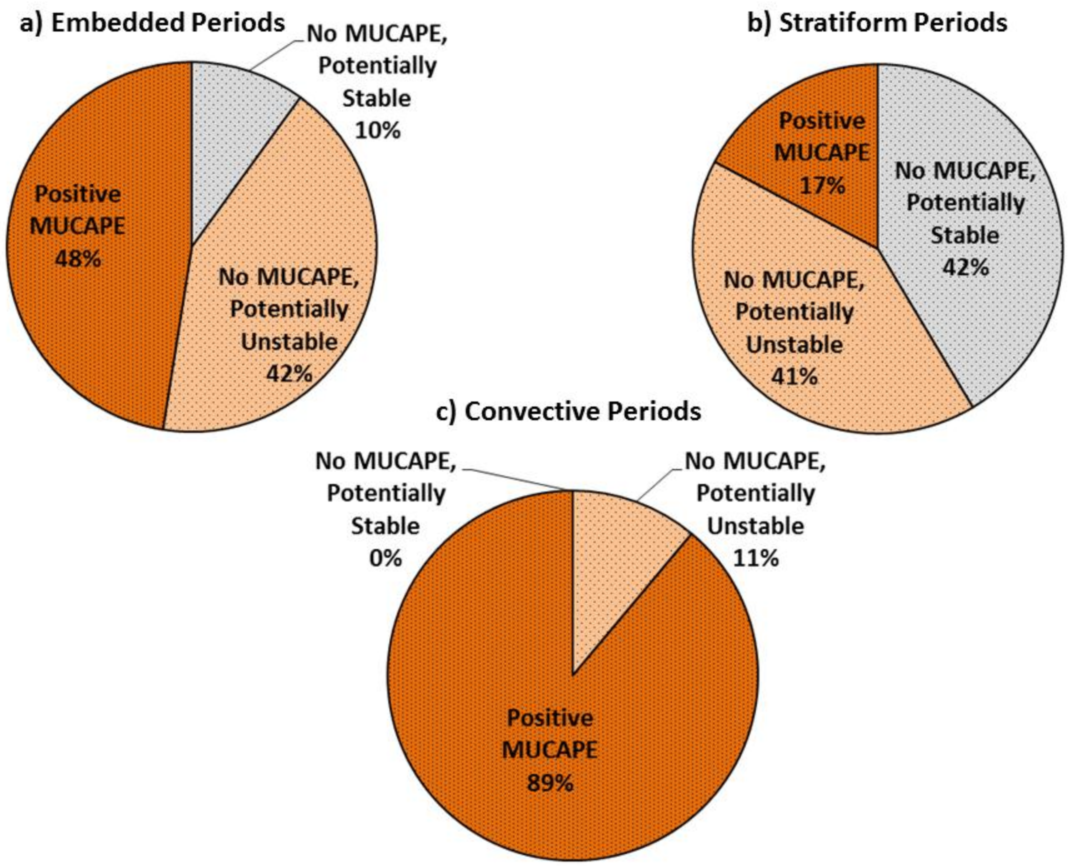

FIG. 5.9. Fraction of precipitation periods that have soundings with 1) positive MUCAPE, 2) No MUCAPE, but potentially unstable ($\frac{d\theta_e}{dz} < 0$) for at least two 500 meter layers, 3) no MUCAPE and potentially stable for KSLE from 2002 to 2008. (a) embedded within convective stratiform precipitation (40 periods) (b) mostly stratiform precipitation (99 periods) (c) mostly convective precipitation (27 periods). Orange areas have positive MUCAPE or potential instability.

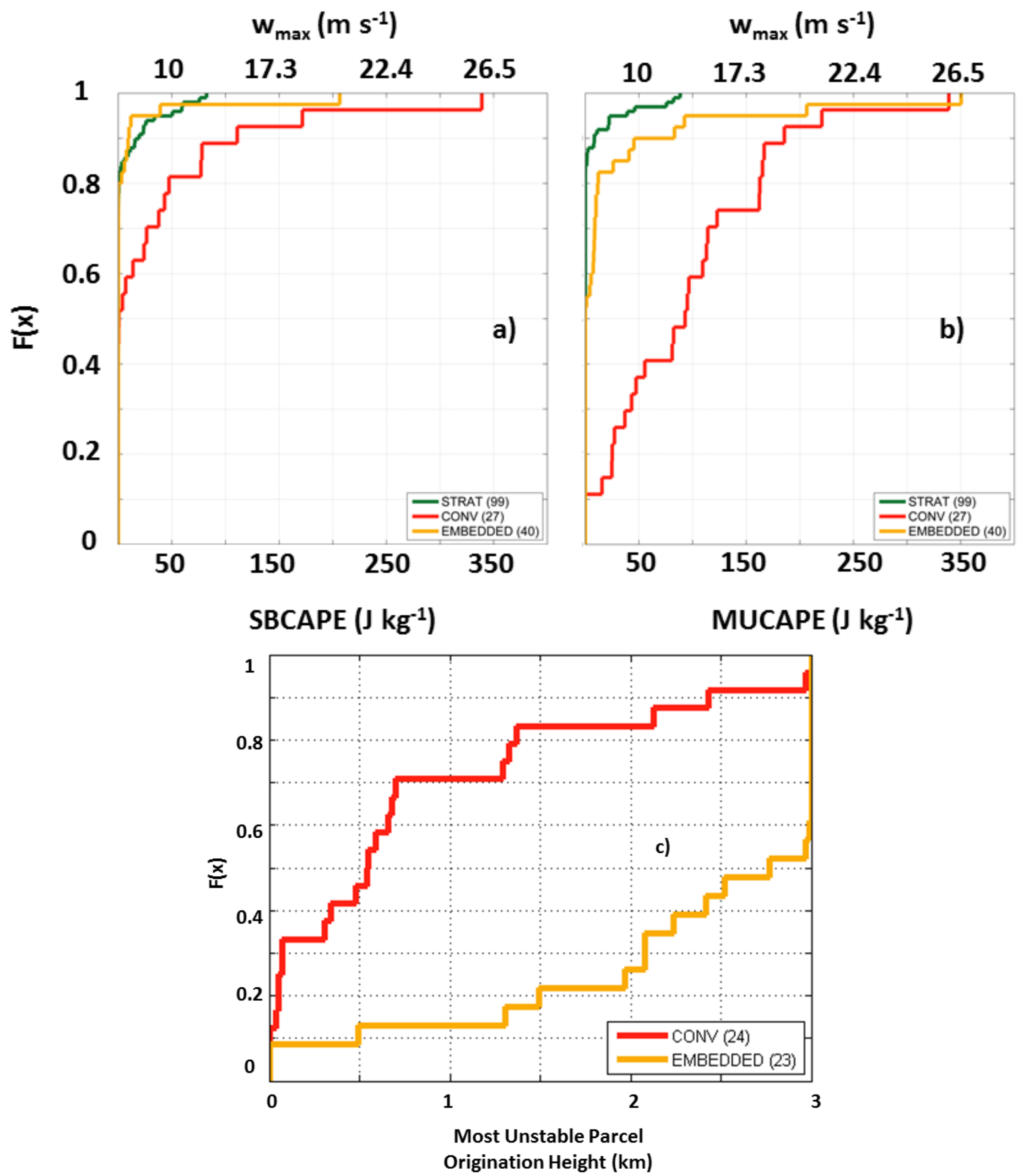

FIG. 5.10. Cumulative distribution functions for (a) surface based convective available potential energy (CAPE) and (b) most unstable parcel CAPE (MUCAPE), and (c) most unstable parcel origination height from KSLE for 2002 to 2008 with 0° C level >1.4 km altitude. Red lines are mostly convective 3-hour periods, gold lines embedded convective within stratiform 3-hour periods, and green lines are mostly stratiform 3-hour periods.

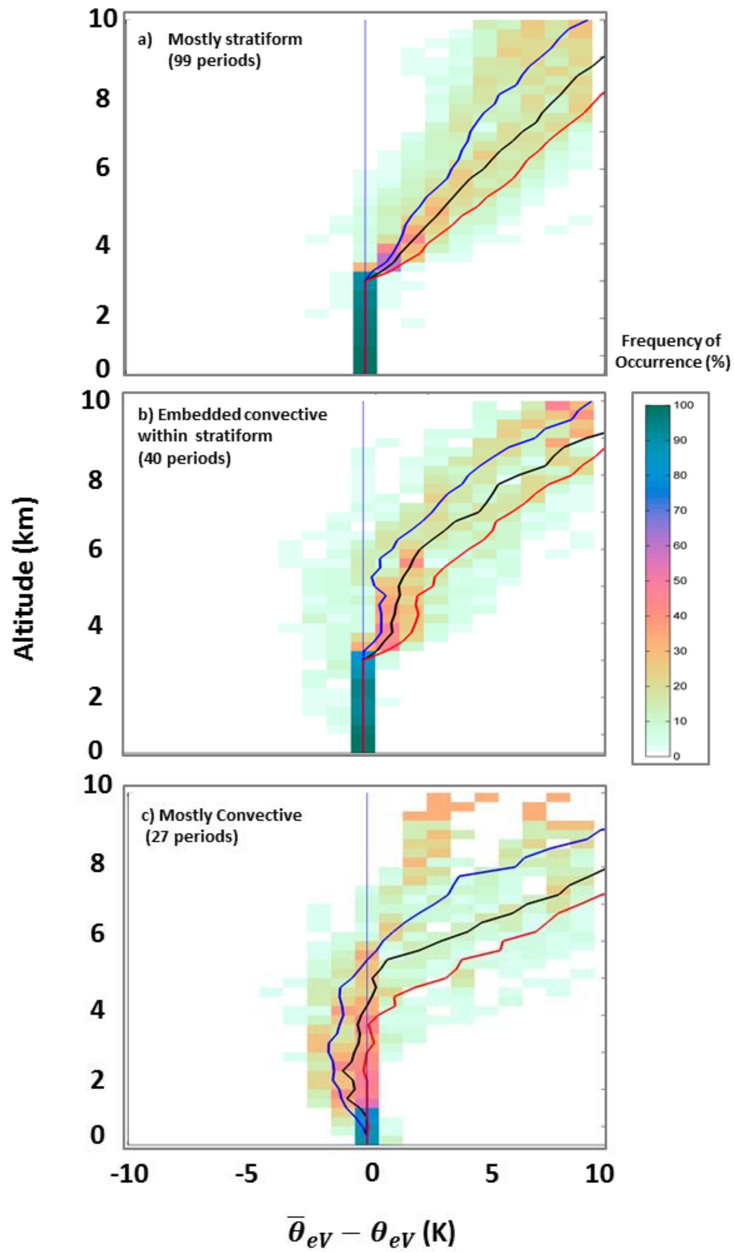

FIG. 5.11. Most unstable parcel $\overline{\theta}_{eV} - \theta_{eV}$ frequency of occurrence by altitude from KSLE for 2002-2008 for a) mostly stratiform periods, b) embedded convective within stratiform periods, and c) mostly convective periods. Blue, black, and red lines are the 25th, 50th, and 75th percentiles, respectively.

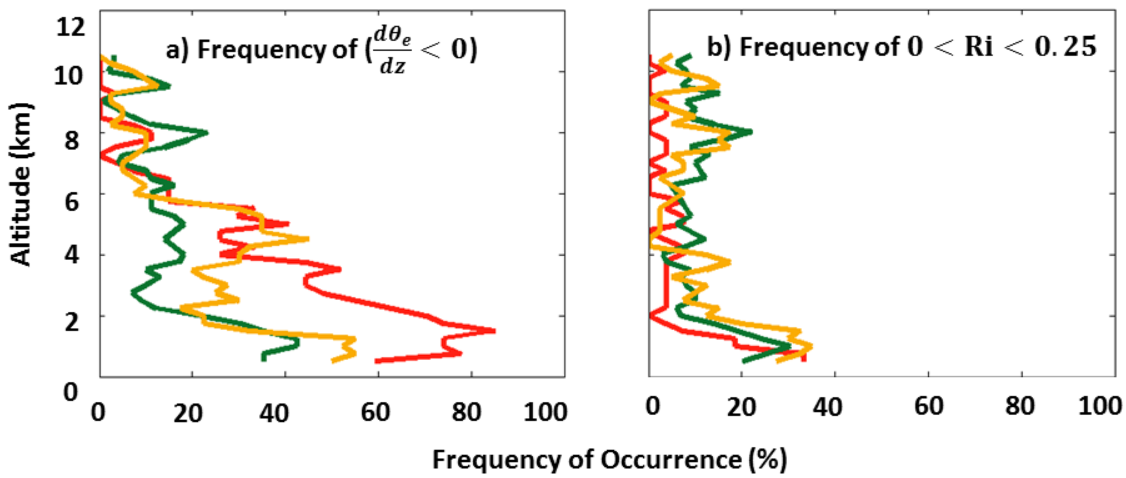

FIG. 5.12. Vertical profiles of the frequency of potential instability and shear instability for KSLE from 2002 to 2008. Panel a) is the frequency of potential instability ($\frac{d\bar{\theta}_e}{dz} < 0$) by altitude, and panel b) is the frequency of vertical wind shear (0 < Ri < 0.25) instability by altitude. Red lines are mostly convective 3-hour periods, gold lines embedded convective within stratiform 3-hour periods, and green lines are mostly stratiform 3-hour periods. Values are calculated over 500 meter layers.

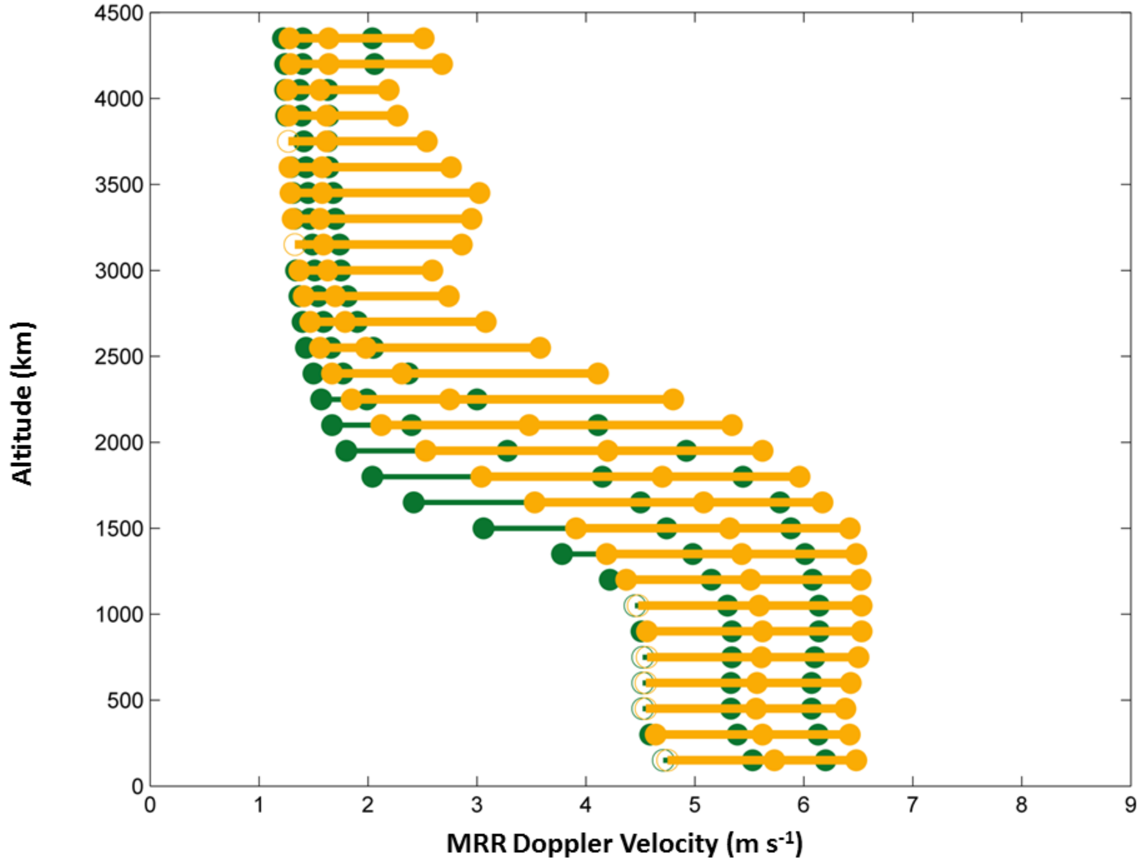

FIG. 5.13. 2005-2008. Vertical profile of MRR Doppler velocity distributions. Circles are 25th, 50th, and 75th percentiles. Filled circles represent percentile differences which are statistically significant. Unfilled circles represent percentile differences that are not statistically significant. Gold lines and circles are embedded convective within stratiform 3-hour periods, while green lines and circles are mostly stratiform 3-hour periods.

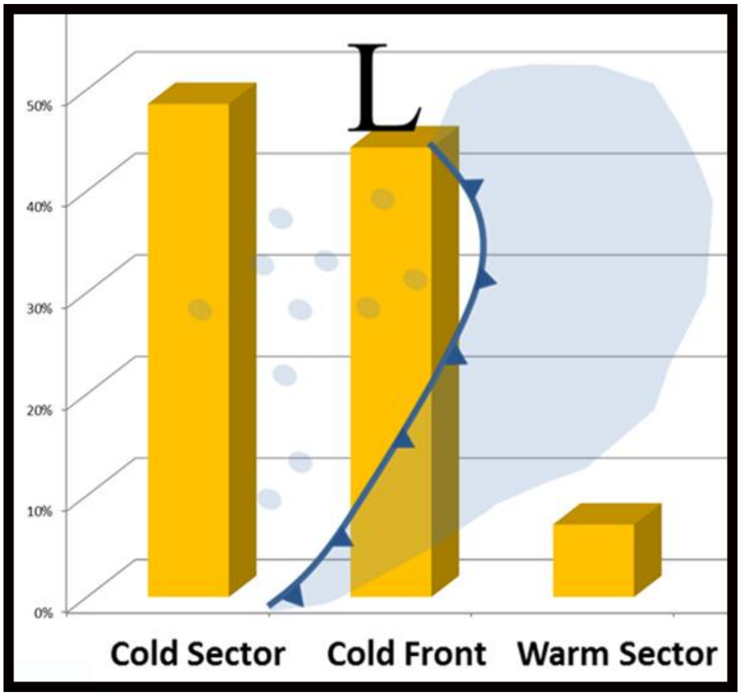

FIG. 5.14. NLDN 2005-06. Frequency (%) of lightning occurrence relative to extratropical cyclone location.

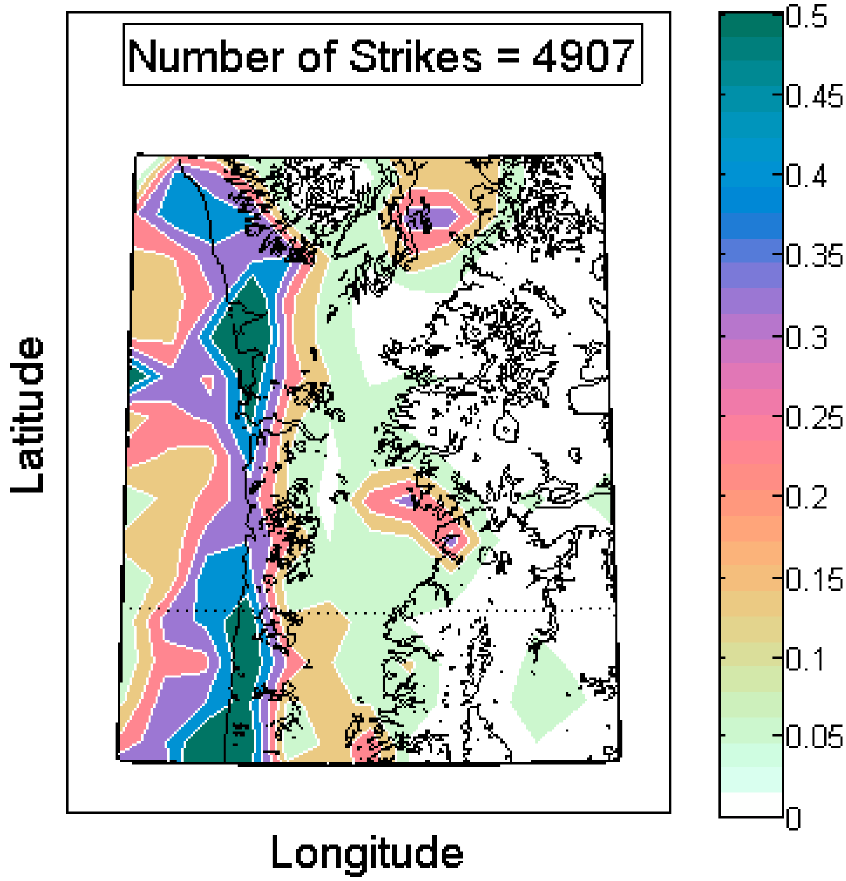

FIG. 5.15. NLDN 2002-2008 cool season spatial frequency (%) of lightning strike occurrence.

Chapter 6 – Concluding Remarks

6.1 Synthesis of Results with Background Literature

The primary goal of this study was to determine the sources of instability typically associated with convective cells embedded within stratiform precipitation for Pacific Northwest cool season storms. The testable hypothesis was *the frequency of precipitation periods with positive buoyancy (as measured by most unstable parcel convective available potential energy) should be higher (> 2x) for embedded convective within stratiform precipitation periods than for mostly stratiform precipitation periods.* Based on analysis of the KSLE sounding data, the hypothesis is confirmed. Periods with embedded convective cells within stratiform precipitation have a frequency of MUCAPE > 0 J kg^{-1} about 2.8 times that of stratiform precipitation by itself. The analysis indicated that 48% of embedded period soundings have MUCAPE > 0 J kg^{-1}. Buoyancy is more commonly aloft (> 3 km) for embedded periods compared to convective periods.

As expected, embedded convection within stratiform precipitation was found to most commonly occur ahead of the surface cold front near the warm conveyor belt of extratropical cyclones. Embedded cells were more prevalent closer to (but ahead of) the surface cold front. This observation is very consistent with the split cold front conceptual model proposed by Browning and Monk (1982) (Fig. 1.10), which relates elevated convection to drier and cooler air aloft that is moving ahead of the surface cold front. The observed locations of mostly convective precipitation along and behind the surface cold front, and of stratiform precipitation near the warm conveyor belt of the extratropical cyclone are consistent with conceptual models and observations from Nagle and Serebreny (1962), Hobbs (1975), and Hobbs (1978). The Browning and Monk split cold front conceptual model shows a cross-section of the warm front. The warm-front is an assumed synoptic feature for this present research, since warm fronts were not specifically identified in the analysis.

Fall streaks in snow were nearly ubiquitous within both embedded and stratiform precipitation. These fall streaks represent the seeder-feeder process in action. Rain fallstreaks (precipitation enhancement in the rain layer) were often directly below the snow fallstreaks.

The fallstreaks varied in intensity and tended to be weaker in stratiform precipitation and stronger in embedded precipitation. Occasionally a fall streak was sufficiently strong to stand out from the background precipitation as an embedded convective cell.

The observation that embedded convection was frequently elevated during the six year data record, rather than near the surface, has microphysical implications. The seeder-feeder process occurs to some extent in nearly every Pacific Northwest cool season storm and is a primary cause of rain fallstreaks and at least a subset of embedded convective cells. This result also highlights a weakness of compositing several storms to obtain a "typical" environment. Compositing tends to washout the signature of seeder cells and fall streaks in reflectivity and of measures of hydrostatic instability that occur in vertical layers between 2 to 6 km altitudes. Hence, while mathematically correct, such composites miss important aspects of the typical storm environment.

The size of this data set, 1,923 hours of precipitation, over 6 cool seasons also allows us to put several previous findings about Pacific Northwest precipitation into context. Although this present research did not deal directly with orographic precipitation enhancement, it does address synoptic and mesoscale precipitation processes that frequently occur near terrain. Rotunno and Houze's (2007) exclusion of the seeder-feeder mechanism as a mode of cellularity for orographic precipitation is inconsistent with the observations presented here and the works of Browning (1974), and the numerous CYCLES studies cited throughout this dissertation. Our observations and past research show the seeder-feeder mechanism directly modulating surface rain rate without terrain present (e.g. Appendix A).

Pre-2000 conceptual models of Pacific Northwest cool season storms included the presences of upper-level instability and seeder cells ahead of the cold front. However, the importance of these features to precipitation variability in the warm sector has been underemphasized in recent literature (Fuhrer and Schar, 2005; Houze and Medina, 2005; Rotunno and Houze, 2007; Cannon et al., 2011; Ralph et al., 2011). A revised schematic that includes the findings of this study is shown relative to the schematics of Nagle and Serebreny (1962) as adapted by Medina et al. (2007) and Browning and Monk (1982 (Fig. 6.1). The previous conceptual models located in the top two rows of Figure 6.1 indicate precipitation becoming cellular, but do not clearly connect the upper-level instability cells, hydrostatic instability, and microphysical processes to increased precipitation intermittency and intensity variability at the surface. Results from this research show that hydrostatic instability is a good general predictor for cellularity for cool season intermittent precipitation over the Willamette Valley. The vertical wind shear instability mechanism for generating cellularity as described by Houze and Medina (2005) and Medina et al. (2007) is not a general feature in the multi-year dataset. These present results may not be applicable directly over terrain, but do show common structures occurring over the Willamette Valley. The new conceptual model in the bottom panel clearly connects upper-level hydrostatic instability to generating cells aloft, with increasing cellularity and variability of precipitation intensity in both the snow layer and the rain layer. The new conceptual model in Figure 6.1 assumes microphysical characteristics (i.e. hydrometeor type, etc.) based on previous work in literature and MRR reflectivity and Doppler vertical velocity data.

While simulating cool season embedded convective within stratiform precipitation in the Pacific Northwest is possible with idealized and operational modeling, simulating embedded convection with real extratropical cyclones is practically difficult. Many idealized modeling studies of cool season embedded convection near terrain do not account for elevated unstable layers and the seeder-feeder mechanism (Cannon et al. 2011, Fig. 1.17). When numerical models are run at 12 km and coarser resolutions, the seeder feeder process is treated as a sub-grid scale process, if at all. With operational and idealized numerical models now using horizontal grid spacing of 3 km, 1.3 km and smaller, there is a need for model dynamics and microphysics to address the seeder-feeder mechanism. Ensuring that numerical weather prediction models adequately capture hydrostatic instability aloft and the seeder-feeder mechanism will improve the precipitation fields within the warm sector of extratropical cyclones where most of the precipitation accumulation often occurs. More accurate quantitative precipitation forecasts that include better representations of warm sector precipitation variability will in-turn aid flood forecasting and fresh water management.

6.2 Suggested Future Work

This study has shown that hydrostatic instability plays a lead role in modulating precipitation intermittency during periods of cool season precipitation near Portland, Oregon. Specifically, elevated convective cells associated with the seeder-feeder mechanism affect precipitation rate near the surface during embedded convective within stratiform precipitation periods. A review of the literature indicates that the seeder-feeder mechanism is often not simulated in either idealized or operational modeling settings. Future work with observations should address the role of synoptic (such as frontal circulations and conditional symmetric instability) and terrain features on developing environmental conditions conducive to an elevated convective seeder cells. A field project with 3-hourly upper air sounding launches at sites forming a polygon from the Pacific Ocean west of the coast to the Willamette Valley are needed to address this question with observations. Future modeling efforts of embedded convective within stratiform precipitation should ensure that upper-level hydrostatic instability and the seeder feeder mechanism are adequately represented. Information on the lifecycle of convective cells embedded within stratiform precipitation as compared to those in convective regions would also be of value in understanding the underlying physics of precipitation variability. Additionally, information on how convective cells respond to the terrain of the Coastal Range and the Cascade Mountains will help tie together the work of this study with other work on orographic precipitation enhancement in this region. Results from this study are also relevant to hydrology community. What are the impacts of precipitation intermittency on small urban watersheds with quick response times? Can this new information aid in streamflow forecasting?

6.3 Chapter Figures

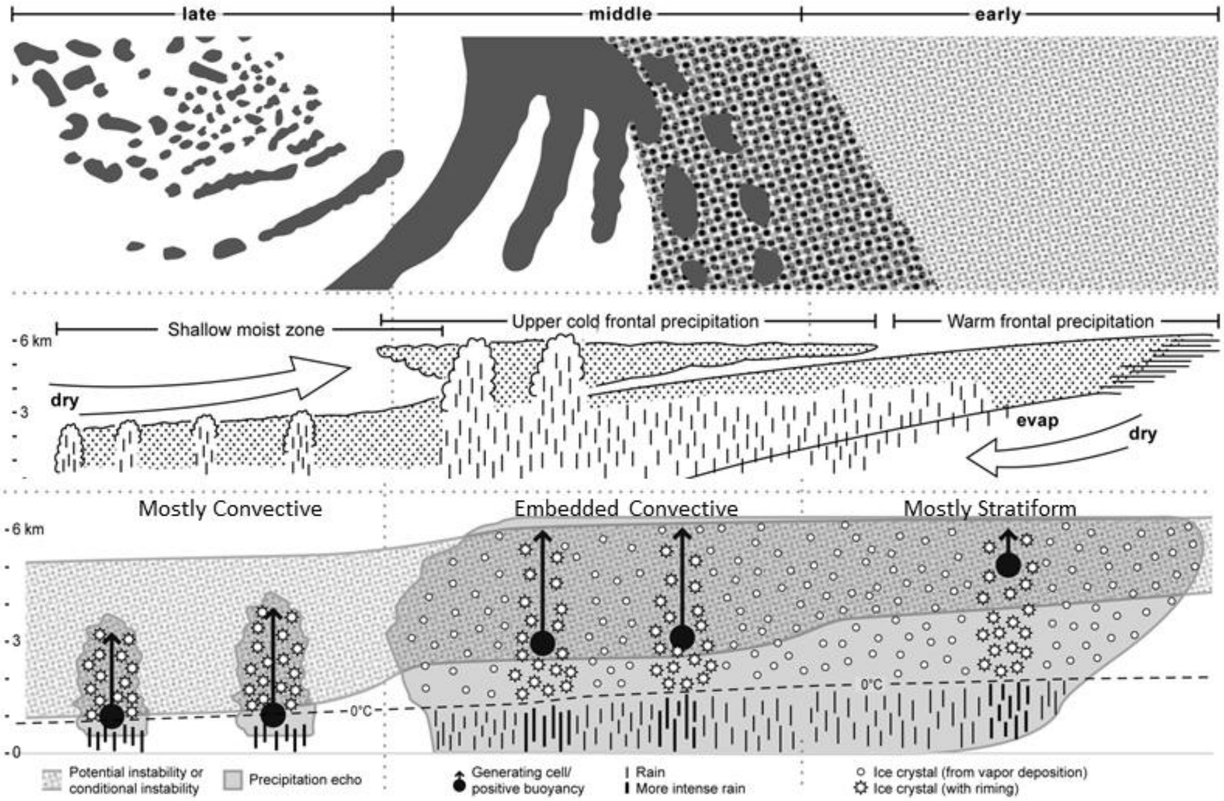

FIG. 6.1. A conceptual model that indicates elevated seeder cells in split-front impacting rain layer precipitation intermittency. Seeder cells aloft develop more intense precipitation in the snow layer above warm conveyor belt. Precipitation in the rain layer is enhanced immediately beneath the seeder cells aloft leading to higher intensity and more intermittent precipitation. The top panel is based on a figure from Nagle and Serebreny (1962) adapted by Medina et al. (2007). The middle panel is based on a figure from Browning and Monk (1982). The bottom panel is based on the observations from the current work. The illustration of this figure was aided by Beth Tully.

References

Bader, M. J., G. S. Forbes, J.R. Grant, R. B. E. Lilley, and A. J. Waters, 1995: *Images in weather forecasting: A practical guide for interpreting satellite and radar imagery*. University Press, Cambridge. pp. 499.

Bao, J.-W., S. A. Michelson, P. J. Neiman, F. M. Ralph, and J. M. Wilczak, 2006: Interpretation of Enhanced Integrated Water Vapor Bands Associated with Extratropical Cyclones: Their Formation and Connection to Tropical Moisture. *Mon. Wea. Rev.,* **134**, 1063-1080.

Baum, R. L. and J. W. Godt, 2010: Early warning of rainfall-induced shallow landslides and debris flows in the USA. *Landslides*, **7**, 259-272.

Bolton, D., 1980: The Computation of Equivalent Potential Temperature. *Mon. Wea. Rev.*, **108**, 1046-1053.

Browning, K.A., F. F. Hill, and C.W. Pardoe, 1974: Structure and mechanism of precipitation and the effect of orography on wintertime warm sector. *Quart. J. Met. Soc.*, **100**, 309-330.

_____, and G. A. Monk, 1982: A Simple Model for the Synoptic Analysis of Cold Fronts. *Quart. J. Met. Soc.*, **108**, 435-452.

_____, 1986: Conceptual models of precipitation systems. *Meteorol. Mag.*, **114**, 293-319.

_____, 1990: Organization of Clouds and Precipitation in Extratropical Cyclones. *Extratropical Cyclones: The Erik Palmen Memorial Volume*. American Meteorological Society, 129-153.

Cannon, D. J., D. J. Kirshbaum, and S. L. Gray, 2012: Under what conditions does embedded convection enhance orographic precipitation? *Quart. J. Met. Soc.*, **138**, 391-406.

Churchill, D. D., and R. A. Houze Jr., 1984: Development and structure of winter monsoon cloud clusters on 10 December 1978. *J. Atmos. Sci.,* **41,** 933–960.

Colle, B. A., 2004: Sensitivity of orographic precipitation to changing ambient conditions and terrain geometries: An idealized modeling perspective. *J. Atmos. Sci.*, **61**, 588-606.

_____, B. A., Y. Lin, S. Medina, and B. F. Smull, 2008: Orographic Modification of Convection and Flow Kinematics by the Oregon Coast Range and Cascades during IMPROVE-2. *Mon. Wea. Rev.*, **136**, 3894-3916.

Cotton, W. R., G. H. Bryan, S. C. Van Den Heever, 2011: Storm and Cloud Dynamics. 2nd ed. Academic Press, 809.

Doswell, C. A., 1987: The Distinction between Large-Scale and Mesoscale Contribution Severe Convection: A Case Study Example. *Wea. Forecasting,* **2**, 3-16.

_____, and E. N. Rasmussen, 1994: The Effect of Neglecting the Virtual Temperature Correction on CAPE Calculations. *Wea. Forecasting*, **9**, 625-629.

Doviak, R. J. and D. S. Zrnic, 1993: *Doppler Radar and Weather Observations*. Dover Publications, 2nd ed., pp. 562

Durran D. R., and J. B. Klemp, 1982: On the effects of moisture on the Brunt–Väisälä frequency. *J. Atmos. Sci*., **39**, 2152–2158.

Emanuel, K., 1994: *Atmospheric Convection*. Oxford University Press, 580 pp.

FEMA, cited 2012: Declared Disasters by Year or State. [http://www.fema.gov/news/disaster_totals_annual.fema].

Fuhrer, O. and Christoph Schar, 2005: Embedded Cellular Convection in Moist Flow past Topography. *J. Atmos*., **62**, 2810-2828.

Gunn, K. L. S., M. P. Langleben, A. S. Dennis, and B. A. Power, 1954: Radar Evidence of a Generating Level for Snow. *Journal of Meteorology*, **11**, 20-26.

Harrold, T. W., 1973: Mechanisms influencing the distribution of precipitation baroclinic distrubances. *Quart. J. Roy. Meteor. Soc.*, **99**, 232-251.

Herzegh, P. H. and P. V. Hobbs, 1980: The Mesoscale and Microscale Structure and Organization of Clouds and Precipitation in Midlatitude Cyclones. II: Warm-Frontal Clouds. *J. Atmos*., **37**, 597-611.

Hobbs, P. V., T. J. Matejka, P. H. Herzegh, J. D. Locatelli, and R. A. Houze, 1980: The Mesoscale and Microscale Structure and Organization of Clouds and Precipitation in Midlatitude Cyclones. I: A Case Study of a Cold Front. *J. Atmos*., **37**, 568-596.

______, 1975: The Nature of Winter Clouds and Precipitation in the Cascade Mountains and their Modification by Artificial Seeding. Part I: Natural Conditions. *J.Appl. Meteor.*, **14**, 783-804.

_____, 1978: Organization and Structure of Clouds and Precipitation on the Mesoscale and Microscale in Cyclonic Storms. *Reviews of Geophysics and Space Physics*, **16**, 741-755.

Houze, R. A., P. V. Hobbs, K. R. Biswas, and W. M. Davis, 1976: Mesoscale Rainbands in Extratropical Cyclones, *Mon. Wea. Rev.*, **104**, 868-878.

______, 1993: *Cloud Dynamics*. Academic Press, 573 pp.

_____, 1997: Stratiform precipitation in regions of convection: A meteorological paradox? *Bull. Amer. Meteor. Soc.*, **78,** 2179–2196.

_____, and Medina, S., 2005: Turbulence as a Mechanism for Orographic Precipitation Enhancement. *J. Atmos*., **62**, 3599-3623.

Hughes, M., A. Hall, and R G. Fovell, 2009: Blocking in Areas of Complex Topography, and Its Influences on Rainfall Distribution. *J. Atmos*., **66**, 508-518.

Jorgensen, D. P., Z. Pu, P. O. G. Persson, and W. K. Tao, 2003: Variations Associated with Cores and Gaps of a Pacific Narrow Cold Frontal Rainband. *Mon. Wea. Rev.*, **131,** 2705-2729.

Kessler, E., 1969: On the Distribution and Continuity of Water Substance in Atmospheric Circulation. *Meteor. Monogr.*, No. **10**, Amer. Meteor. Soc., 84 pp.

Kirshbaum, D. J. and D. R. Durran, 2004: Factors Governing Cellular Convection in Orographic Precipitation. *J. Atmos*., **61**, 682-698.

_____, and R. B. Smith, 2008: Temperature and moist-stability effects on midlatitude orographic precipitation. *Quart. J. Roy. Meteor. Soc.*, **134**, 1183-1199.

Lin, Y., B. A. Colle, and S. E. Yuter 2012: Impact of moisture flux and freezing level on simulated orographic precipitation errors over the Pacific Northwest, *J. Hydro*., submitted.

Locatelli, J. D., M. T. Stoelinga, M. F. Garvert, and P. V. Hobbs, 2005: The IMPROVE-1 Storm of 1-2 February 2001. Part I: Development of a Forward-Titled Cold Front and Warm Occlusion. *J. Atmos*., **62**, 3431-3455.

Löffler-Mang, M, M. Kunz, and W. Schmidt, 1999: On the performance of a low-cost K-band doppler radar for quantitative rain measurement. *J. Atmos.Oceanic Technol*., 16, 379-387.

Lundquist, J.D., J. R. Minder, P. J. Nieman, and E. Sukovich, 2010: Relationship between Barrier Jet Heights, Orographic Precipitation Gradients, and Streamflow in the Northern Sierra Nevada. *J.Hydrometeor*., **11**, 1141-1156.

Matejka, T. J., R. A. Houze, and P. V. Hobbs, 1980: Microphysics and dynamics of clouds associated with mesoscale rainbands in extratropical cyclones. *Quart. J. Roy. Meteor. Soc.*, **106**, 29-56.

Markowski, P. and Y. Richardson, 2010: *Mesoscale Meteorology in Midlatitudes*. Wiley-Blackwell, pp. 407.

Marshall, J. S., 1953: Precipitation Trajectories and Patterns. *Journal of Meteorology*, **10**, 25-29.

Mass, C., 2008: *The Weather of the Pacific Northwest*. University of Washington Press, 280 pp.

MacGorman, D. R. and W. David Rust, 1998: *The Electrical Nature of Storms*. Oxford University Press, 422 pp.

McCann, D. W., 1995: Three-Dimensional Computations of Equivalent Potential Vorticity. *Wea. Forecasting*, **10**, 798-802.

McCaul, E. W., C. Cohen, and C. Kirkpatrick, 2005: The Sensitivity of Simulated Storm Structure, Intensity, and Precipitation Efficiency to Environmental Temperature. *Mon. Wea. Rev.*, **133**, 3015-3037.

McNulty, R. P., 1978: On Upper Tropospheric Kinematics and Severe Weather Occurrence. *Mon. Wea. Rev.*, **106**, 662-672.

Medina, S., E. Sukovich, and R. A. Houze, 2007: Vertical Structures of Precipitation in Cyclones Crossing the Oregon Cascades. *Mon. Wea. Rev*., **135**, 3265-3586.

Michimoto, K., 1991: A study of radar echoes and their relation to lightning discharge of thunderclouds in the Hokuriku District. Part I: Observation and analysis of thunderclouds in summer and winter. *J. Meteor. Soc. Japan*, **69**, 327-35.

Nagle, R. E., and S. M. Serebreny, 1962: Radar precipitation echo and satellite cloud observations of a maritime cyclone. *J.Appl. Meteor.*, **1,** 279–295.

NCAR, 2012: Reorder. [http://www.eol.ucar.edu/rdp/home/reorder.html].

Neiman, P. J. and Coauthors, 2008: Meteorological Characteristics and Overland Precipitation Impacts of Atmospheric Rivers Affecting the West Coast of North America Based on Eight Years of SSM/I Satellite Observations. *J. Hydrometeor*., **9**, 22-47.

_____, E. M. Sukovich, F. M. Ralph, and M. Hughes, 2010: A Seven-Year Wind Profiler-Based Climatology of the Windward Barrier Jet along California's Northern Sierra Nevada. *Mon. Wea. Rev.*, **138**, 1206-1233.

NCDC, cited 2012: Storm Events Database. [http://www.ncdc.noaa.gov].

Panziera, L., and U. Germann, 2010: The relationship between airflow and orographic precipitation in the Southern Alps as revealed by weather radar. *Quart. J. Roy. Meteor. Soc.*, **136**, 222–238.

Parsons, D. B. and P. V. Hobbs, 1983: The Mesoscale and Microscale Structure and Organization of Clouds and Precipitation in Midlatitude Cyclones. XI: Comparisons between Observational and Theoretical Aspects of Rainbands. *J. Atmos. Sci.*, **40**, 2377-2397.

Peters, G., B. Fischer, and T. Andersson, 2002: Rain observations with a vertically looking Micro Rain Radar (MRR). *Boreal Environment Research*, **7**,353-362.

_____, B. Fischer, H. Münster, M. Clemens, and A. Wagner, 2005: Profiles of raindrop size distributions as retrieved by microrain radars. *J. Applied Meteor.*, **44**, 1930-1949.

Petersen, W.A., S.A., Rutledge, and R.E. Orville, 1996: Cloud-to-ground lightning observations to TOGA COARE: Selected results and lighting location algorithms. *Mon. Wea. Rev*., **124**. 602-620.

Ralph, F.M., P. J. Neiman, and R. Rotunno, 2005: Dropsonde Observations in Low-Level Jets over the Northeastern Pacific Ocean from CALJET-1998 and PACJET-2001: Mean Vertical-Profile and Atmospheric-River Characteristics. *Mon. Wea. Rev.*, **133**, 889-910.

_____, P. J. Neiman, G. A. Wick, S. I. Gutman, M. D. Dettinger, D. R. Cayan, and A. B. White, 2006: Flooding on California's Russian River: Role atmospheric rivers. *Geophysical Research Letters*, **33**, 1-5.

_____, and Coauthors, 2011: A Multi-Scale Observational Case Study of a Pacific Atmospheric River Exhibiting Tropical-Extratropical Connections and a Mesoscale Frontal Wave. *Mon. Wea. Rev*., **139**, 1169-1189.

Reeves, H. D., Y-L. Lin, and R. Rotunno, 2008: Dynamic forcing and mesoscale variability of heavy precipitation events over the Sierra Nevada Mountains. *Mon. Wea. Rev.*, **136**, 62-77.

Roe, G. H., 2005: Orographic Precipitation. *Annu. Rev. Earth Planet. Sci*., **33**, 645–71.

Rotunno, R. and R. A. Houze, 2007: Lessons on orographic precipitation from the Mesoscale Alpine Programme. *Quart. J. Met. Soc*., **133**, 811-830.

Rutledge, S. A. and P. V. Hobbs, 1983: The Mesoscale and Microscale Structure and Organization of Clouds and Precipitation in Midlatitude Cyclones. VIII: A Model for the "Seeder-Feeder" Process in Warm-Frontal Rainbands. *J. Atmos. Sci.,* **40**, 1185-1206.

Schultz, D. M. and P. N. Schumacher, 1999: The Use and Misuse of Conditional Symmetric Instability. *Mon. Wea. Rev*., **127**, 2709-2732.

_____, P.N., Schumacher, and C.A. Doswell, 2000: The Intricacies of Instabilities. *Mon. Wea. Rev*., **128**, 4143-4148.

Sharp, J. and C. F. Mass, 2004: Columbia Gorge Gap Winds: Their Climatological Influence and Synoptic Evolution. *Wea. Forecasting*, **19**, 970-992.

Smith, R. B. I. Barstad, and L. Bonneau, 2005: Orographic Precipitation and Oregon's Climate Transition. *J. Atmos*., 62, 177-191.

Steiner, M., R. A. Houze, and S. E. Yuter, 1995: Climatological Characterization of Three-Dimensional Storm Structure from Operational Radar and Rain Gauge Data. *J. Appl. Met*., **34**, 1978-2007.

Väisälä, cited 2012: Brochure. [http://www.vaisala.com/Vaisala%20Documents/Brochures%20and%20Datasheets/NLDN-brochure-B210412EN-F-low.pdf]

Wernli, H. and C. Schwierz, 2006: Surface Cyclones in the ERA-40 Dataset (1958-2001). Part I: Novel Identification Method and Global Climatology. *J. Atmos*., **63**, 2486-2507.

Westrick, K. J., C. F. Mass, 2001: An Evaluation of a High-Resolution Hydrometeorological Modeling System for Prediction of a Cool-Season Flood Event in a Coastal Mountainous Watershed. *J. Hydrometeorology*., **2**, 161-179.

Williams, E. and N. Renno, 1993: An Analysis of the Conditional Instability of the Tropical Atmosphere. *Mon. Wea. Rev*., **121**, 21-36.

Wilks, D. S., 2006: *Statistical Methods in the Atmospheric Sciences*. 2nd ed. Elsevier, 627 pp.

Woods, P. W., M. T. Stoelinga, J. D. Locatelli, and P. V. Hobbs, 2005: Microphysical Processes and Synergistic Interaction between Frontal and Orographic Forcing of Precipitation during the 13 December 2001 Improve-2 Event over the Oregon Cascades. *J. Atmos*., **62**, 3493-3519.

Yu, Cheng-ku and B. F. Smull, 2000: Airborne Doppler Observations of a Landfalling Cold Front Upstream of Steep Coastal Orography. *Mon. Wea. Rev.*, **128**, 1577-1603.

Yuter, S. E. and R. A. Houze, Jr., 1997: Measurements of Raindrop Size Distributions over the Pacific Warm Pool and Implications for Z-R Relations. *J. Appl. Met.*, **36**, 847-867.

______, and R. A. Houze, Jr., 2003: Microphysical modes of precipitation growth determined by S-band vertically pointing radar in orographic precipitation during MAP. *Quart. J. Met. Soc*., **129**, 455-476.

_____, and coauthors, 2005: Physical Characterization of Tropical Oceanic Convection Observed in KWAJEX. *J. Appl. Met.*, **44**, 385-414.

_____, D. A. Stark, J. A. Crouch, M. J. Payne, and B. A. Colle, 2011: The impact of varying environmental conditions on the spatial and temporal patterns of orographic precipitation over the Pacific Northwest near Portland, Oregon. *J. Hydrometeorology*., **12**, 329-351.

Zhu, Y. and R. E. Newell, 1998: A Proposed Algorithm for Moisture Fluxes from Atmospheric Rivers. *Mon. Wea. Rev.*, **126**, 725-733.

Zipser, E. J., 1994: Deep cumulonimbus clouds systems in the tropics with and without lightning. *Mon. Wea. Rev*, **122**, 1837-51.

Appendices

Appendix A – Impact of Embedded Convective within Stratiform Precipitation on Streamflow

A.1 Example

A conceptually easy way to understand the impact of convective precipitation versus stratiform precipitation on regional rainfall is to compare the evolution of precipitation radar data with measurements from a streamflow gage that responds quickly to local precipitation. The Fanno Creek watershed, located west of Portland, Oregon is a small ($\approx$ 6 km^2) urban watershed with a quick response time to local precipitation events (Fig A.1). Drainage in urban watersheds is rapid, since surfaces such as concrete, asphalt, sewage drainage systems, and/or other man-made structures are relatively impervious to rainfall.

To illustrate how intermittent and variable intensity precipitation modulates streamflow, we use an example of convective cells embedded within stratiform precipitation from 14 December 2006 (as in Chapter 4). Figure A.2 is a snapshot of the evolution of rain for the Portland, Oregon radar domain. The plan view reflectivity figures indicate more intense precipitation in warm colors. The areas of convective precipitation identified in the plan view reflectivity figure (A.2a) are associated with vertical columns of reflectivity as illustrated in the southwest to northeast vertical cross-sections of reflectivity (Fig A.2b). Information from vertical cross-section figures aids in concluding that the column of strong radar echo in the plan view is associated with convective type precipitation.

The streamflow gage data in Fig. A.2c shows two pulses of runoff, one before and one after 17 UTC. The first stronger pulse (-3 hours side) corresponds to convective cells and the right side of Fig A.2b and the second pulse (+3 hours side) corresponds to cells to the left side of figure A.2b. This example shows, with a snapshot view, how intense pulses of precipitation during can affect streamflow. Repeated pulses of higher intensity precipitation serve to increase streamflow rates and over time increase the likelihood of flooding.

A.2 Appendix Figures

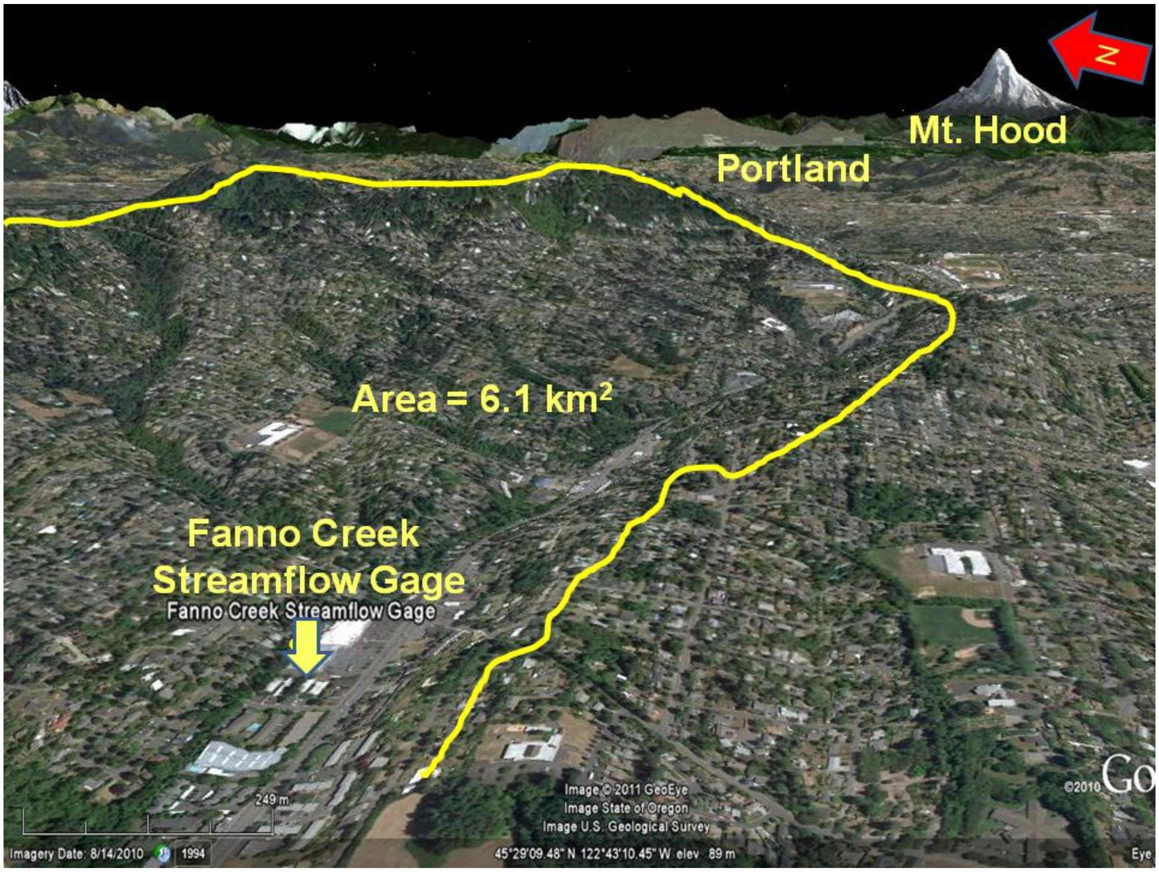

FIG. A.1. Google Earth Watershed Map of Small Fanno Creek Watershed near Portland, Oregon. The yellow line outlines the approximate boundary of the watershed. Terrain features are exaggerated to emphasize watershed boundaries.

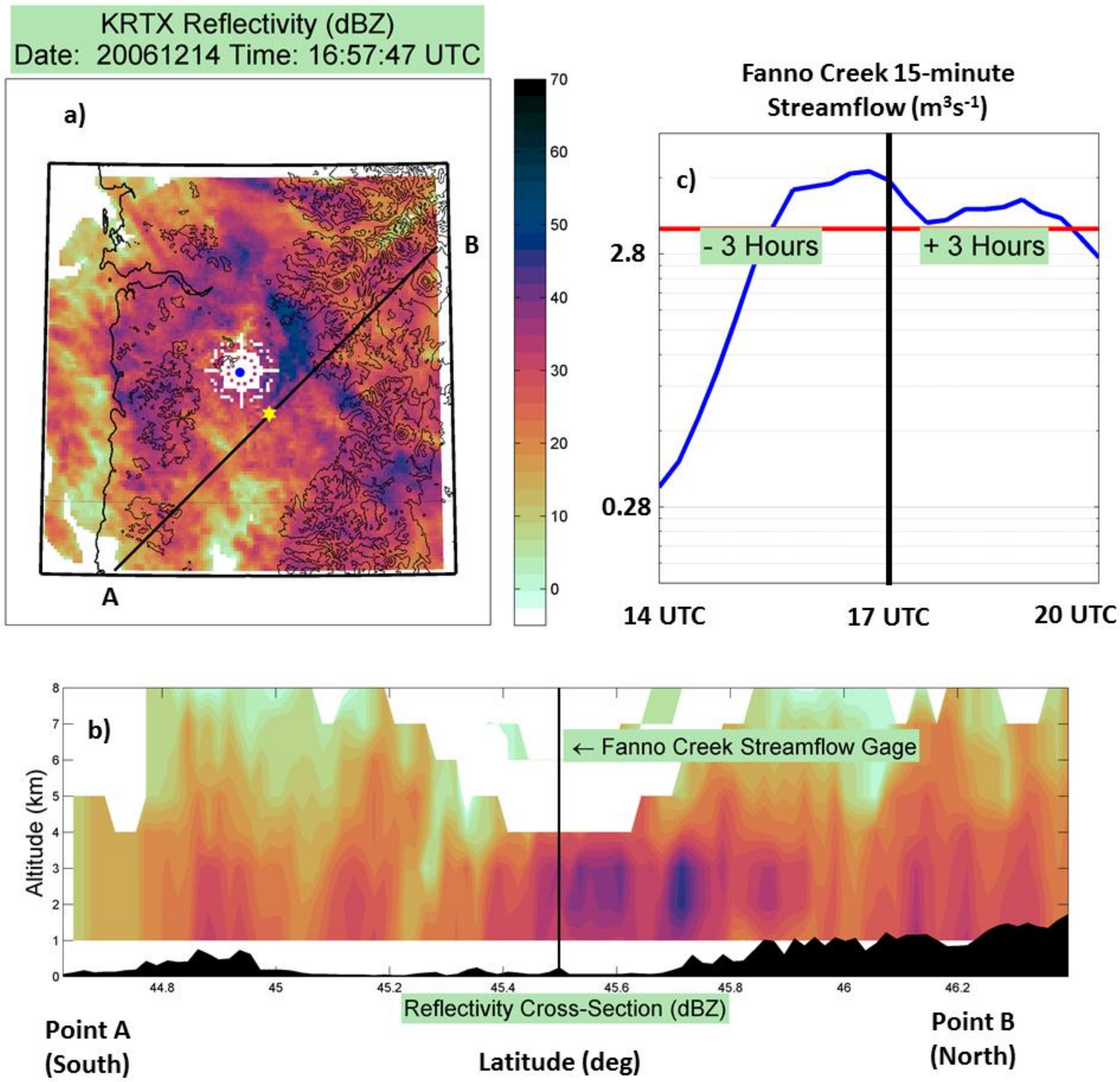

FIG. A.2. Fanno Creek streamflow example. a) KRTX 0.5 degree elevation slice of reflectivity (dBZ) at 16:57:47 UTC on 14 December 2006, b) South-North cross-section (indicated by line through panel a) over the Fanno Creek streamflow gage (yellow star in panel a) for the same time as panel a), and c) USGS Fanno creek streamflow discharge (Gage #. 14206900) at 17 UTC on 14 December 2006, also showing streamflow discharge 3-hours before and 17 UTC.

Appendix B – Ray Path Equations

The location of the radar beam relative to earth is assumed to follow closely the ray path equations in Doviak and Zrnik (1993). The beam height relative to earth's surface is defined as:

$$h = [s_r{}^2 + (k_e a)^2 + 2 s_r k_e a \sin\theta_e]^{1/2} - k_e a\ , \quad (1)$$

where r is the slant-range path distance (along the beam), a is the earth's radius plus antenna height, and θ_e is the elevation angle. k_e is defined as:

$$k_e = \frac{1}{1 + a(\frac{dn}{dh})}\ ,$$

where n is the refractive index. The earth path distance (i.e. follows earth's curvature) equation is defined as:

$$s_e = k_e a \sin^{-1}\left(\frac{s_r \cos\theta_e}{k_e a + h}\right).$$

Appendix C – Thermodynamic Equations

1) Potential temperature: $\theta = T\left(\frac{p_0}{p}\right)^{\frac{R}{c_p}}$, is the temperature of an air parcel if the parcel is expanded or compressed adiabatically to the reference pressure p_0. R is dry gas constant. c_p is the specific heat for a constant pressure (Markowski, 2010).

2) Saturation equivalent potential temperature, $\theta_e^* = \theta \exp\left(\frac{l_v r_s}{c_p T}\right)$, is the temperature of a saturated air parcel if all of the water vapor were to condense in a adiabatic, isobaric process. θ is the potential temperature, l_v is the specific latent heat of vaporization, r_s is the saturation mixing ratio, and T is the temperature (Markowski, 2010).

3) Equivalent potential temperature, $\theta_e = \theta \exp\left(\frac{3376}{T_L - 2.54} r_v (1 + 0.81 r_v)\right)$, is the is the temperature of a moist but unsaturated air parcel if all of the water vapor were to condense in a adiabatic, isobaric process. T_L is the temperature at the parcel's equilibrium level and is defined as $T_L = \left(\frac{2840}{3.5\log(T) - \log(\frac{e_v}{100}) - 4.805}\right) + 55$ (Bolton, 1980; Markowski, 2010).

Appendix D – A Brief Review Inertial and Symmetric Instability

The following explanation is based on McCann (1995), Schultz and Schumacher (1999), and Markoswki and Richardson (2010). Inertial instability generates a horizontal acceleration which causes a horizontal displacement Δy. This horizontal acceleration is defined as:

$$\frac{d^2 \Delta y}{dt^2} = f(u_g - u),$$

where f is the Coriolis parameter, u_g is the geostrophic wind component in the x-direction (east-west) and u is the total wind in the x-direction. An inertial instability is best thought of in terms of conservation of angular momentum. For purely geostrophic flow, geostrophic absolute momentum is written as:

$$M_g \equiv u_g - fy \, .$$

An inertially unstable condition exists when geostrophic absolute momentum increases in the y-direction (poleward), which is indicated by:

$$\frac{\partial M_g}{\partial y} > 0 \, .$$

Slantwise convection occurs at an angle between the horizontal and vertical directional components (Markoswki and Richardson's Figure 3.10). The equation of motion for acceleration along the slantwise direction is:

$$\frac{d^2 \Delta s}{dt^2} = \overbrace{- f\left(\frac{\partial M_g}{\partial y}\Delta y - \frac{\partial M_g}{\partial z}\Delta z\right)\cos\alpha}^{F_h} + \overbrace{\left(-\frac{g}{\bar{\theta}}\frac{\partial \bar{\theta}}{\partial y} - \frac{g}{\bar{\theta}}\frac{\bar{\theta}}{\partial z}\right)\sin\alpha}^{F_v} \, .$$

Acceleration occurs along the slantwise path as a result of the net forcing from horizontal and vertical restoring forces. The horizontal restoring force is inertial and is related to geostrophic absolute momentum, whereas the vertical restoring force is related buoyancy. Although parcels might be stable with respect to horizontal and vertical restoring forces, slantwise instability can exist. Assessing symmetric instability is slightly more involved than assessing stability for buoyancy or inertial instability. One can assess symmetric instability with a carefully cut south to north cross-section that included isentropes and lines of constant geostrophic absolute momentum. If the slope of the potential temperature lines exceeds the slope of the momentum lines then symmetric instability exists (Markowski and Richardson's Figure 3.10). The slope criteria for symmetric instability can be expressed as:

$$\left(\frac{\Delta z}{\Delta y}\right)_{\bar{\theta}} > \left(\frac{\Delta z}{\Delta y}\right)_{M_g}$$

The cross-section method for assessing symmetric instability is unsatisfactory for many 3-hour Periods because special care must be taken to create cross-sections that adequately sample the three-dimensional space. Therefore, the following alternative three-dimensional method is more robust (McCann, 1995). This method relies on the potential vorticity relationship:

$$PV_g = -g\eta_g \bullet \nabla\theta ,$$

where g is the gravitational constant, η_g is the three-dimensional (x,y,p) geostrophic absolute vorticity vector, ∇ is the three dimensional gradient operator, and θ is the potential temperature. Potential temperature can be replaced with equivalent potential temperature or saturation equivalent potential temperature to evaluate equivalent potential vorticity (EPV_g) and saturation equivalent potential vorticity (EPV_g^*), respectively. Working out the dot product yields which can be used for calculating potential vorticity, equivalent potential vorticity, or saturation equivalent potential voriticty.

$$PV_g = -g\left[\left(\frac{\partial w_g}{\partial y} - \frac{\partial v_g}{\partial p}\right)\hat{i} + \left(\frac{\partial u_g}{\partial p} - \frac{\partial \omega_g}{\partial x}\right)\hat{j} - \left(\frac{\partial v_g}{\partial x} - \frac{\partial u_g}{\partial y}\right)\hat{k}\right] \bullet \left[\frac{\partial \theta}{\partial x}\hat{i} + \frac{\partial \theta}{\partial y}\hat{j} - \frac{\partial \theta}{\partial p}\hat{k}\right]$$

$$PV_g = \left[\frac{\partial \theta}{\partial x}\frac{\partial v_g}{\partial p} - \frac{\partial \theta}{\partial y}\frac{\partial u_g}{\partial p} - \left(\frac{\partial v_g}{\partial x} - \frac{\partial u_g}{\partial y} + f_k\right)\frac{\partial \theta}{\partial p}\right]$$

Just as with buoyancy instabilities, the atmospheric moisture condition determines which form of instability is present and determines which instability measure to use (Schultz and Shumacher, 1999). When the atmosphere is dry, it is appropriate to use the potential vorticity relationship, where

$$PV_g < 0$$

means that symmetric instability exists. When the atmosphere is moist, but unsaturated, it is appropriate to use equivalent potential voriticity, where

$$EPV_g < 0$$

means that potential symmetric instability (PSI) is present. When the atmosphere is moist and saturated, it is appropriate to use saturation equivalent potential temperature, where

$$EPV_g^* < 0$$

means that conditional symmetric instability (CSI) is present.

For moist gravitational or slantwise convection to be realized, it's not sufficient for decreasing $\frac{\partial \overline{\theta}_e^*}{\partial z}$ or negative EPVg* . Sufficient lift and moisture must also be present to realize convection.

Appendix E – Lists of Two-Step Intermittent Precipitation Detection Process 3-hour Periods

Note: 3-hour periods highlighted in bold were used in the sounding analysis.

E.1 Mostly Stratiform Precipitation 3-hour Periods (386)

2002110718	**2002110800**	2002110803	2002111215	2002121109	**2002121112**
2002121115	2002121118	2002121121	2002121221	**2002121300**	2002121303
2002121306	2002121321	**2002121400**	2002121409	**2002121412**	2002121415
2002121418	2002121421	**2002121500**	2002121521	**2002121600**	2002121603
2002121606	2002121609	2002122603	2002122606	2002122815	2002122818
2002123009	**2002123012**	**2003010300**	2003010303	**2003010400**	2003010406
2003010409	**2003010412**	2003010415	2003011121	**2003011200**	2003011203
2003011206	2003011209	**2003011212**	2003011215	**2003011400**	2003011403
2003012209	**2003012212**	2003012215	**2003012600**	2003012603	2003012606
2003012915	2003012918	2003012921	**2003013000**	2003013003	2003013006
2003013009	2003013015	2003013109	**2003013112**	2003021606	2003030709
2003030712	2003030809	**2003030812**	2003030815	2003030818	2003030906
2003031209	2003031221	**2003031300**	2003031306	2003031309	2003031315
2003031321	2003031403	2003031921	**2003032000**	2003032109	**2003032112**
2003032115	2003032118	2003032121	**2003032200**	2003032203	2003032206
2003032209	**2003032212**	2003032215	2003111515	2003111615	2003111618
2003111721	**2003111800**	**2003111912**	2003111915	2003111918	2003112903
2003112906	**2003120112**	2003120115	2003120118	**2003122000**	2003122006
2003122103	2003122406	2003122409	2004010621	**2004010700**	2004010703
2004010706	2004010806	2004010821	**2004010900**	2004010903	2004010906
2004011000	2004011415	2004011418	**2004011500**	2004011809	**2004011812**
2004012303	2004012306	2004012309	**2004012312**	2004012318	2004012321
2004012400	2004012403	2004012406	2004012809	2004012815	2004012818
2004012821	**2004012900**	2004012903	2004012906	2004012909	**2004012912**
2004012915	2004012918	2004021403	2004021406	2004021609	**2004021612**
2004021615	2004021618	2004021621	2004021715	2004030315	2004030318
2004032515	2004032518	**2004110112**	2004110115	2004110218	2004110221
2004110300	2004111518	2004111521	**2004111600**	**2004120500**	2004120503
2004120506	2004122521	**2004122600**	2004122603	2005011718	2005011721
2005011800	2005011803	2005011806	2005011809	2005012903	2005031915
2005031918	2005031921	2005032021	2005032609	**2005032612**	2005032615
2005032618	2005032621	**2005032700**	2005032703	2005032706	2005032709
2005032712	2005032715	2005032718	2005032721	**2005110112**	2005110115
2005110118	**2005110600**	**2005111300**	2005111303	2005111306	2005111309
2005111315	**2005112500**	2005112503	2005112509	**2005112512**	2005112515
2005112518	**2005121912**	2005121915	**2005122000**	2005122003	**2005122012**
2005122112	2005122115	2005122118	2005122121	**2005122200**	**2005122600**
2005122706	2005122709	**2005122712**	2005122806	2005122809	**2005122812**
2005122815	**2005123000**	2005123003	2005123009	**2005123012**	2005123015
2005123018	2005123021	**2006010600**	2006010615	2006010618	**2006010700**
2006010703	2006010706	2006010909	**2006010912**	2006010915	2006010918

2006010921	**2006011000**	2006011003	2006011009	**2006011012**	2006011021
2006011221	**2006011300**	2006011303	2006011306	2006011309	**2006011312**
2006011318	2006011321	**2006011400**	2006011403	2006011406	2006011703
2006011706	2006012921	**2006013000**	2006013006	2006013009	2006020406
2006022703	2006022709	**2006032400**	2006032406	2006032409	**2006110200**
2006110203	**2006110212**	2006110215	**2006110400**	2006110418	2006110518
2006110521	**2006110600**	2006110603	2006110709	**2006110712**	2006110715
2006110718	2006111915	2006111918	**2006112000**	2006121109	2006121115
2006121118	2006121303	2006121306	2006121406	2006121409	2006121415
2006122018	2006122021	2006122309	**2006122500**	2006122503	2006122506
2006122609	2006122615	2006122618	2007010118	2007010121	2007010303
2007010306	2007010309	**2007010312**	2007010315	2007010718	2007010721
2007010800	2007020909	2007021418	2007021421	2007021509	**2007021512**
2007021515	2007021521	**2007021600**	2007021603	2007021609	**2007021612**
2007021621	2007021921	2007030221	**2007030300**	2007030303	2007030306
2007030309	2007031906	2007031909	**2007032400**	2007032403	2007032406
2007032409	**2007032412**	2007032415	2007032418	2007032509	**2007032512**
2007032606	2007032609	2007111709	**2007111712**	2007111715	2007111815
2007111818	**2007112700**	**2007120300**	2007120303	2007120306	2007120309
2007120312	2007120315	2007120318	2007120321	2007122315	2007122318
2007122400	2007122403	2007122406	**2008010212**	2008010215	2008010221
2008010300	2008010303	2008010306	2008010309	**2008010312**	2008010318
2008010321	2008010415	**2008011500**	2008012618	2008020709	2008031309
2008032309	**2008032312**				

E.2 Convective Embedded within Stratiform Precipitation 3-hour Periods (126)

2002111200	2002111203	2002121006	**2002121612**	**2002122712**	**2003010212**
2003010418	2003012218	2003012221	**2003012300**	2003012609	2003012615
2003013018	2003013021	2003013115	2003021515	2003030715	2003030718
2003030909	**2003030912**	2003031218	2003032503	2003032606	2003111621
2003112900	2003120306	**2003122412**	2004010809	**2004012812**	2004020615
2004020618	**2004021500**	2004021718	2004021721	2004021806	2004022515
2004032412	2004111809	**2004111812**	2004120809	**2004121000**	2004121403
2005011812	**2005032100**	2005110321	2005110521	**2005111100**	2005122021
2005122100	2005122203	**2005122212**	2005122215	2005122221	2005122603
2005122606	**2005122612**	2005123006	**2005123100**	2006010609	**2006010612**
2006011006	**2006011100**	2006011103	2006011709	**2006013012**	2006020221
2006110218	2006110221	2006110403	**2006110500**	2006110503	2006110606
2006110609	**2006110612**	2006110615	2006110618	2006110621	**2006110700**
2006110703	2006110706	**2006111600**	2006111603	2006111921	**2006112112**
2006112115	2006121106	2006121121	2006121309	**2006121412**	2006121418
2006121421	**2006121500**	2006122106	**2006122312**	2006122418	2006122621
2007010221	**2007010300**	**2007020912**	**2007021500**	2007021518	2007111006
2007111009	**2007111012**	2007111603	2007111615	2007111618	2007111621
2007111718	2007112703	2007120221	**2007120400**	2007121809	**2007121812**
2007121815	2007122218	2007122321	2008010218	2008010315	2008011009
2008011215	**2008013112**	**2008031100**	**2008031312**	2008032315	2008032318

E.3 Mostly Convective Precipitation 3-hour Periods (98)

2002110906	2002110909	**2002110912**	2002110915	2002111221	2002121003
2002121509	2002121618	2003010306	2003010421	2003012618	**2003111700**
2003111703	2003111706	2003122418	2004011915	2004021506	**2004021800**
2004021812	2004022721	**2004022800**	2004022803	**2004120812**	2004120815
2005012909	**2005031912**	2005032009	**2005032012**	2005032803	**2005110400**
2005110403	2005122206	2005122621	2005122718	2005122903	2005122906
2005123109	**2006010100**	2006010103	2006010715	2006010718	2006013018
2006020209	**2006020212**	2006020215	2006020218	**2006020300**	2006030606
2006032418	**2006110300**	2006110303	2006110306	2006110309	**2006110312**
2006110315	2006110318	2006110406	2006110421	2006110506	2006110809
2006110812	2006111421	**2006112100**	**2006121100**	**2006121200**	2006121203
2006121206	2006121503	2006121506	**2007010712**	2007020921	2007021109
2007021400	2007022003	2007032006	2007032515	2007111609	**2007111612**
2007120403	2007120406	2007120409	2007120415	2007120609	**2007120612**
2007120615	2007120618	**2007120700**	2007121818	**2008010400**	**2008011012**
2008011015	**2008011212**	2008011218	2008013109	**2008020712**	2008020718
2008031315	2008031318				

E.4 Split Stratiform/Convective Precipitation 3-hour Periods (31)

2002110921	2003010321	2003011303	2003120103	**2003122100**	2003122106
2004011815	**2004011912**	2004011918	2004022521	2004022606	2004110215
2004121003	**2005012900**	**2005032800**	2005122509	2005122615	2005122715
2005123121	2006010709	2006022718	2006110321	**2006122612**	2007010318
2007021100	**2007032000**	2008013118	2008030803	2008030806	2008030809
2008032321					

Appendix F – Additional Buoyancy Instability Results

F.1 Discussion

Figures F.1-F.3 are vertical distributions of $\frac{d\bar{\theta}}{dz}$, $\frac{d\bar{\theta}_{es}}{dz}$, and $\frac{d\bar{\theta}_{e}}{dz}$, respectively. A layer with negative values is absolute, conditional or potentially unstable, respectively. As expected, Figure F.1 indicates all precipitation modes as being absolutely stable; however, the mostly convective 3-hour periods have the weakest absolute stability, followed by embedded within stratiform 3-hour periods, and then mostly stratiform 3-hour periods. Mostly notably, many embedded convective within stratiform 3-hour periods have conditional instability aloft above 3.5 km, more so than mostly stratiform 3-hour periods. Embedded convective 3-hour periods also have slightly more potentially unstable layers aloft. This is consistent with figure 5.12, which shows more frequent conditional instability aloft with embedded 3-hour periods. Potential instability appears to be extremely important for a large subset of mostly convective cases from the surface to 4 km (Fig. F.3)

F.2 Appendix Figures

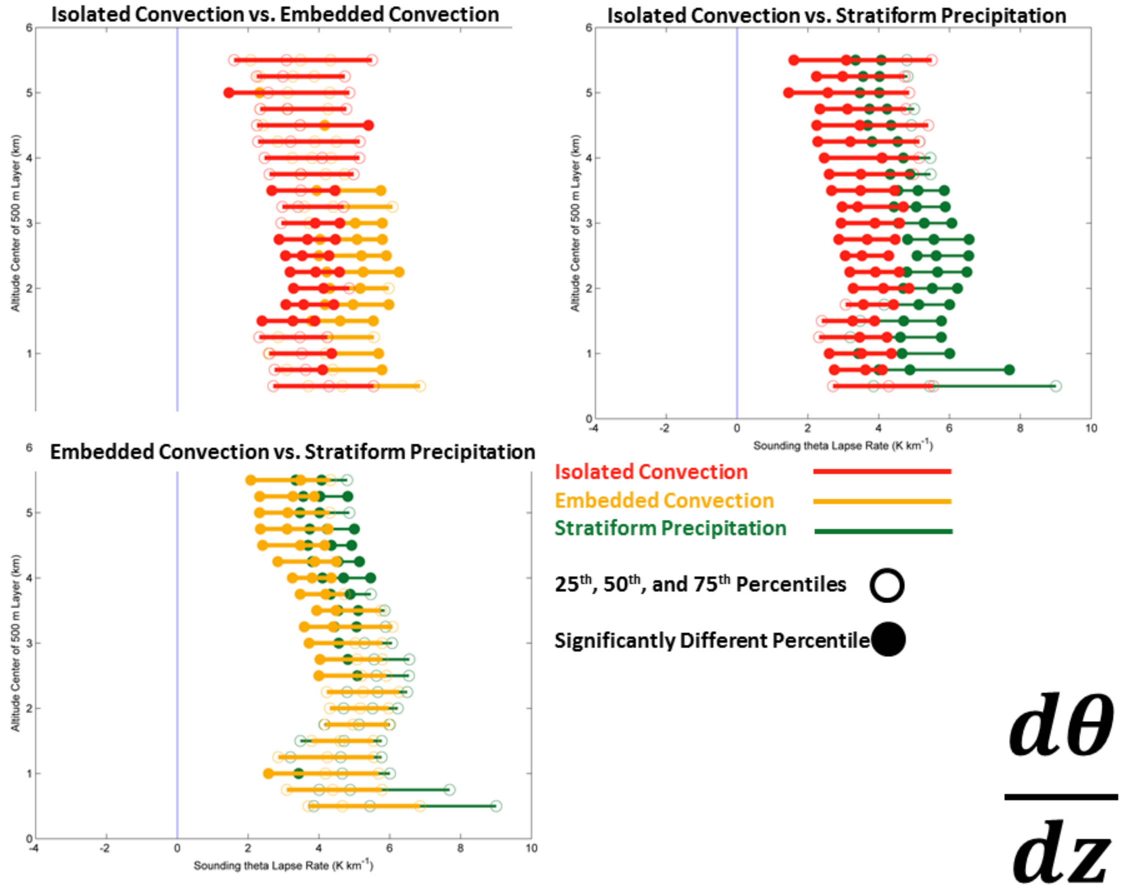

FIG. F.1. Vertical distributions of $\frac{d\bar{\theta}}{dz}$. Circles are 25th, 50th, and 75th percentiles. Filled circles represent percentile differences which are statistically significant. Unfilled circles represent percentile differences that are not statistically significant. Gold lines and circles are embedded convective within stratiform 3-hour periods, while green lines and circles are mostly stratiform 3-hour periods. Values are calculated over 500 meter layers.

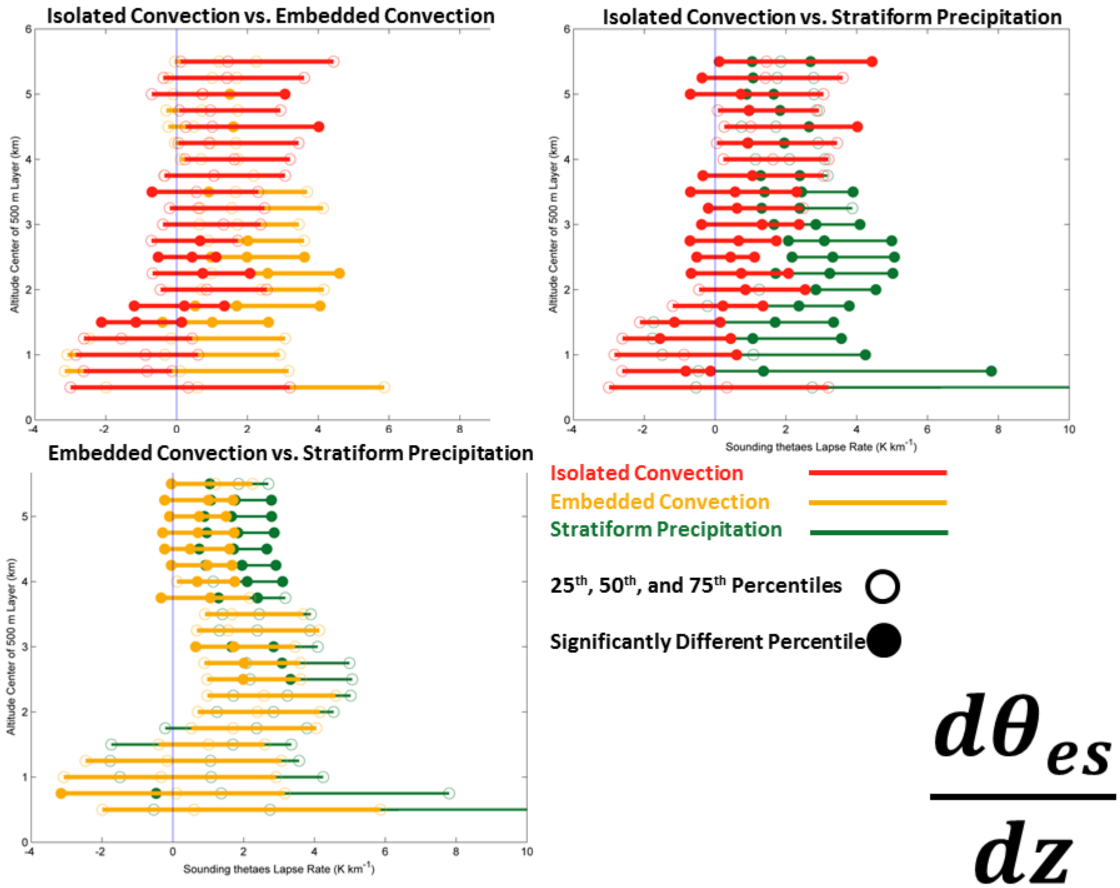

FIG. F.2. Vertical distributions of $\frac{d\bar{\theta}_{es}}{dz}$. As in F.1.

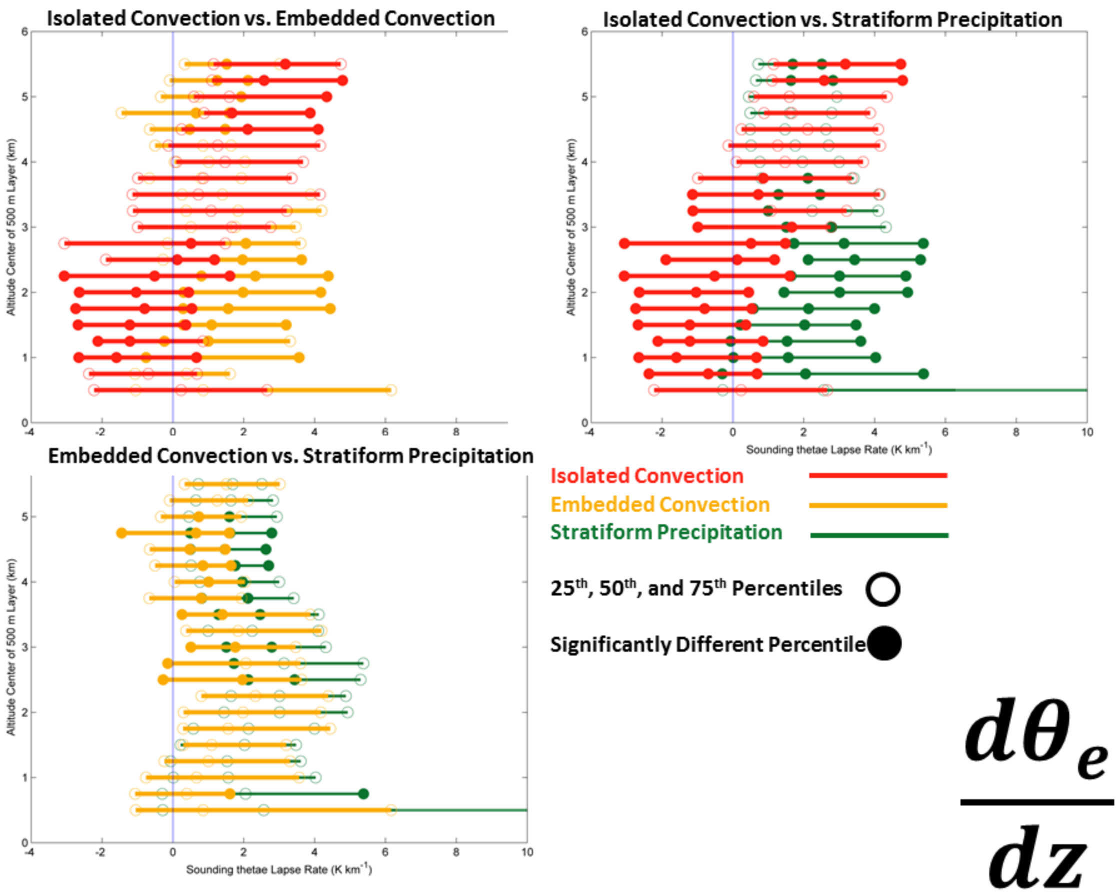

FIG. F.3. Vertical distributions of $\frac{d\bar{\theta}_e}{dz}$. As in F.1.